UCRL-53179-83
Distribution Category UC-20,20D

UCRL--53179-83

DE85 008352

Fire Protection Research for DOE Facilities: FY 83 Year-End Report

H. K. Hasegawa, N. J. Alvares,

A. E. Lipska-Quinn, D. G. Beason,

K. L. Foote, S. J. Priante, and K. Staggs

Manuscript date: August 2, 1984

LAWRENCE LIVERMORE NATIONAL LABORATORY
University of California • Livermore, California • 94550

Available from: National Technical Information Service • U.S. Department of Commerce
5285 Port Royal Road • Springfield, VA 22161 • $10.00 per copy • (Microfiche $4.50)

Contents

Fire Protection Research for DOE Facilities: FY 83 Year-End Report

Abstract

We summarize our research in FY 83 for the DOE-sponsored project, *Fire Protection Research for DOE Facilities*. This research program was initiated in 1977 to advance fire-protection strategies for energy technology facilities in order to keep abreast of the unique fire problems that develop along with energy technology research. Since 1977, the program has broadened its original scope, as reflected in previous year-end reports. We are developing an analytical methodology through detailed study of fusion energy experiments at Lawrence Livermore National Laboratory (LLNL). Using these experiments as models for methodology development, we are currently advancing three major task areas: (1) the identification of fire hazards unique to fusion energy facilities, (2) the evaluation of accepted fire-management measures to meet and negate hazards, and (3) the performance of unique research into problem areas we have identified to provide input into analytical fire-growth and damage-assessment models.

Introduction

We report our work performed in FY 83 for a DOE-supported study entitled *Fire Protection Research for DOE Facilities*. Previous fiscal-year reports have been published.[1-4] One ultimate goal of this study is the assessment of potential fire damage in such facilities. To accomplish this, three parameters have to be evaluated: (1) the fire-threat potential to the facility, (2) the response and effectiveness of fire-management systems, and (3) the possible fire-related damage.

The milestone chart in Fig. 1 delineates the sub-tasks (marked by bullets) that must be completed to achieve our major goals (underlined) for this program. These major goals are all necessary to the ultimate objective: a standard guide of fire-management tactics for large DOE facilities. It is appropriate here to describe the logic and significance of each milestone as to its contribution to the final result. The sub-tasks listed under *Fire Growth Parameters for Model Development* are a combination of small- and large-scale fire experiments to provide appropriate input for our modeling efforts and is also a partial model-validation tool. Those sub-tasks supporting *Smoke Aerosol Production and Transport; Physical and Chemical Characteristics* will help define two major phenomena: (1) the potential corrosive and particulate damage to experimental components, and (2) the particulate analysis (size, distribution, etc.) that will provide insight into the response times of smoke detection systems.

The next two milestones listed in Fig. 1 (*Adaptation of Modeling Technique for Fire-Risk Assessment* and *Advanced Fire Management System Development*) integrate all results from the previous two milestones and are probably the most significant components to the program. They combine all the facets of what has been learned that can be applied to actual facilities. The modeling technique will predict the rate and extent of fire development in these facilities and the work on fire-management systems will define how detection and suppression response to predicted fires will modify the degree of fire damage. The *Advanced Fire-Management-System Development* phase will concentrate on unique detection and suppression systems to deal with fire problems in DOE facilities that traditional countermeasures cannot negate.

In FY 83, we made significant progress in a number of task areas. In general, we completed our analysis of the 1982 fire-model data and we compared six fire models to the data from three of the 1982 tests. In addition, two separate publications were derived from the series. Toward the end of FY 83, we initiated an 1983–1984 series of

PROJECT 6294-93 FIRE PROTECTION RESEARCH
FOR ENERGY TECHNOLOGY PROJECTS

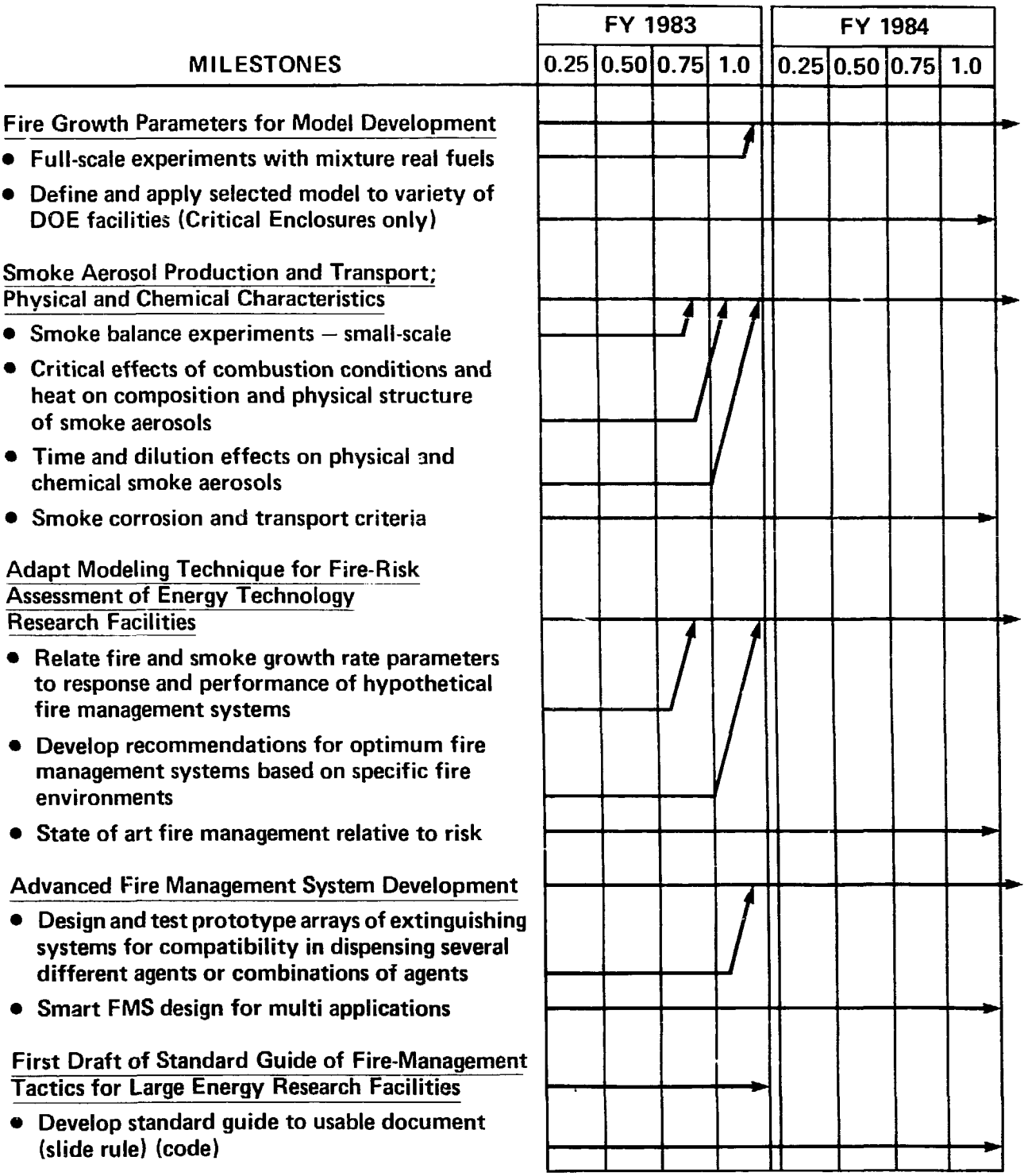

Figure 1. Descriptive chart of project milestones for LLNL fire-protection research for DOE facilities.

widely varying fire-model tests using improved instrumentation and methodology. The results from our FY 82 test series led us to a research plan that we pursued for cable insulations in our Ease-of-Ignition apparatus. We found, non-conclusively, that ignition times of some cable types can be predicted from certain physical characteristics. At the same time, we performed 17 large-scale vertical cable burns using the FY 82 research protocol. The results reconfirmed our FY 82 findings.

In the area of chemical characteristics of smoke aerosol, we started and completed high-temperature studies on the Lawrence Livermore National Laboratory (LLNL) inventory of insulations by thermogravimetric analysis, differential scanning calorimetry, and gas chromatographic/mass spectrometry. We also started and completed detailed analyses of Teflon and Kynar wire insulations.

Finally, although not listed as a specific milestone, we completed a reliability analysis of the LLNL water-supply system in the event of a major fire. This study falls under the major heading of *Adopt Modeling Techniques for Fire-Risk Assessment of Energy Technology Research Facilities.* We used the Digraph-Fault Tree technique, which can analyze a variety of complicated systems, such as reactor-cooling systems and nuclear-material-safeguard systems.

Fire Modeling

Our FY 81 and 82 year-end reports have already described the objectives of our efforts to create a versatile computer model that simulates fires in a forced-ventilation enclosure.[1,2] Here, we cover the final conclusions from an analysis of the 1982 fire-model tests, compare six fire model's predictions with the 1982 tests, and discuss the 1983 fire-model tests.

In 1982, we completed 27 fire-model validation studies and started an analysis of same. We finished this analysis in 1983. This involved careful checking of air and fuel flows, balancing the gas species present, and analyzing wall thermocouples. We presented these findings in a paper at a National Bureau of Standards' meeting that honored Howard Emmons.[5] This paper is included in its entirety as Appendix A. The most important conclusions were that up to 80% of the energy from the fires is absorbed by the enclosure walls, that over 2000 s are required to reach "chemical equilibrium" in our test cell, and that twice the stoichiometric amount of air is required for total combustion of the fuels we used.

We chose 3 of the 1982 tests (Tests 8, 9, and 27B) for 6 model-validation comparisons. Our results indicate that these models need significant improvements in order to correctly predict the parameters of a fire in our forced-ventilation enclosure. The difficulty of such model improvements and the time required to complete them is not known. The comparisons and soon-to-be-analyzed 1983–1984 results should, however, speed up this process.

Even though we found all of the current versions lacking in some respects, we ranked them as to their "friendliness" and utility to our goals. This is the ranking as follows: California Institute of Technology one-layer model (Cal Tech I), Battelle Pacific Northwest Laboratories' model (PNL), the Harvard model, the Los Alamos National Laboratory model (LANL), Cal Tech two-layer model (Cal Tech II), and the LLNL model. In the past year, we experimented with two of the models; both models used the Cal Tech entrainment code and were difficult to modify. We acquired and rewrote the Cal Tech I model, a relatively small code, so we could run and modify it ourselves as necessary.

The analysis of the 1982 experimental data pointed out many problems in our experimental approach, one of which was elucidating enclosure-fire characteristics more fully. Table I lists the problems of the 1982 experimental series and the improvements we applied to the 1983–1984 forced-ventilation tests. The most significant changes were to the gas analysis and airflow systems. Leaks in the test cell and the duct were plugged, and the HEPA filter was removed to improve the airflow measurements. More gas analyzers were added and a different calibration and sampling system was used that made the O_2, CO_2, and CO measurements more reliable. All the improvements combined make the 1983 fire-model tests the best forced-ventilation data to date.

Table 2 lists 35 experiments completed in the last quarter of FY 83 and the first quarter of FY 84. These tests investigated forced-ventilation fires near walls and in corners, as well as fires raised off the ground. We also explored the effects of the position of the inlet and exit ducts. Since most of

Table 1. Improvements in instrumentation, calibration and techniques for 1983 model test series.

1982 Problem	1983 Improvement	Comments	Techniques
Instrumentation			
1. Not enough thermocouples. 105 channels only 40 TC channels	1a. More channels (118) 50 TC. 1b. Non-essential channels and instruments deleted.	1. Uncertainty in the effect of ambient conditions (i.e., heated test cell).	1. Only one test was done per day.
2. Uncertainty in airflow measurements.	2a. Sharp edged orifice installed in orifice. 2b. Amenometer matched to both sharp-edged orifices. 2c. Leaks in cell and duct patched.	2. Pool fires were not directly correlatible to burner fires because of pan diameter.	2. The pool pan diameter was matched to the burner diameter.
3. Uncertainty in wall temperatures.	3. Wall TCs were embedded in the wall with sauraisen.	3. Inability to correlate different tests and confirm results.	3a. Fewer changes in fuel and fire strength. 3b. More overventilated tests. 3c. More repeated tests.
4. Uncertainty in gas measurements.	4a. O_2 analyzer added (4 total) 4b. CO_2 analyzer added (3 total) 4c. CO analyzer added (3 total) 4d. H_2O analyzer added (1 total)	4. Some data were useless or misleading.	4a. O_2 analysis moved from test cell floor to midpoint of room. 4b. The test cell walls were divided into zones with equal areas that could better account for the geometry of the test cell. 4c. Wall TC's were repositioned throughout the test cell in each of the new zones instead of on just one wall. 4d. Radiometers and calorimeters were repositioned to measure the fire not the layer. 4e. Turbidity meters deleted.
5. CH_4 burner too small (Dia ~ 30 cm) created momentum jet.	5. Enlarged burner (Dia ~ 56 cm)	5. Uncertainty in gas measurements.	5. Gas samples were "pumped" into the gas analyzers instead of "pulled." This allowed fast response times and didn't build up large pressures in the analyzers to interfere with the calibration.

Table 1. (Continued)

1982 Problem	1983 Improvement
6. Exit airflow changes too much during test.	6. HEPA filter was removed.
7. CH_4 massflow went out of turbine flowmeter's range.	7. New turbine flowmeter purchased and installed.
Calibration	
1. Uncertainty in airflow measurements.	1. All three airflow instruments were calibrated in the same short duct to the same flow before any tests were run.
2. Uncertainty in gas measurements.	2a. Gas calibration was checked daily.
	2b. Calibration was done at sample probe and at analyzer not just the analyzer.
3. Uncertainty in radiation measurements.	3a. Radiometer and calorimeter were recessed in walls.
	3b. All radiometers and calorimeters were precalibrated to proper operation.

these tests were completed at the end of the year, the results will be published in a subsequent report. The 1982–1983 data represent a wide variety of forced-ventilation tests, wide enough, we feel, to validate a computer code that simulates the fire conditions in our forced-ventilation enclosure and in other DOE test cells. In 1984, we will modify existing computer codes with the data to better simulate these conditions. The code that most nearly duplicates the test data will be applied to selected enclosures to assess fire risk and define appropriate countermeasures.

Table 2. Complete 1983 fire test series.

Test	Fuel ($C_xH_yO_z$)	Fire type	Initial fire strength (kW)	Initial ventilation rate (gm/s)	Position in burner room	Height of burner in room (m)	Inlet vent position	Outlet vent position
0	CH_4	burner	250	0	C[a]	0.2	Lo[b]	Hi[c]
1	CH_4	burner	490	425	C	0.2	Lo	Hi
2	CH_4	burner	490	225	C	0.2	Lo	Hi
3	CH_4	burner	490	125	C	0.2	Lo	Hi
4	CH_4	burner	490	300	C	0.2	Lo	Hi
5	CH_4	burner	250	125	C	0.2	Lo	Hi
6	CH_4	burner	250	225	C	0.2	Lo	Hi
7	CH_4	burner	250	425	C	0.2	Lo	Hi
8	CH_4	burner	490	225	C	1.0	Lo	Hi
9	CH_4	burner	490	225	WW[d]	0.2	Lo	Hi
10	CH_4	burner	250	225	WW	1.0	Lo	Hi
11	CH_4	burner	490	125	SEC[e]	0.2	Lo	Hi
12	CH_4	burner	490	225	C	0.5	Lo	Hi
13	CH_4	burner	490	225	SEC	1.0	Lo	Hi
14	CH_4	burner	490	225	C	1.5	Lo	Hi
15	CH_4	burner	490	425	C	1.5	Lo	Hi
16	CH_4	burner	490	225	C	2.5	Lo	Hi
17	CH_4	burner	490	425	C	2.5	Lo	Hi
18	CH_4	burner	490	225	C	0.2	Hi	Hi
19	CH_4	burner	490	425	C	0.2	Hi	Hi
20	CH_4	burner	490	225	C	0.2	Hi[f]	Hi
21	CH_4	burner	490	425	C	0.2	Hi	Hi
22	CH_4	burner	250	425	C	0.2	Hi	Hi
23	CH_4	burner	250	225	C	0.2	Hi	Hi
24	CH_4	burner	360	330	C	0.2	Hi	Hi
25	CH_4	burner	250	225	C	0.2	Hi	Lo
26	CH_4	burner	250	425	C	0.2	Hi	Lo
27	CH_4	burner	250	425	C	0.2	Lo	Lo
28	CH_4	burner	490	425	C	0.2	Lo	Lo
29	C_3H_8O	pool	150	425	C	0.6	Lo	Lo
30	C_3H_8O	pool	150	225	C	0.6	Lo	Lo
31	C_3H_8O	pool	150	225	C	1.5	Lo	Lo
32	CH_4	burner	250	225	C	1.5	Lo	Lo
33	CH_4	burner	250	425	C	1.5	Lo	Lo
34	C_3H_8O	pool	180	225	C	0.6	Lo	Hi
35	CH_4	burner	150	225	C	0.5	Lo	Hi

[a] C = center of room.
[b] Lo = inlet air introduced low ~ 0.2 m.
[c] Hi = inlet air introduced high ~ 4.2 m.
[d] WW = west wall.
[e] SEC = southeast corner.
[f] Hi = inlet air introduced high and directed down ~ 4.0 m.

Large-Scale Vertical Cable Burns

We conducted large-scale fire experiments to define the effect of cable size, composition, number and packing density on the vertical flame-spread rate, and, consequently, on the mass-burning rate. Although other parameters are monitored for each test, flamespread and mass-burning rate are the most important. These data will be compared to results from our small-scale tests to assess the correspondence to real conditions, and be applied to models for use in fire-risk assessment. Moreover, we can obtain specific fuel performance and enclosure-fire parameters, e.g., the temperature profile along the vertical surface, the temperature distribution throughout the test cell, and the enclosure-ventilation changes resulting from the heat-release rate.

Figure 2 shows the support structure for the vertical-cable tests. The bundle of electrical conductors is suspended from a steel cable threaded over two bicycle wheels (to decrease friction) and attached to a counterbalanced load cell. Adjacent to the specimen is a vertical panel with half-meter increments for visually monitoring the flame-spread. Calorimeters and radiometers are located at the ignition source, near the specimen bottom, and at mid-height. Similarly, chromel-alumel thermocouples are located at strategic points on the specimens, apparatus, and throughout the test cell. To monitor the melting insulation that might drip from a burning cable, a load cell is placed directly under the specimen's centerline. The weighing of cable melt is necessary to estimate mass balance and fuel-consumption rates. Thermocouples attached to specimens sense temperatures of the insulation to define heat transfer during the flamespread period.

Ignition Source

To provide a well-defined fire producing a specified heat-flux level, we constructed a premixed natural gas and air burner with gravel as a diffusion medium. This 30-cm-o.d. circular burner produced a calibrated exposure flux of 5 W/cm^2 at an energy release rate of 20 kW. A heat flux of 5 W/cm^2 or greater was identified as a threshold ignition energy from previous heat-release-rate experiments conducted at SRI, International.[3]

Test Specimen

The test specimens for this experimental series were two-layer cable bundles formed into a perpendicular "Z" configuration as shown in Fig. 3. The net vertical cable length was 1.8 m. To prevent undefined heat-loss effects on cable-burning characteristics, we designed and fabricated special low-mass hardware to hold the cables. We chose the vertical configuration to maximize the rate of flamespread and simulate a worst-case situation. To supplement our visual observations of fire growth, we attached thermocouples in a vertical array at approximately 0.4-m intervals on both faces of the specimens.

Experimental Notes

We performed the experiments in the LLNL Fire-Test Cell, an extraction-ventilation enclosure with a 4.7-m ceiling height and a total volume of 100 m^3. In FY 82, we performed 6 tests, and in FY 83, we completed 17 additional tests. The cables chosen for the FY 83 series were based on the results of the FY 82 tests. Table 3 lists the cable types, their pertinent physical characteristics, and packing densities.

To evaluate the effects of decreasing the overall mass and increasing the cable spacing, we conducted tests on three separate bundles for each cable type shown in Fig. 4. The first specimen was normally a full cable run (100% pack) that averaged 20 cables in 2 layers, with a net vertical run of 1.8 m. The second specimen contained half this number (50% pack), which allowed for a 1-cable diameter space between each cable. The third specimen contained half this number, or approximately 5 cables (25% pack), in a single layer.

The heat-release rate during these experiments were calculated using both the mass-loss and oxygen-depletion rates; but, due to the high ventilation rate (500 L/s) and sparse cable burning, only the mass-loss rate provided usable data. Consequently, the heat-release rates for the various experiments were derived from the mass-loss rate. Because many of the cable types are composed of several different polymeric materials, we had to use an average value for heat of combustion of the composite.

Table 4 summarizes the results from the cable series. The data show that the FY 83 results echoed the FY 82 burns. Specifically, the majority of cable types produced slow flamespread rates, low heat-release rates, and extended ignition times.

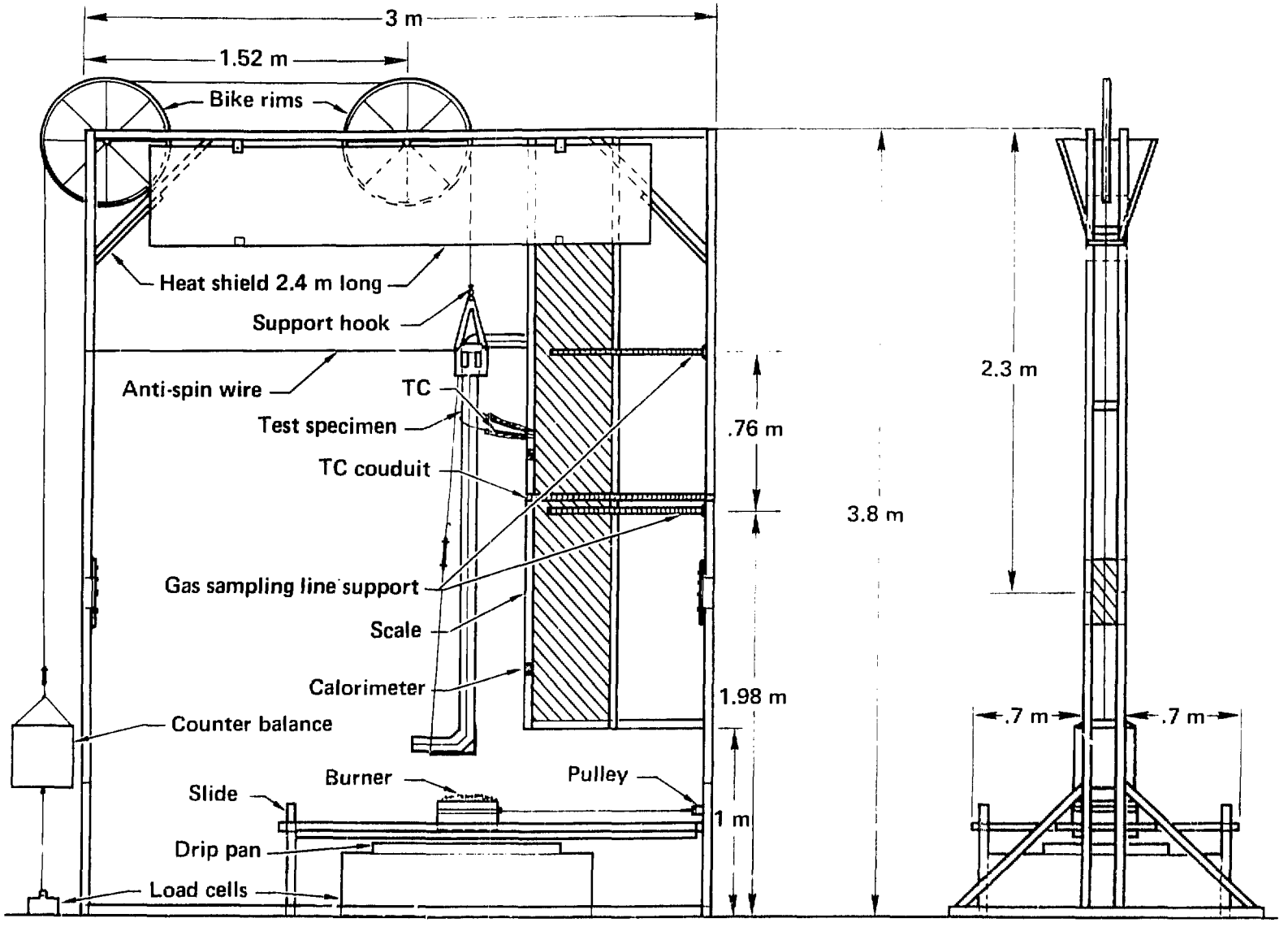

Figure 2. Experimental support structure for vertical cable burn (VCAB) experiments (TC = thermocouple).

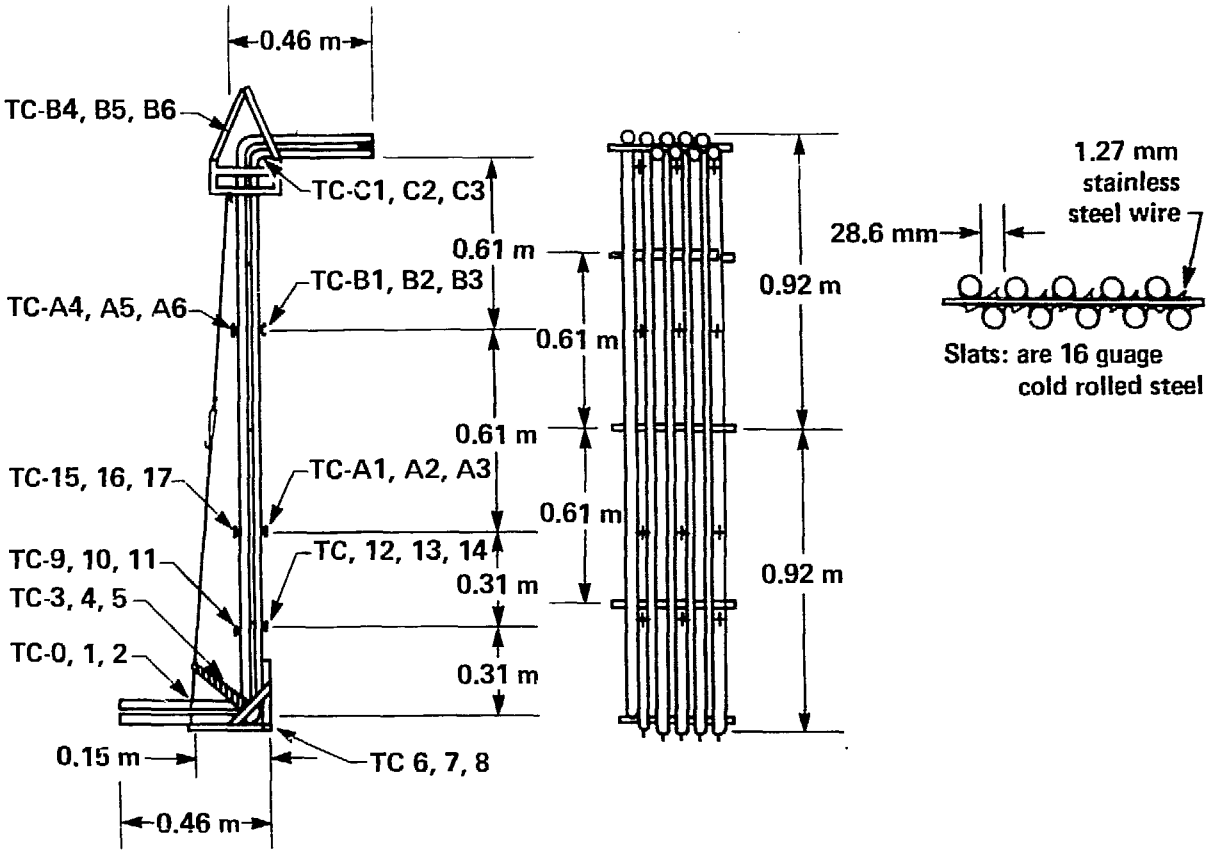

Figure 3. Thermocouple (TC) locations for vertical cable burns.

However, Tests 10–12, which were polyvinyl-chloride (PVC) multiconductors, produced relatively fast flamespread rates that covered the entire cable run. Also, these three produced consistently higher peak and average heat-release rates.

General Observations

- The 50%-pack configuration produced the highest heat-release rate for most cable types.
- When exposed to the 20-kW exposure fire, the majority of cables were very difficult to ignite.
- Once ignited, the flamespread rate was very slow.
- In most cases, the extent of flamespread was only a fraction of the vertical section.
- Heat-release rates remained low and were slow to peak.
- Fire performance correlates to the cable diameter (1.25 to 2.54 cm), the percentage of conductor, and the packing density.
- Multiconductor cables generally have less fire resistance.

In the next fiscal year, only critical experiments relating to flamespread, cable heat transfer, and cable heat-release rate are scheduled. With this data, we intend to define simple flamespread and heat-release-rate growth models as input for the enclosure-fire model we will select as a risk-analysis tool.

Table 3. Summary of cable types tested to date.

Test	Jacket mat'l (wt %)	Insulation (wt %)	Conductor (wt %)	Cable o.d. (mm)	Total wt (kg/m)	% packing
1,2	Hypalon 16.2	None	Copper 83.8	19.1	1.15	100
3	Neoprene 23.5	None	Copper 76.5	19.1	1.29	100
4	PVC 18.9	P.E. 32.1	Copper 49.0	25.5	1.12	100
5	PVC 18.9	P.E. 32.1	Copper 49.0	25.5	1.12	50
6	PVC 18.9	P.E. 32.1	Copper 49.0	25.5	1.12	25
7	Neoprene/rubber 31.0	None	Copper 69.0	23.6	1.39	100
8	Neoprene/rubber 31.0	None	Copper 69.0	23.6	1.39	50
9	Neoprene/rubber 31.0	None	Copper 69.0	23.6	1.39	25
10	PVC 27	PVC-multi 16	Copper 57	17.5	0.58	100
11	PVC 27	PVC-multi 16	Copper 57	17.5	0.58	50
12	PVC 27	PVC-multi 16	Copper 57	17.5	0.58	25
13	Neoprene 30.3	Rubber-multi 26.5	Copper 43.0	20.6	0.21	50
14	Neoprene 30.3	Rubber-multi 26.5	Copper 43.0	20.6	0.21	25
15	Neoprene 30.3	Rubber-multi 26.5	Copper 43.0	20.6	0.21	100
16	Rubber 22.35	None	Copper 77.52	21.2	1.26	50
17	Rubber 22.35	None	Copper 77.52	21.2	1.26	25
18	Rubber 22.35	None	Copper 77.52	21.2	1.26	100
19	Rubber/Hypalon (22.05)	None	Copper (77.95)	24.2	2.66	50
20	Rubber/Hypalon (22.05)	None	Copper (77.95)	24.2	2.66	25
21	Nylon/PVC (10.34)	None	Copper (89.66)	22.5	1.8	100
22	Nylon/PVC (10.34)	None	Copper (89.66)	22.5	1.8	50
23	Nylon/PVC (10.34)	None	Copper (89.66)	22.5	1.8	100

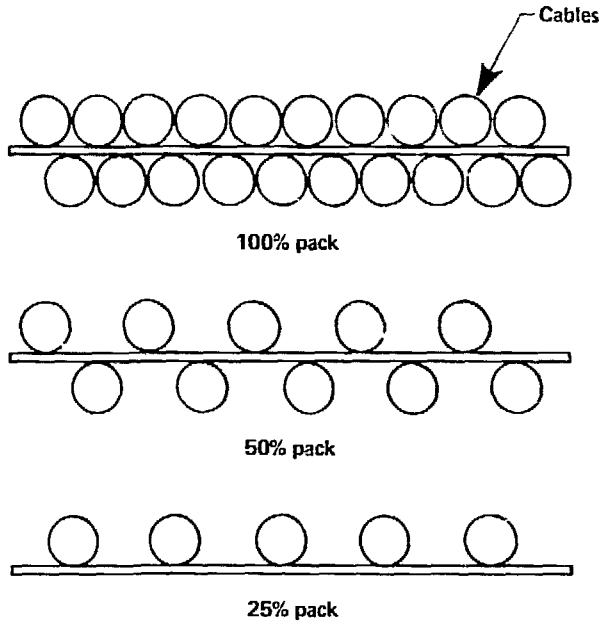

Figure 4. End view of test cable bundles showing different packing densities.

Table 4. Results of large-scale vertical cable burns.

Test	Max hrr[a] (kW)	Time (s)	Average hrr (kW)	Total flamespread (m)	Flamespread rate (m/min)
7	65.00	400	20.00	0.3	0.05
8	42.00	400	11.00	1.22	0.06
9	4.0	600	2.5	1.22	0.13
10	100.00	930	37.5	1.82	0.52
11	300.00	660	53.2	1.82	0.44
12	80.00	660	31.3	1.82	0.5
13	2.5	Average	2.2	0.3	–
14	9.75	Average	9.75	0.3	–
15	4.0	Average	2.5	0.3	–
16	75.7	400	19.95	0.61	0.03
17	43.75	300	12.12	0.61	0.06
18	5.29	1000	2.72	0.00	–
19	100.00	960	37.5	0.00	–
20	9.3	1000	6.9	0.61	0.18
21	5.3	1000	4.2	0.30	0.14
22	16.8	1000	8.9	0.61	0.06
23	2.9	500	1.4	0.30	0.04

[a] Heat-release rate.

Ease-of-Ignition Tests

In terms of fire performance, one very important characteristic of cables is how they resist ignition. The Ease-of-Ignition apparatus is a small-scale experiment that ranks materials as a function of their ignition times. Such results can also help indicate relative ignition energies of materials, identifying sources that pose potential ignition threats around these materials. For fire-modeling purposes, ignition information adds data points for stochastic ignition predictions and fire growth. Our previous small-scale cable tests had problems with the wide variation of cables' physical characteristics and insulation types, the combination of which made any realistic comparisons of performance impossible. We developed a matrix of several commonly used cables to evaluate the individual effects of cable size, geometry, composition, and materials on ignitability. We tested the effect of cable size (diameter, jacket thickness, etc.) on ignitability by varying the outside diameter of the cables while keeping the material and composition constant.

Experimental Design

Since our objective was establishing a correlation between a cable's physical characteristics and its time to ignition, we had to identify a matrix of cable types that were available in several different sizes. Our previous studies identified PVC, Neoprene, and rubber as the most commonly specified cable-jacketing materials on cables used at LLNL. We selected the cables listed in Table 5 to evaluate the effect of size and configuration (i.e., multiconductor or dielectric). To ensure uniformity of jacket composition for each of the insulating materials, chemical analyses were performed for the different cable sizes.

Ease-of-Ignition Test Method

Figure 5 shows the test apparatus and related instrumentation. The only sensors used in this series were the thermopile and water temperature thermocouple (TC). Two parallel vertical specimens, 140 mm wide and 152 mm high, face each other at a separation of 53 mm. The facing surface of both specimens are exposed to a methane diffusion flame supplied from a multiported burner located below the lower edge of the specimens. The gas flow rate through each of the independently controlled burners was set to approximately 100 ml/s (12.5 SCFH) of technical-grade methane, producing a heat flux of 3.2 W/cm^2 ± 0.2 W/cm^2 from a total gas flow of 200 ml/s ± 10 ml/s (25 SCFH ± 1.3 SCFH) that resulted in an energy release of 7 kJ/s. The reason for having two specimens face each other was to simulate the reinforcement that would occur in a worst-case fire.

Table 5. Specifications of cable-jacket material used at LLNL.

Cable type	Jacket/ dielectric materials	Jacket thickness (mm)	o.d. (mm)	Mass of jacket (g/cm)	Mass of dielectric (g/cm)	Total cable mass (kg/m)	Conductor(s) Number of conductors	Conductor(s) size (mm)	Conductor(s) % Insulation material
RG 213 A/U	PVC/P.E.	1	10	0.369	—	1.57	1	—	23.5
RG 59 B/U	PVC/P.E.	1.02	6	0.22	0.0925	0.56	1	—	56
RG 58 C/U	PVC/P.E.	0.14	4.95	0.14	0.05	0.38	1	0.9	52
Telephone cable	PVC/P.E.	0.3	7.62	0.561	—	4.37	4	—	56.6
Welding cable AWG 6	Neoprene	2.54	10.24	0.68	—	1.94	1	5.3	36
Welding AWG 4/0	Neoprene/ rubber	3.5	23	4.195	—	14	1	14	29.96
Power cord	Neoprene/ Neoprene	—	15.2	0.135	conductor jacket 0.085	0.315	4	—	72
Test product	Rubber/ rubber	2	4.75	0.13	—	0.20	1	—	65
Welding 2/0	Rubber/ rubber	2.7	19.05	1.22	—	7.85	1	3325 strands	20.9
Welding AWG 2	Rubber/ rubber	0.3	14.2	1.07	—	4.14	1	1666 strands	25.8
Audio cable	Rubber/ rubber	0.26	1.1	0.29	—	0.78	3	—	37

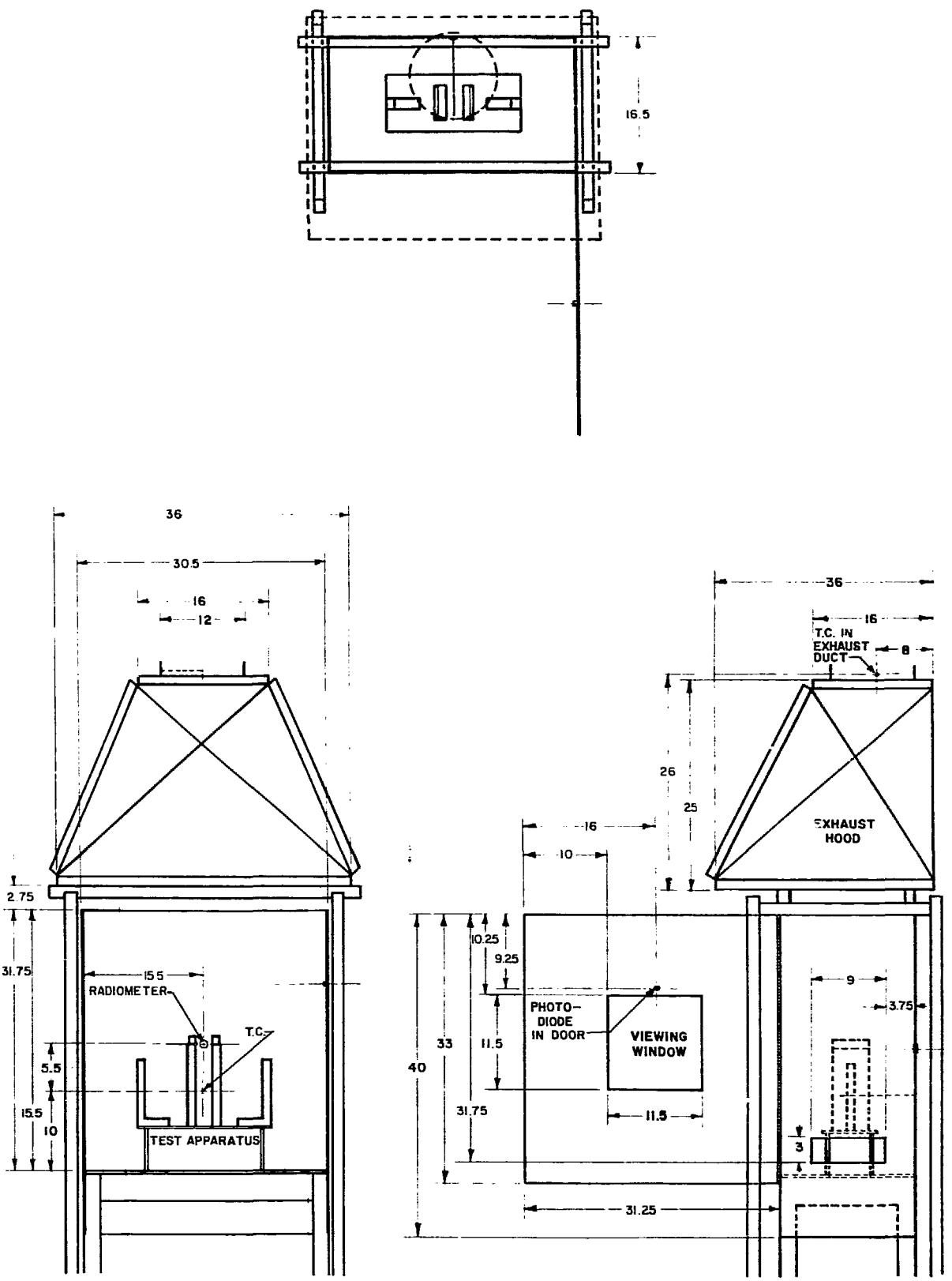

Figure 5. Schematic of ease-of-ignition apparatus.

The ignition time is indicated by the time at which a flame attachment on a specimen surface is observed and by the time when the specimens begin to contribute a significant quantity of fuel, as indicated by a rise in voltage of a thermopile. The thermopile consists of a bank of thermocouples located 6.4 mm above the top edge of each specimen and 6.4 mm out from the plane of their surfaces.[6]

Test Specimens

We tested eight rectangular cable array samples, 140 mm wide and 152 mm high. Two arrays were required for each test, and four replicate tests were conducted. The specimen holders gripped the cable samples at their ends and provided sufficient tension to prevent large deformation of the individual cables due to heating, which ensured reasonable reproducibility among samples.

We intended to establish a correlation between a cable's physical characteristics and its time to fuel contribution. In our analysis, the physical characteristics considered were the outside diameter, the total mass per centimeter, and the percentage of insulating material. These properties were then plotted against their respective times to fuel contribution. Further analysis was conducted to determine the change in performance from a single conductor to a multiconductor. PVC, Neoprene, and rubber were analyzed separately, and all conclusions were based on a comparison of the performance of the three materials.

PVC Results

As shown in Fig. 6, the PVC cables tested, with the exception of the multiconductor, were

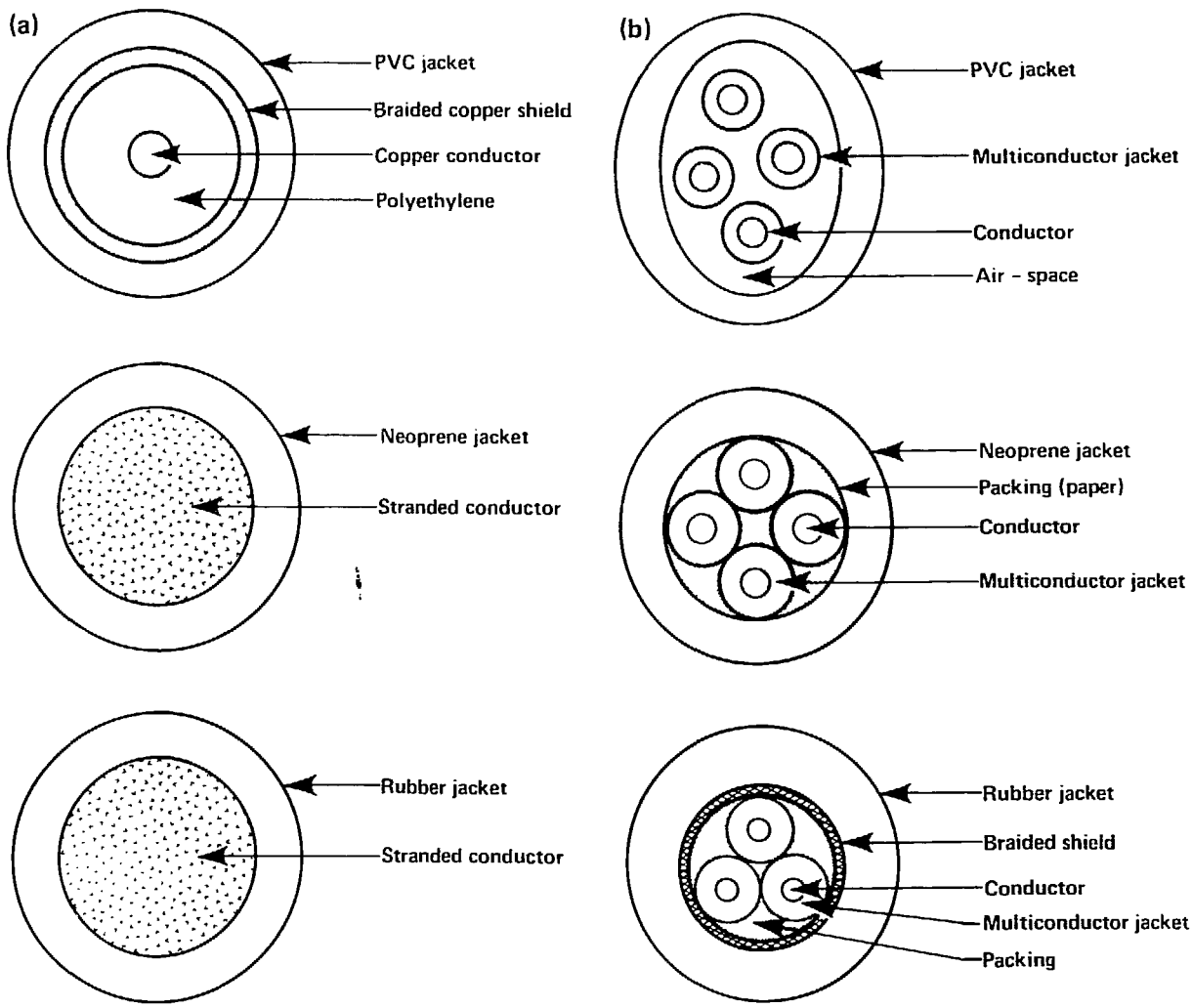

Figure 6. Cross sections of (a) single conductor cables and (b) multiconductor cables.

coaxial types using polyethylene as the dielectric material. Of the three insulating materials tested, PVC was the only one to exhibit a near linear relationship between its physical characteristics and time to ignition.

The data displayed in Figs. 7a through 7c indicate the following relationships:

- Decreasing the outside diameter reduces the ignition time (Fig. 7a).
- Although it is not a linear relationship, it appears that decreasing the mass also reduces the ignition time (Fig. 7b).

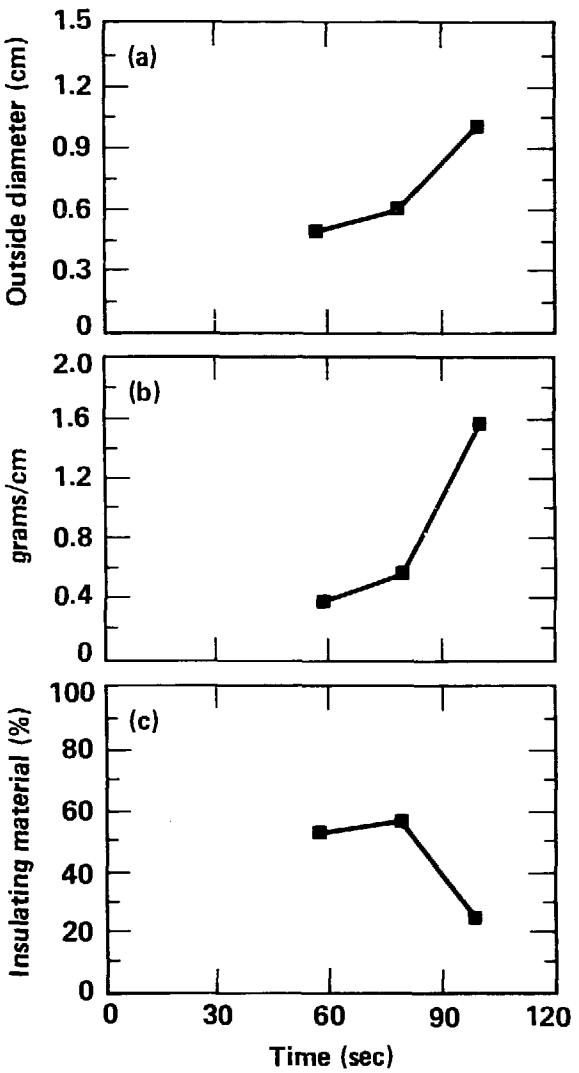

Figure 7. Times to fuel contribution for PVC as a function of (a) decrease in outside diameter, (b) decrease in mass, and (c) percentage of insulating material and the time to ignition.

- No correlation exists between the percentage of insulating material and the ignition time (Fig. 7c).

These preliminary findings follow heat-transfer principles. In order for cable insulations to ignite, they must be heated to their ignition temperature. The greater the mass, the more energy, or, in this case, the more time is needed to bring the jacket material to its critical temperature.

Conversely, reducing the mass reduces the heating time. The testing of a multiconductor seemed to confirm the physical characteristics-ignition time relationship. The four-conductor telephone cable was loosely wrapped with a PVC jacket that resulted in a substantial airspace between the outer jacket and the conductors. This elliptical cable had a major axis diameter of 0.76 cm and an ignition time of 11 s. By comparison, the RG 59 B/U cable (single conductor) with an outside diameter of 0.6 cm had an ignition time of 79 s. The greatly reduced ignition time for the multiconductor cable can be directly attributed to the airspace that allows the outer jacket material to heat up rapidly (i.e., only the mass of the jacket absorbs the heat as opposed to having the jacket and insulator in the coaxial heat up). It appears that we may be able to roughly predict the ignition times of PVC-jacketed coaxial cables with respect to the scale of the Ease-of-Ignition apparatus.

Neoprene Results

Due to limited availability, only three of the chosen four Neoprene-insulated cables were tested, and one of these was a multiconductor. So, since multiconductors are not plotted, we had to use only two data points. We can draw no clear conclusion. However, the two data points shown in Figs. 8a and 8b infer Neoprene's time-to-fuel-contribution is independent of the cables' physical properties. Both plots show that cables with vastly different outside diameters and masses had almost identical ignition times. Yet, like PVC, the Neoprene multiconductor of larger diameter displayed a fuel-contribution time of nearly half (ignited twice as fast) that of the single conductor, 47 and 85 s, respectively. This indicates that, in our choice of single-conductor cable sizes, we have exceeded a size threshold where the conductor absorbs most of the thermal energy. This makes the ignition time solely dependent on the chemical composition and the density of the jacket.

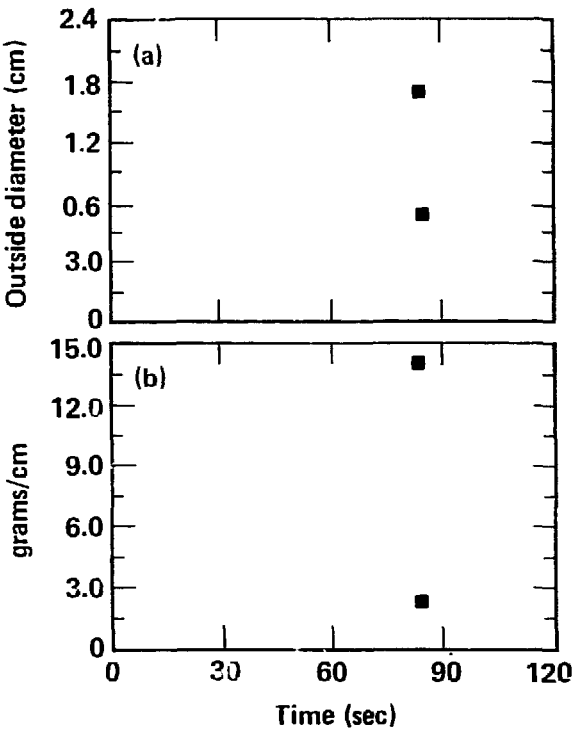

Figure 8. Times to fuel contribution to Neoprene showing (a) the outside diameter and (b) decreasing mass.

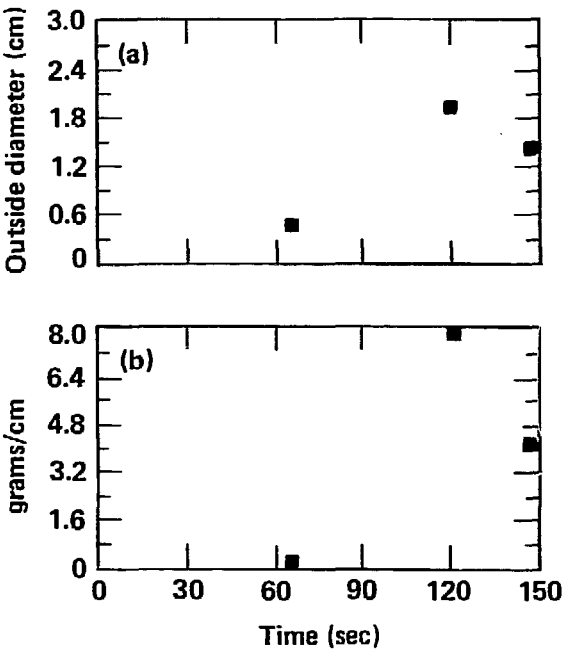

Figure 9. Rubber test result showing (a) increasing outside diameter and (b) decreasing cable mass.

Again, the energy dissipation in the multiconductor is not as pronounced as in the single conductor. Further experiments will have to substantiate this hypothesis.

Rubber Results

Preliminary examination of the rubber-insulated cables shows no correlation between physical characteristics and the time-to-fuel-contribution (see Figs. 9a and 9b). The results show that the AWG 2 cable with an outside diameter of 1.37 cm had an average time to ignition of 146 s, while the larger AWG 2/0 cable with an outside diameter of 1.9 cm had an average ignition time of 120 s. Our third data point was a 0.495-cm wire with a short time-to-fuel-contribution of 67 s. And, like the previous cables, the rubber multiconductor indicated a reduced ignition time of 69 s.

Conclusions

The results from this test series show that the Ease-of-Ignition apparatus in its present form cannot be used to accurately discriminate between materials with similar flammability characteristics. A major problem is that fire exposure fluctuates over a statistically significant range because it is a diffusion flame. Since times-to-fuel-contribution, in most cases, differ by only seconds, nonuniform exposure produces scattered results. Furthermore, the ignition time is calculated on the average of four tests. If one or more results are at extreme range, the average ignition time can be very inaccurate. Although great pains were taken to ensure uniformity among specimens before and during testing, it is highly probable that individual cables deformed during the fire. This would change the amount of cable surface area exposed to the flame, which would alter its ignition time.

We believe the combination of the above variables is significant enough to cause the random results obtained from the rubber-jacketed cable tests; the larger and more massive AWG 2/0 cable had a time-to-fuel-contribution which was 26 s less than the smaller AWG 2 cable. The following ignition times for the two cable types illustrates the wide variation in times:

Burn	AWG 2	AWG 2/0
1	135.0 s	95 s
2	119.0 s	145 s
3	172.0 s	105 s
4	159.4 s	135 s

It can be seen that both sets of data have a spread of about 50 s from the shortest to longest ignition time. A possible improvement is to substitute a radiant panel (the same size as a specimen) for one of the specimens and eliminate all the existing burner ports except for one under the sample to serve as a pilot flame. The radiant panel would provide a uniform and steady thermal flux on the specimen and should provide more reproducible results.

Consequently, our study can only provide performance trends. The study does indicate that the three major physical characteristics that govern a cable's ignition time are the mass per unit length, the outside diameter, and the ratio between conductor and insulator. It appears that cables with a conductor diameter of approximately 0.8 cm and greater, and a ratio of conductor to outside diameter of 60% or more, will have ignition times dependent primarily on the chemical composition of the jacket material. Thus, if the conductor's mass dominates the cable composition, it is as if the jacket material is attached to an infinitely conductive slab. Cables containing smaller conductor sizes will probably perform according to relationships derived from a cable's chemical composition, physical make-up, and physical dimensions, as was indicated by the PVC coaxials we tested in this study. Similarly, PVC four-wire multiconductors would perform to one relationship, triaxials to another, and so on.

Fire Chemistry: Thermal Degradation of Cable and Wire Insulations

In moderate-temperature pyrolysis of various wire and cable insulations, the insulations form detectable amounts of light hydrocarbons in the very early degradation stage.[1] Our GC/MS analyses of the liquid pyrolyzates from these insulations show no unique components of specific insulations that can help in choosing fire-resistant cables. The data, however, can be used to isolate those insulations that incorporate flammable plasticizers; such plasticizers enhance the insulations' flammability so that flame retardants should be incorporated if the plasticizers are used in the insulations.

We have found that the production of acidic components is enhanced by higher heating rates, but, higher heating rates do not increase total acid production. The presence of acid acceptors (e.g., ZnO, HgO, Sb_2O_3, and $CaCO_3$) will influence how much acid is released into the environment. This year, we extended these kinds of detailed studies to Teflon and Kynar wire insulations. And, we added more GC/MS measurements on insulations reported in last year's report, specifically high-temperature pyrolysis and usage of additional GC capillary columns to resolve pyrolyzates obtained at medium-temperature pyrolysis.

Experimental Procedure

Experiments involving Teflon and Kynar wire insulations and their corresponding virgin polymers consisted of thermogravimetric analysis (TGA), differential scanning analysis (DSCA), and GC/MS of their pyrolyzates on four chromatographic columns. Teflon and wire-insulation TGA was done in air at heating rates of 10, 20, 40, 80, and 160°C/min from ambient temperature to 900°C. As reported previously, we monitored the samples' weights and the generation of acidic components as a function of temperature. As before, the acidic components and other thermal degradation products were directed to a container filled with 200 ml of distilled water buffered to a pH of 6.8–9.8. The gaseous solution was gently stirred with a magnetic stirrer to achieve uniform mixing and the change in pH was measured with a pencil-sized pH reference electrode and recorded on a multichannel recorder.

DSCA was performed on a DuPont-900 differential scanning calorimeter using a standard cell. Our samples weighed between 5 and 10 mg and all were heated in air at 20°C/min. The rest of the testing followed the procedure reported in last year's report.[1]

Experimental Results

Teflon

Polytetrafluoroethylene (Teflon), used in small-signal wire insulations, is one of the most stable addition polymers, owing to the strength of the C-F bond and the shielding effect of the highly electronegative fluorine atoms. Reaction involves random-chain scission followed by depolymerization and chain termination by disproportionation,[7,8,9] although it has been suggested that, instead of an unzipping mechanism, CF_2 fragments are eliminated which subsequently combine in the gas phase to give tetrafluoroethylene.

Figure 10 shows our TGA results of Teflon-7, Teflon-107, and virgin polytetrafluoroethylene. Essentially, there is one degradation phase that leaves no residue at the end of pyrolysis. Of the three samples studied, virgin polytetrafluoroethylene degrades at the lowest rate and requires the lowest temperature for the onset of the main degradation phase. The main pyrolysis phase starts at 500°C for virgin polytetrafluoroethylene, at 535°C for Teflon-7, and at 540°C for Teflon-107. The main degradation phase is preceded by an induction phase that starts at 445°C for virgin polytetrafluoroethylene, at 430°C for Teflon-7, and at 450°C for Teflon-107.

The effect of heating rates on the degradation of the two Teflon insulations and virgin polytetrafluoroethylene is summarized in Table 6. As expected, higher heating rates increase the degradation rates of all three samples. The higher heating rates, however, do not change the temperature that is responsible for the onset of the main degradation phase of the virgin polytetrafluoroethylene and the effect is inconsistent on the main pyrolysis phase of both Teflon-7 and Teflon-107. We also found that heating rates of 40°C/min and higher decrease the temperature leading to the induction phase of Teflon-107. However, the induction phase of Teflon-7 remains unaffected until it

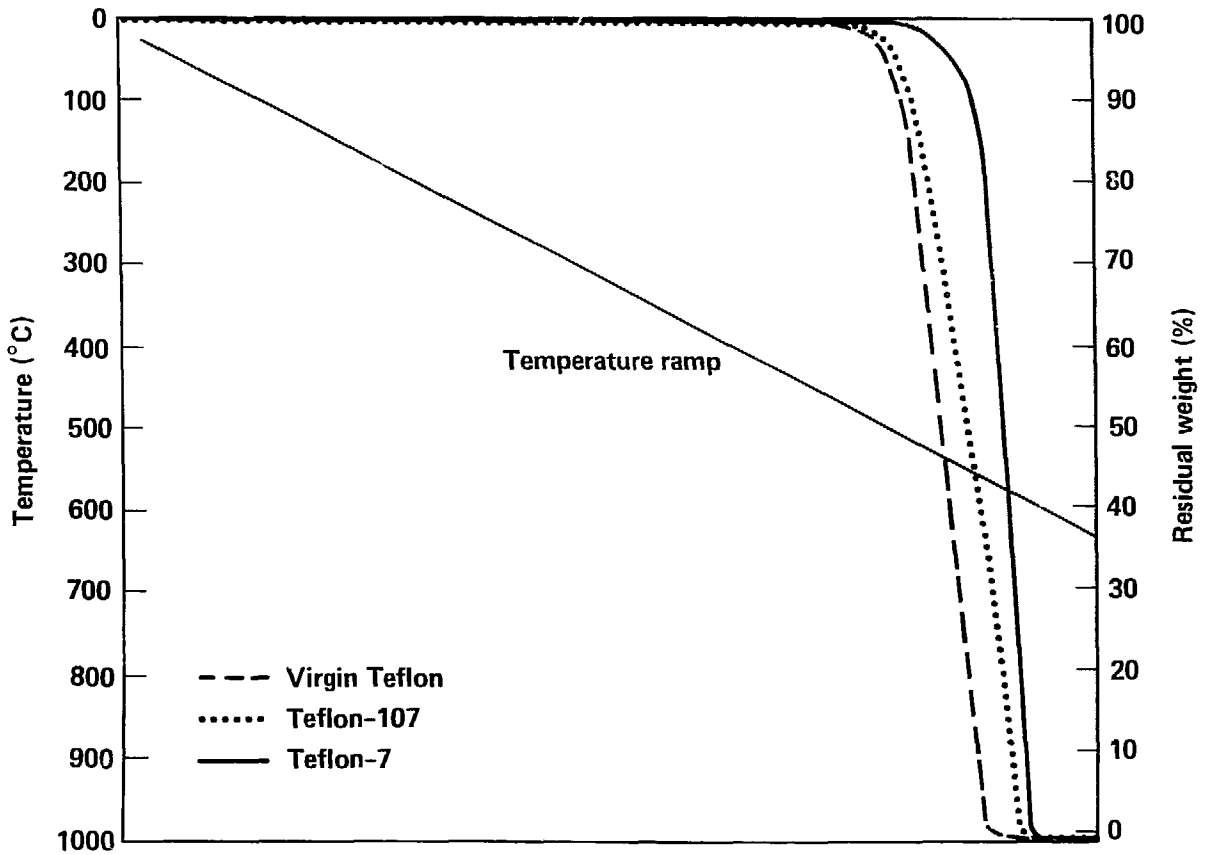

Figure 10. Thermograms of Teflon insulations heated in air at 20°C/min. The diagonal temperature ramp provides a way to correlate weight loss and temperature, where the rampline defines the apex of a right angle between discrete points on the residual weight curve and temperature scale.

Table 6. The effect of heating rate on thermal degradation of Teflon.

Sample	Heating rate (°C/min)	Onset of induction phase (°C)	Onset of main phase (°C)	Degradation rate (%/min)	Residual wt. at end of pyrolysis (%)
Virgin	10	430	500	22	0
polytetrafluoroethylene	20	445	500	33	0
	40	445	500	55	0
	80	445	500	90	0
	160	450	500	>100	0
Teflon-7	10	430	495	25	0
	20	430	535	50	0
	40	430	500	73	0
	80	485	548	>100	0
	160	230	550	>100	0
Teflon-107	10	450	545	29	0
	20	450	540	43	0
	40	425	545	82	0
	80	370	540	>100	0
	160	200	490	>100	0

is exposed to a heating rate of 160°C/min. Higher heating rates do not lower the temperature responsible for the induction phase of virgin polytetrafluoroethylene.

Figure 11 shows the DSCA of virgin polytetrafluoroethylene in air; the endotherm began at 338°C, which we attribute to melting and an exotherm began at 445°C which is at the start of the induction period or very slow decomposition phase. Teflon-7 showed an endotherm starting at 317°C and an exotherm starting 460°C, which is the beginning of the induction period. Teflon-107 showed an endotherm at 322°C and a beginning of an exotherm at 460°C, again due to initiation of the decomposition phase.

The gaseous-products analysis shows the presence of HF which we think is formed as a result of the following reaction:

$$2COF_2 + 2H_2O \rightarrow CO_2 + 4HF.$$

Other gaseous secondary products formed after dehalogenation were found to be low-molecular-weight hydrocarbons such as methane, ethylene, acetylene, ethane, propane, propyne, isobutane, n-butane, 1-butene, isobutylene, cis-2-butene, trans-2-butene, and pentane. These hydrocarbons are produced in large quantities from virgin polytetrafluoroethylene, but not from Teflon-107 and Teflon-7. Of the latter two insulations,

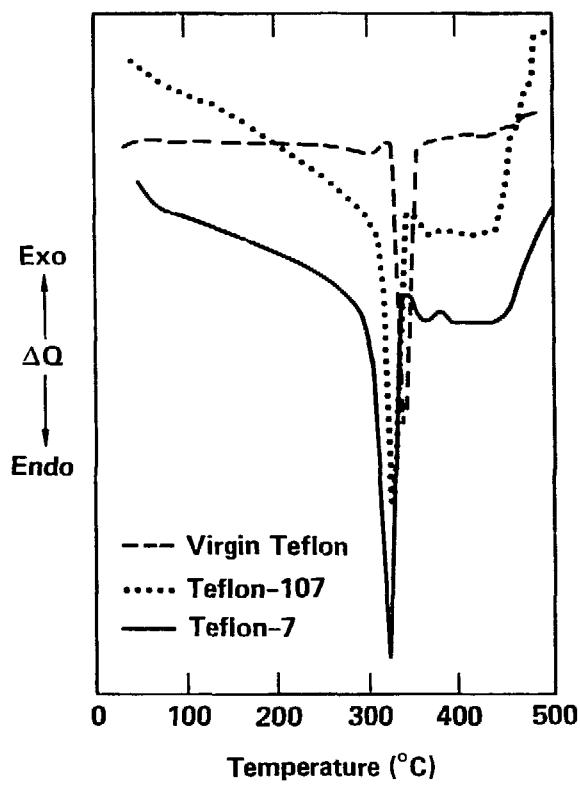

Figure 11. DSCA of Teflon insulations heated in air at 20°C/min.

Teflon-107 produces more hydrocarbons than Teflon-7. We also noticed that high-temperature pyrolysis increased the amount of the hydrocarbons in all samples. In addition, the gaseous mixture in all samples contained C_3F_8, C_3F_6, C_4F_8, C_2F_4, C_2F_6, and CF_4.

High-temperature pyrolysis of Teflon-107 led to a liquid pyrolyzate comprised mainly of trimers and tetramers of tetrafluoroethylene, hexafluorobenzene, 1,3-di-(2-xenyl)-benzene. Teflon-7's high-temperature pyrolysis resulted in liquid pyrolyzates consisting of 3,5,5-trimethyl-1-hexene, diethylphthalate, butyl methyl phthalate, dioctylphthalate, methyl-2-methyl octadecanoate, 3,6-dimethyl-3-heptanol, trimers and tetramers of tetrafluoroethylene.

The liquid pyrolyzate obtained from medium-temperature pyrolysis of tetrafluoroethylene yielded 2-H-perfluorohexane, 3,5,5-trimethyl-1-hexene, tetrafluoroethylene trimer and tetrafluoroethylene tetramer, and unidentified components. Medium-temperature pyrolysis of Teflon-107 rendered a pyrolyzate comprised of 2-methyl-1-(2-methylpropylimino) propane, perfluoroheptene-1, perfluoromethyl-cyclohexane, tetrafluoromethylcyclohexane, perfluoroheptene-1, butylphthalate, and dioctylphthalate. The phthalates are decomposition products of the plasticizer used in formulation. Medium-temperature pyrolysis of Teflon-7 produced a liquid pyrolyzate consisting of 2-N-hexyl-N-methyl pyrrolidene, butylphthalate, and dioctylphthalate.

Kynar

Kynar (polyvinylidene fluoride), also used in small-signal wire, thermally degrades primarily by dehydrofluorination with evidence of other degradative processes such as chain scission, cross-linking, cyclization and hydroperoxide formation.[10] The TGA of Kynar-51 and virgin polyvinylidene fluoride show that both have two regions of decomposition. There is the main pyrolysis region, which is due to loss of HF, and a second region which involves decomposition of the residual cross-linked polymer chains. The main degradation region is preceded by an induction period that is probably due to activation of the weak links in the polymer.

Figure 12 contrasts the thermograms of Kynar-51 and virgin polyvinylidene fluoride

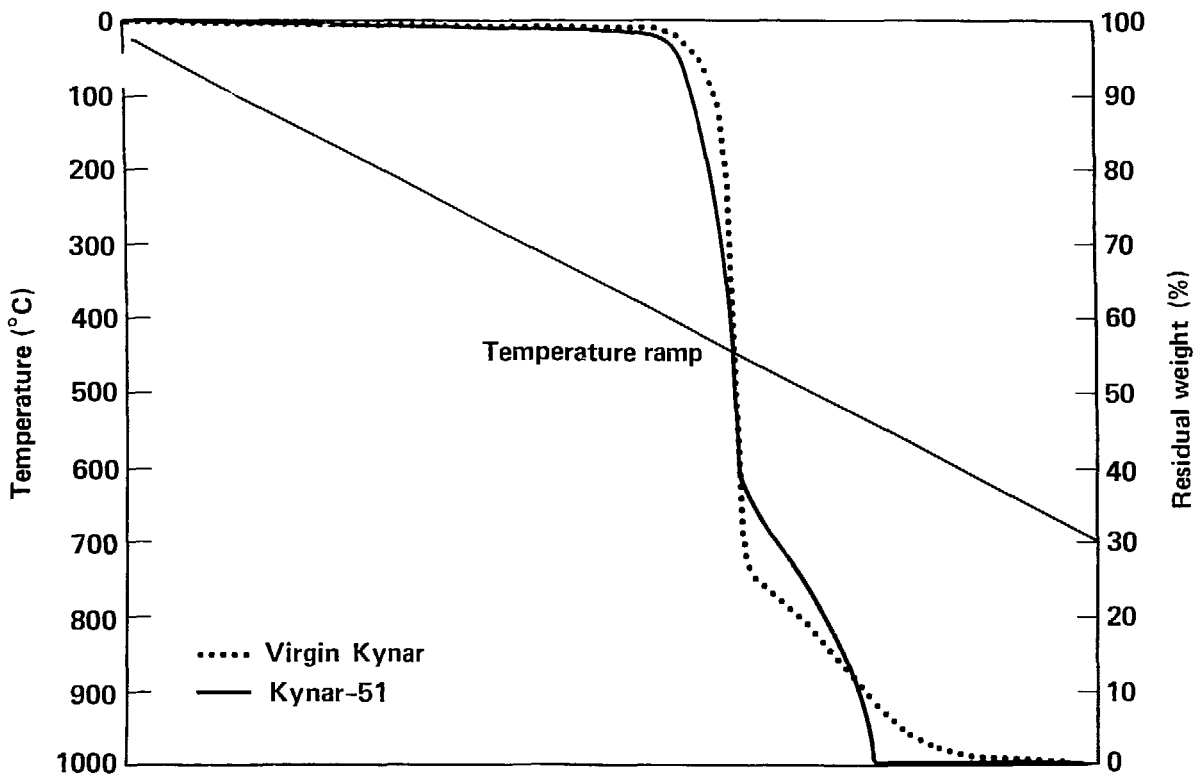

Figure 12. Thermogram of Kynar-51 and virgin Kynar heated in air at 20°C/min. See Figure 10 caption for the interpretation of the temperature rampline.

heated in air at 20°C/min. We see that the main degradation phase for Kynar-51 shows a lower overall weight loss and a lower rate of weight loss than virgin polyvinylidene fluoride.

The effect of heating rates on the degradation of Kynar-51 and virgin polyvinylidene fluoride is summarized in Table 7. As expected, the higher heating rates lead to higher degradation rates and therefore faster production of HF. We found that heating rates below 160°C/min do not effect the temperature responsible for the onset of the induction phase of virgin polyvinylidene fluoride. At 160°C/min, the temperature leading to the induction phase of virgin polyvinylidene fluoride is considerably lower than that observed with the lower heating rates. The induction phase of Kynar-51 occurs at a higher temperature at higher heating rates up to a heating rate of 160°C/min, at which rate the induction phase occurs at a considerably lower temperature. The effect of heating rates is inconsistent on the main phase pyrolysis of both the Kynar-51 and the virgin polyvinylidene fluoride samples.

Figure 13 shows the DSCA results of polyvinylidene fluoride and Kynar-51. Virgin polyvinylidene fluoride shows an endotherm at 150°C due to the polymer melting, an endotherm at 375°C in the realm of the induction phase, an exotherm at 442°C in the beginning of the dehalogenation region, and an exotherm at 455°C where the degradation of the residual cross-linked polyol begins. Kynar-51 shows an endotherm at 149°C due to melting, an exotherm at 390°C due to the beginning of dehalogenation region, and an exotherm at 445°C at the beginning of the degradation of the residual polymer.

HF is the dominant gas evolved from degrading virgin polyvinylidene fluoride and Kynar-51 at both medium and high temperatures. Other gases formed from virgin polyvinylidene fluoride and Kynar-51 at both the medium- and high-temperature pyrolysis are methane, ethylene, acetylene, ethane, propane, propylene, propyne, isobutane,

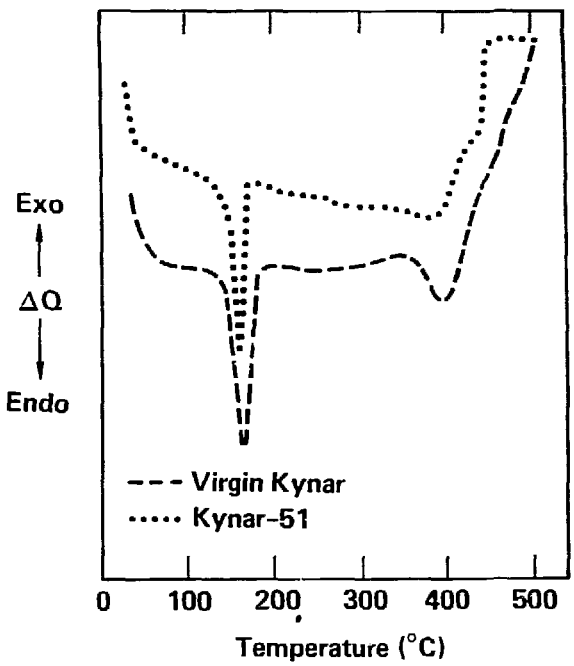

Figure 13. DSCAs of Kynar insulations heated in air at 20°C/min.

Table 7. The effect of heating rate on thermal degradation of Kynar.

Sample	Heating rate (°C/min)	Onset of induction phase (°C)	Onset of main phase (linear region) (°C)	Degradation rate in main phase (%/min)	Onset of phase-II (linear region) (°C)	Residual wt. at end of pyrolysis (%)
Virgin	10	330	420	24	470	0
Polyvinylidenefluoride	20	320	445	88	501	0.5
	40	335	395	80	475	0
	80	330	380	>100	460	0
	160	150	400	>100	500	0
Kynar	10	90	422	35	473	0
	20	165	420	39	500	0
	40	245	420	>100	500	1.0
	80	300	430	>100	525	1.75
	160	170	410	>100	530	1.75

n-butane, 1-butene, isobutylene, trans-2-butene, ethylacetylene, 1.3-butadiene, and pentane.

The liquid pyrolyzate from virgin polyvinylidene fluoride heated at medium temperature yielded a highly complex mixture, consisting of at least 50 compounds, of which only 5 components were identified. We identified 1-H-perfluorohexane, ethylacetate, 1,1,1,3,3-pentafluoropropene, 2-methoxy diphenyl ether, and 1,1,1-trifluoroethane. High-temperature pyrolysis also yielded a complex mixture, most of which was not identified, but which matched those found in the medium-temperature pyrolyzate.

The liquid pyrolyzate from Kynar-51, generated at medium temperature, rendered the following compounds: 1-H-perfluorohexane, borneol, di(trifluoromethyl) furan, methylphenylacetate, farnesol, n-butyl-o-phthalate, 4-carboxybenzophenone, and other unidentified components. High-temperature pyrolysis yielded 3-bromo-3,3-difluoro-1-propene, tetrafluoro-2-methylpentane, 4-methoxy-diphenyl ether, 2(trifluoromethyl) propene, 1,1,2,2-tetrafluoropropane, hexafluoro-tert-butyl trifluoroacetate, 1,1,2,2,3,3,4,4-octafluoropentane, and a number of unknown compounds.

Additional GC/MS Results on FY 82 Pyrolyzates

PVC

Table 8 lists additional degradation products identified this year for the FY 82 materials tested previously. The products were generated at medium temperature or at the temperature responsible for the dehalogenation region, and were separated on an SE-54 fused-silica capillary column.

High-temperature pyrolysis of virgin PVC, PVC-3, PVC-78, and PVC-104 produced high concentrations of ethylene, acetylene, ethane, propane, propylene, propyne, n-butane, 1-butene, isobutylene, and ethylacetylene. The amount of the gaseous hydrocarbons in all of the PVC samples was considerably higher at this temperature than those formed at medium temperature.

Table 9 lists the constituents of the liquid pyrolyzates generated at high temperature separated on both the Carbowax-20M and the SE-54 columns. Both columns indicated that the liquid pyrolyzate consists primarily of aromatic components which are largely the secondary decomposition products of PVC. In addition to the aromatic compounds formed directly from the decomposing plastics, degradation products are also formed from the plasticizers such as phthalic anhydride, di-(2-ethylhexyl) phthalate, phthalic acid, dibutyl phthalate, and stearic acid.

Rubber

High-temperature pyrolysis of Neoprene-G07, -84, and -435 resulted in a substantial increase in the production of the these hydrocarbons: ethylene, acetylene, ethane, propane, propylene, propyne, n-butane, 1-butene, isobutylene, cis-2-butene, trans-2-butene, ethylacetylene, pentane, and a number of other unidentified hydrocarbons.

GC/MS results of the liquid pyrolyzates generated from Neoprene are listed in Table 10. The constituents are mainly chlorinated and non-chlorinated aromatics, originating from the degrading plastics, as well as phthalates which are degradation products of the plasticizers used in the formulations. The main difference between these high-temperature degradation products and those from medium-temperature pyrolysis is a reduction in the quantity of liquid pyrolyzates, particularly in the lower-molecular-weight compounds.

The SE-54 results at medium temperature for rubber-134 and -138 show mainly higher molecular weight aliphatic hydrocarbons, aliphatic alcohols, naphthalene, benzoic, and phthalic acids for rubber-134; those from rubber-138 are predominantly aromatic.

High-temperature pyrolysis of rubber-12, rubber-134, rubber-138, rubber-1132, and rubber-1138 again produced large amounts of the C_1-C_5 hydrocarbons: methane, ethylene, acetylene, propane, propylene, propyne, isobutane, n-butane, 1-butene, isobutylene, trans-2-butene, 1,3-butadiene, and pentane.

The constituents of the liquid pyrolyzates from the rubbers are aromatic esters, aldehydes, ketones, and variously substituted benzenes (Table 11). In addition, degradation products from the plasticizers include such as palmitic acid, dioctylphthalate, n-amylphthalate, phthalic anhydride, butylmethylphthalate, and n-butyl-o-phthalate. The overall effect of the high-temperature pyrolysis on the liquid degradations products is that the pyrolyzate formed at high temperature is composed mainly of aromatic components as opposed to the low-temperature pyrolyzate which is comprised of both aliphatic and aromatic constituents.

Polyethylene

High-temperature pyrolysis of polyethylene yielded a considerable increase from medium-temperature pyrolysis in the production of ethylene, acetylene, ethane, propane, propylene and

Table 8. Newly identified degradiation products from pyrolysis of PVC a generated at medium temperature and separated on SE-54 fused-sileca capillary column.

T_R[a] (min)	Virgin PVC	T_R (min)	PVC-3
3.0	m-xylene	3.9	pinocamphene
3.7	n-propylbenzene	4.0	ethyltoluene
4.4	2,2,5-trimethylhexane	4.5	propenylbenzene
4.7	2,2,3,3-tetramethylpentane		
4.8	methylstyrene		
5.0	2,2,5,5-trimethylhexane		
5.1	2,2,4-trimethylheptane		
9.5	3-methylindane		
12.3	1,1,2-triphenylethane		

T_R (min)	PVC-78	T_R (min)	PVC-104
3.6	phenylacetaldehyde	3.6	phenylacetaldehyde
3.9	ethyltoluene	3.9	ethyltoluene
4.6	propenylbenzene	4.6	propenylbenzene
5.1	1-phenyl-1-nitroethane	5.1	1-phenyl-1-nitroethane
5.4	m- and p-ethylstyrene	5.4	m- and p-ethylstyrene
6.1	1-methylindane	6.1	methylallylbenzene
6.5	methyl-1-indene	6.3	1-methylindane
6.9	naphthalene	6.5	methyl-1-indene
8.2	benzoic acid	6.8	naphthalene
		8.5	methylnaphthalene
		10.6	3-benzyl-6-bromo-3,4-dihydro-2-H-1,3-benzoin
		11.1	4-methyl-2,6-di-tert-butylphenol
		12.8	2,5-di-tert-amylquinone

[a] Retention times (inTables 8-14).

Table 9. Pyrolysis products of PVC materials generated at high temperature, separated on the Carbowax-20M and SE-54 columns.

Insulation	T_R (min)	Carbowax-20M	T_R (min)	SE-54
Virgin PVC	3.7	1-methyl-2-ethylbenzene	3.2	6,6-dimethylfulvene
	4.8	m-methylstyrene	3.7	phenylacetaldehyde
	6.5	styrene	4.0	methyltoluene
	7.4	3-methylindene	4.5	2,2,4-trimethylheptane
	8.8	naphthalene	4.8	o-methylstyrene
	10.0	1-methylnaphthalene	5.4	2,5-dimethylheptane
	11.1	biphenyl	5.5	2-methylindane
	11.5	1,3-dimethylnaphthalene	6.4	methylallylbenzene
	11.9	2-ethylnaphthalene	6.6	1,2-dihydronaphthalene
	14.0	allylnaphthalene	7.1	azulene
	14.5	fluorene	8.2	3-methyl-1,2-dihydronaphthalene
	17.6	phenanthrene	8.6	2-methylnaphthalene
	19.1	4-methyl phenanthrene	8.9	1-methylnaphthalene
	22.8	1,2,3,4-tetrahydrofluoranthene	9.9	acenaphthene
	24.1	dioctylphthalate	14.8	phenanthrene
	24.7	fluoranthene	16.2	2-methyl anthracene
	26.4	5,6-benzo-7-phenylbicyclo (2,2,1) hept-2-ene		
PVC-3	3.6	xylene	4.1	ethyltoluene
	4.4	p-ethyltoluene	4.9	propenylbenzene
	5.1	isopropyl benzyl heptane	6.4	allyltoluene
	9.6	naphthalene	7.1	naphthalene
	10.8	1-methylnaphthalene	8.9	methylnaphthalene
	11.9	1-ethylnaphthalene	9.6	phthalic acid
	12.1	phenol	16.5	butyl phthalate
	12.2	biphenyl		
	15.3	phthalic anhydride		
	15.5	2-hydroxy-4-methoxy-6-methylbenzaldehyde		
	15.9	ethylene glycol dibenzoate		
	18.7	dibutyl phthalate		
	20.4	4-methylphenanthrene		
PVC-78	7.9	1-phenyl-1,2-propandione	4.5	isooctyl alcohol
	8.8	naphthalene	7.1	azulene
	10.4	1-methylnaphthalene	8.7	benzoic acid
	11.4	biphenyl	9.0	1-methylnaphthalene
	11.9	1,2-dimethylnaphthalene	10.0	phthalic anhydride
	14.4	phthalic acid	17.4	di-(2-ethylhexyl) phthalate
PVC-104	3.5	o-xylene	3.1	6,6-dimethyl fulvene
	3.9	isopropylbenzene	3.7	phenylacetaldehyde
	4.1	styrene	3.9	benzyl ester
	9.5	naphthalene	4.1	isopropylbenzene
	10.9	1-methylnaphthalene	4.9	methylstyrene
	12.1	phenol	5.6	o-allyltoluene
	18.6	anthracene or phenanthrene	11.4	2,6-di-tert-butyl-4-methyl phenol
			16.7	stearic acid

Table 10. Pyrolysis products of Neoprene generated at high temperature and separated on the Carbowax-20M and SE-S4 columns.

Insulation	T_R (min)	Carbowax-20M	T_R (min)	SE-54
Virgin Neoprene	3.6	o-xylene	3.1	6,6-dimethylfulvene
	3.7	chlorobenzene	3.9	n-proplybenzene
	4.0	1-methyl-3-ethylbenzene	4.6	acetophenone
	4.9	m-chlorotoluene	4.9	propenylbenzene
	5.6	m-methylstyrene	5.6	x-chloro-o-xylene
	6.0	o-chloroethylbenzene	6.1	2-phenylpropanol
	6.6	4-chloro-m-xylene	6.4	7-methylbenzo(β)furan
	8.3	1-methyl-1H-indene	7.9	benzoyl chloride and others
	9.7	naphthalene		
		1-methyl naphthalene		
Neoprene-007	3.8	o-xylene	3.1	n-butyl chloroacetate
	4.8	methylbenzoate	3.3	2-nonynic acid
	5.7	m-chlorotoluene	3.7	benzyl chloride
	6.4	indane	3.8	n-propylbenzene
	6.8	o-chloroethylbenzene	4.0	2-(1-phenylethylthio) phenol
	8.0	4-methylindane	4.4	3-methyl-1,4-heptadiene
	9.1	1-methyl-1-H-indene	4.7	indane
	9.9	chloroprene dimer	5.0	o-chloroethylbenzene
	10.5	naphthalene	5.4	m- and p-ethylstyrene
	12.1	2-methylnaphthalene	6.3	methylindane
	21.1	phenyl B-naphthylamine	8.7	methylnaphthalene
			12.3	allylnaphthalene
			12.8	diphenylmethane
			15.2	8-hydroxymethylquinoline
Neoprene-84	3.7	x-xylene	9.8	2,3-dimethyl-1,2,3,4-tetra-hydronaphthalene
	4.6	1-methyl-3-ethylbenzene		
	12.5	benzothiazole	25	di-(2-ethylhexyl) phthalate
	12.7	phenol		
	13.5	x-cresol		
	15.8	phthalic anhydride		
	29.8	dioctylphthalate		
Neoprene-435	3.9	x-xylene	3.1	6,6-dimethyl fulvene
	4.4	1-methyl-3-ethylbenzene	3.8	benzyl chloride
	5.3	benzyl chloride	3.9	n-propyl benzene
	5.9	B-methylstyrene	4.1	benzyl benzoate
	7.2	methylphenylacetylene	4.8	indane
	7.6	x-methylindane	6.4	5-methylindane
	8.7	methyl-1-indene	7.1	azulene
	9.5	chloroprene dimer	12.6	allylnaphthalene
	10.1	naphthalene		
	11.4	methylnaphthalene		
	12.4	ethylnaphthalene		
	14.1	acenaphthene		
	15.4	1-allylnaphthalene		

Table 11. Pyrolysis products of rubber generated at high temperature and separated on the Carbowax-20M and SE-54 columns.

Insulation	T_R (min)	Carbowax-20M	T_R (min)	SE-54
Rubber-12	4.3	styrene	7.1	azulene
	5.2	phenylacetylene	18.0	di-N-amylphthalate
	5.4	o-methylstyrene		
	6.7	1-chloroindane		
	8.0	methyl-1-indene		
	9.6	naphthalene		
	11.2	2-methylnaphthalene		
	12.2	biphenyl		
	12.5	p-isopropenylacetophenone		
	14.1	biphenylene		
Rubber-134	3.3	ethylbenzene	3.1	1,2-dimethyl-3-ethylbenzene
	4.3	styrene	4.1	1-phenyl-1-nitroethane
	8.2	methyl-1-indene	5.4	1-chloroheptadecane
	8.6	isobutylphenone	9.6	phthalic anhydride
	9.6	napthalene	27.7	butylmethyl phthalate
	10.9	1-methylnaphthalene		
	12.0	phenol		
	12.2	biphenyl		
	15.9	benzoic acid		
Rubber-138	3.3	1,2-dimethylbenzene	3.2	cyclotetracene
	4.3	benzocyclobutane	3.5	isopropylbenzene
	4.6	allylbenzene-1-phenyl-1-nitroethane	3.8	phenylacetaldehyde
	5.7	phenylcyclopropane	3.9	1-methyl-2-ethylbenzene
	7.1	benzaldehyde	4.2	isopropylbenzene
	8.1	1-methyl-1H-indene	4.4	methylstyrene
	8.5	acetophenone	4.9	propenylbenzene
	9.2	azulene	5.1	chlorindene
	9.6	naphthalene	6.6	1,7-ethene-spiro-(2,6)mono-4,8-diene-2,8-lactone
	10.0	β-phenylethyl acetate		
	11.3	methylnaphthalene	7.1	naphthalene
	11.8	benzothaozole	9.1	β-phenylethyl acetate
	12.0	phenol	9.9	acenaphthene
	12.3	biphenyl	13.2	1,3-diphenylpropane
	13.5	β-phenylethylformate	17.6	dioctylphthalate
	14.1	biphenylene	30.0	di-(-2-ethylhexyl)phthalate
	14.9	1,3-diphenylpropane		
	15.9	1,2-benzoloxybutane		
	21.7	palmitic acid		
Rubber-1132	4.8	styrene	3.2	6,6-dimethylfulvene
	9.0	1-phenyl-1,2-propandione	3.9	ethyltoluene
	10.0	naphthalene	4.9	allylbenzene
	11.3	methylnaphthalene	7.1	azulene
	12.3	phenol	9.8	phthalic anhydride
	15.5	Phthalic anhydride	17.7	d-n-amyl phthalate
	16.0	benzoic acid	20.8	amyl phthalate
	20.7	3-cyclopentyl-2',4'-di-methylphenone	22.6	isobutyl-o-phthalate
	24.7	methyl-3-(2,5-dimethybenzoyl) butanoate	25.4	isopropyl phthalate
	26.4	butyl phthalate		

Table 11. (Continued)

Insulation	T_R (min)	Carbowax-20M	T_R (min)	SE-54
Rubber-1138	3.4	xylene	3.2	styrene
	3.7	1,2,3,4-tetramethylbenzene	3.4	isopropylbenzene
	4.3	styrene	3.8	phenylacetaldehyde
	6.0	cyclopropylbenzene	4.2	alpha-methylstyrene
	7.1	benzaldehyde	4.8	allylbenzene
	8.6	methylphenylheptane	5.2	n-butylbenzene
	9.6	naphthalene	6.6	n-phenylbenzene
	11.2	methylnaphthalene	13.2	1,3-diphenylpropane
	12.0	phenol	18.5	n-butyl-o-phthalate
	12.3	biphenyl		
	14.9	1,3-diphenylpropane		

propyne. Liquid pyrolyzates generated at high temperature consist mainly of aromatic compounds and high-molecular-weight aliphatic hydrocarbons (Table 12).

Polyurethane

High-temperature pyrolysis did not produce any detectable effect on the generation of C_1-C_4 hydrocarbons (Table 13). The mixture consisted of various aromatic compounds. The main difference between medium-temperature and high-temperature pyrolysis is that the pyrolyzate generated at high temperature consists of a wider variety of products. Some of these products are halogenated, which are probably degradation products of a flame retardant used in this formulation.

Nylon

Both the medium- and high-temperature pyrolysis of nylon rendered the following hydrocarbons: methane, ethylene, acetylene, ethane, propane, propylene, propyne, isobutane, n-butane, 1-butene, isobutylene, cis-2-butene, trans-2-butene, ethylacetylene, 1,3-butadiene, and pentane. High-temperature pyrolysis affects the production of the minor constituents of the liquid pyrolyzate rather than changes the general mechanism of degradation. High temperature generated larger amounts of n-butane, 1-butene, and isobutylene than medium temperature. The liquid pyrolyzate generated at high temperature, as opposed to that from medium temperature, again consisted primarily of caprolactam and low amounts of minor constituents comprised of creosol, 2,5-dimethylbenzene, 2,-5-dimethylbenzoate, methyl-3-butanoate and tetrahydro-quinoline.

Mylar

Table 14 compares high-temperature pyrolysis of polyethylene terephthalate with Mylar. Similar amounts of C_1-C_3 products are produced at both medium and high temperatures, however, polyethylene terephthalate forms large amounts of C_4-hydrocarbons at both medium and high temperatures, such as n-butane, 1-butene, isobutylene, cis-2-butene, and trans-2-butene.

Conclusions

High-temperature pyrolysis leads to formation of large amounts of light hydrocarbons as well as to production of substantial amounts of aromatic species. Our results from *FY 83* confirmed earlier findings in that all the insulations we investigated form detectable amounts of light hydrocarbons upon smoldering or flaming combustion. These are detected in the very early degradation stages of the samples pyrolyzed either under controlled laboratory conditions or ignited in the large-scale test cell. Such information is useful for selecting or designing appropriate early warning alarm systems for buildings housing costly equipment. Also, the extensive GC/MS analysis of the liquid pyrolyzates confirmed that this information can aid in isolating insulations which incorporate flammable plasticizers.

Table 12. Pyrolysis products of polyethylene generated at high temperature and separated on the Carbowax-20M column.

Insulation	T_R (min)	Carbowax-20M
Virgin polyethylene	5.3	1,3-dimethyl-4-cyclopentane
	7.2	1-hexadecene
	?	naphthalene
	?	1-methyl-2-cyclohexylcyclohexane
	10.4	x-methylnaphthalene
	10.6	o-nenthane
	11.4	phenylbenzene
	11.6	methyldicyclohexylmethane
	12.4	acenaphthene
	13.2	biphenylene
	13.6	1,1-dicyclohexylpentane
	22.9	dihexyldiacetylene
	25.0	dioctylphthalate
Polyethylene-77	3.7	styrene
	6.1	1-methylphenylacetylene
	8.9	naphthalene
	10.2	hexahydrofarneool and methylnaphthalene
	10.5	3-methylpentine
Polyethylene-95	3.1	undecanol-1
	4.1	oct-1-ene
	5.3	acetic acid
	6.4	4,6,8-trimethylnonene-1
	7.7	2,2-dimethyl-1-acetylcyclopentane
	7.8	1-hexadecene

Table 13. Degradation products from pyrolysis of Polyurethane-89 separated on the Carbowax-20M and SE-54 columns.

T_R (min)	Carbowax-20M	T_R (min)	SE-54
3.1	o-xylene	3.0	phenylacetylene
3.3	chlorobenzene	3.2	1,2-dimethyl-3-ethylbenzene
3.6	styrene	3.5	bicyclo (5-10) oct-3-ene
4.4	1,4-dichlorobutane	3.9	benzotriazole
4.6	phenylacetylene	4.3	benzamide
5.6	di-(4-chlorobutyl) ether	4.7	4-methylstyrene
5.9	indene	4.9	methylphenylacetylene
8.5	1,2,3,4-tetrachlorocyclopenta-1,3-diene	5.2	4-methyl-1-aziridinecarboxanilide
8.9	naphthalene	6.8	naphthalene
9.3	4-heptanol	8.6	methylnaphthalene
10.1	2-methylnaphthalene	9.8	di-(4-chlorobutyl) ether
11.0	bis (4-chlorobutyl) ether	10.5	biphenyl
12.4	benzyl bromide	14.3	phenanthrene
13.3	biphenyl		
13.5	methyl quindine		
16.7	n-butyl-N-phenylcarbonate		
17.7	phenanthrene		
23.4	pyrene		
25.3	fluoranthene		
26.5	azidobiphenyl		

Table 14. Pyrolysis products of mylar and polyester generated at high temperature and separated on the Carbowax-20M and SE-S4 columns.

Insulation	T_R (min)	Carbowax-20M	T_R (min)	SE-54
Mylar-139	3.3	octadecanol-1	3.2	2-tert-butyl-4-methylfuran
	8.7	naphthalene	3.6	4-methyl-2-heptanone
	24.7	dioctylphthalate	3.9	1,2,4-trimethylbenzene
			4.2	6-methyl-1-heptanol
			4.8	1-methylphenylacetylene
			6.7	azulene
			23.3	dioctylphthalate
Polyethylene terephthalate	3.6	styrene	3.2	cyclooctatetraene
	5.1	methylstyrene	3.9	benzaldehyde
	5.3	acetic acid	4.2	methylstyrene
	6.3	benzaldehyde	6.2	methyl benzoate
	7.0	m-divinylbenzene	10.1	benzoic acid
	7.5	methyl benzoate	10.5	p-methyl benzoic acid
	7.9	ethyl-2-keto-2-phenylethanoate	11.5	ethylbenzoic acid
	8.1	ethyl benzoate	13.4	methyl terephthalate
	10.2	methyl-3-(2,5-dimethyl benzoyl) butanoate	18.1	phenyl benzoate
	11.5	biphenyl		

Reliability Study on the LLNL Water-Supply System

With this section, the reliability analysis of fire-sprinkler systems, a major portion of our fire-risk analysis which began in FY 80, is completed. This reliability study illustrates the application of a powerful analytical tool called digraph-fault-tree methodology.[11] Although it is specifically applied to the LLNL water-supply system, this methodology is ideal for complex systems analyses of large facilities or technologies such as special nuclear materials' safeguards, nuclear-power-plant cooling systems, large-research-facility control systems, large-experiment designs, fire-protection systems, etc. Dunglinson *et al.* not only describes the technique in detail but also presents examples of actual studies in the chemical process industry.[12]

There are a number of disadvantages and deficiencies in traditional fault-tree analysis that digraph alleviates. Since a detailed report will be published in the near future, we will present a summary of the digraph-fault-tree study. We analyzed the reliability of the Mocho water-supply system, LLNL's primary water supply, to establish whether adequate water would be available in the event of a major fire. The digraph procedure generated a fault tree of the water-supply system. The initiating-enabling-event-interval reliability approach is used to perform a probablistic evaluation of the fault tree and to compute various system reliability characteristics, such as the unavailability of the water-supply system in the event of a major fire.[12]

Mocho Water Supply and LLNL Monitoring System

Figure 14 shows the water-supply system to LLNL. The main source of water to LLNL is the Hetch Hetchy Aqueduct, located 800 ft below ground level at the Mocho Pumping station, which is located 8 mi south of LLNL (Site A). The water is first pumped to the surface and into the standpipes (Site B). The purpose of the standpipes is to prevent water hammer at pump discharge. These two standpipes have a capacity of 20,996 gallons each. The water flows by gravity from the standpipes to three main storage tanks (Site C) located 1/2 mi south of LLNL on the hill above Sandia National Laboratories (SNL). Three storage tanks have a total capacity of 1,238,800 gallons (Site C). The storage tanks provide the head

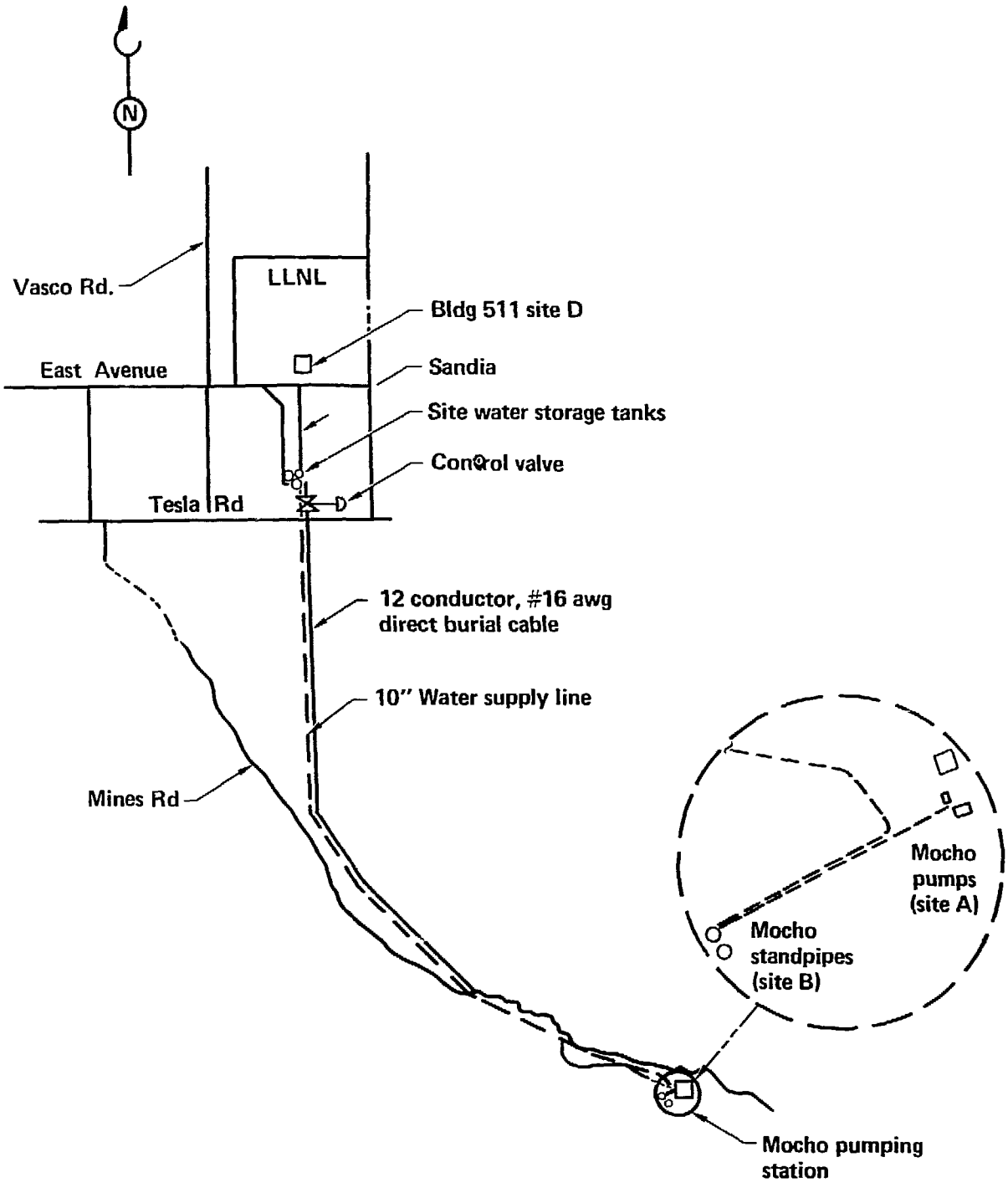

Figure 14. Site plan of existing system.

pressure necessary to supply LLNL. The tanks and standpipes are all at atmospheric pressure. The Central Control Room for the system is located on-site in Bldg. 511 (Site D).

As an alternate or standby water supply, LLNL has water available from the Zone 7 water district. This water supply is used only during times when Hetch Hetchy water is unavailable due to tunnel maintenance, pump failure at the Mocho Pumping Station, or line failure between the Mocho standpipes and the storage tanks. Personnel on-site must activate the Zone 7 water supply manually.

Figure 15 is a simplified schematic of the LLNL water-control system. The system consists basically of two feedback subsystems: (1) the water-level control for the Mocho standpipes and (2) the water-level control for the storage tanks. Any two of the three pumps at Site A controls the water level in the standpipes. Water level in the storage tanks is controlled by opening a valve that causes the Mocho standpipes to drain (Site B). Gravity feeds water as needed to LLNL from the storage tanks. Alarms, status indicators, and control signals are transmitted via frequency division multiplexed frequency shift tone equipment. Selector switches, relays, water-level meters, and pilot lights display the data being transmitted and received on a control console in Bldg. 511 (Site D). Manual commands from the control console can open or close valves at the water-storage tanks, and start and stop pumps at the Mocho pumping station. The water level in the standpipes and storage tanks is continuously monitored in Bldg. 511. Any abnormal condition, such as a high- or low-water level in the storage tanks or in the standpipes, or any pump failure, initiates an au li-ble and visual alarm on the control console.

Analysis of the Mocho System

We first had to understand and model the components of the water-supply-control system. Digraph-fault-tree analysis uses steps common to traditional fault-tree analysis. In assessing the Mocho water-supply system in the event of a major fire, we found that 16 single events would cause the control loop that monitors storage tank level to fail. These failures would go undetected in Bldg. 511 because the feedback loop performs both control and detection functions. Based on this, we recommend that each tank have its own independent water-level sensor. If this is done, then we estimate that system availability would increase by a factor of 50. Restoring this independent measurement would result in no single event minimal cut sets in the system in which failures would go undetected.

We will briefly describe the digraph-fault-tree methodology used to arrive at our recommendations.

Defining the Top Event

The Top Event in this analysis is "Insufficient Supply of Water in Storage Tanks and No Detection of Same in Bldg. 511." Note that we did not consider earthquake effects on the Mocho system.

Based on firefighting experience in the chemical industry, LLNL's Fire Safety Division defined the amount of water necessary to extinquish a major fire on-site: a continuous flowrate of 3500 gallons per minute (gpm) for 4 hours, for a total of 840,000 gallons. Besides, the 1,283,800-gallon capacity of the three storage tanks, standpipes A and B contain 41,992 total gallons, and 180,180 gallons also sit in the line from the standpipes.

In addition, we must include the makeup capacity of the two Mocho pumps (1 lead and 1 lag) during this 4-hour period. The lead pump, No. 3, has a capacity of 1100 gpm; each of the lag pumps, No. 1 or 2, has a 500-gpm capacity. In 4 hours, there is a total capacity of 1600 gpm, or 384,000 gallons. Therefore, the total capacity of the whole system plus makeup is 1,889,972 gallons.

During 1981, the maximum daily water consumption was 950,000 gallons. Subtracting this amount from the Mocho system capacity leaves 939,972 gallons to fight a major fire, which exceeds the recommended 840,000 gallons. If the system is working, then an adequate supply of water will be available for the postulated fire.

In the 15 years the Mocho system has been operating, the storage tanks have drained dry twice due to human error. Such errors will lead to an inadequate supply of water in the storage tanks, and no one will detect it in Bldg. 511. Since the total of the pump makeup plus the standpipes and the line from the standpipes is only 606,000 gallons, at least an additional 234,000 gallons must be in the storage tanks to meet the 840,000-gallon requirement (840,000 − 606,000 = 234,000). Therefore, if the level in the storage tanks drops below 234,000 gallons, there will not be enough water to extinquish the fire.

A low-level condition in the tanks generates an alarm in Bldg. 511. Depending on the event(s) that caused the low level, LLNL personnel will take the appropriate measure, such as activating Zone 7 supplies.

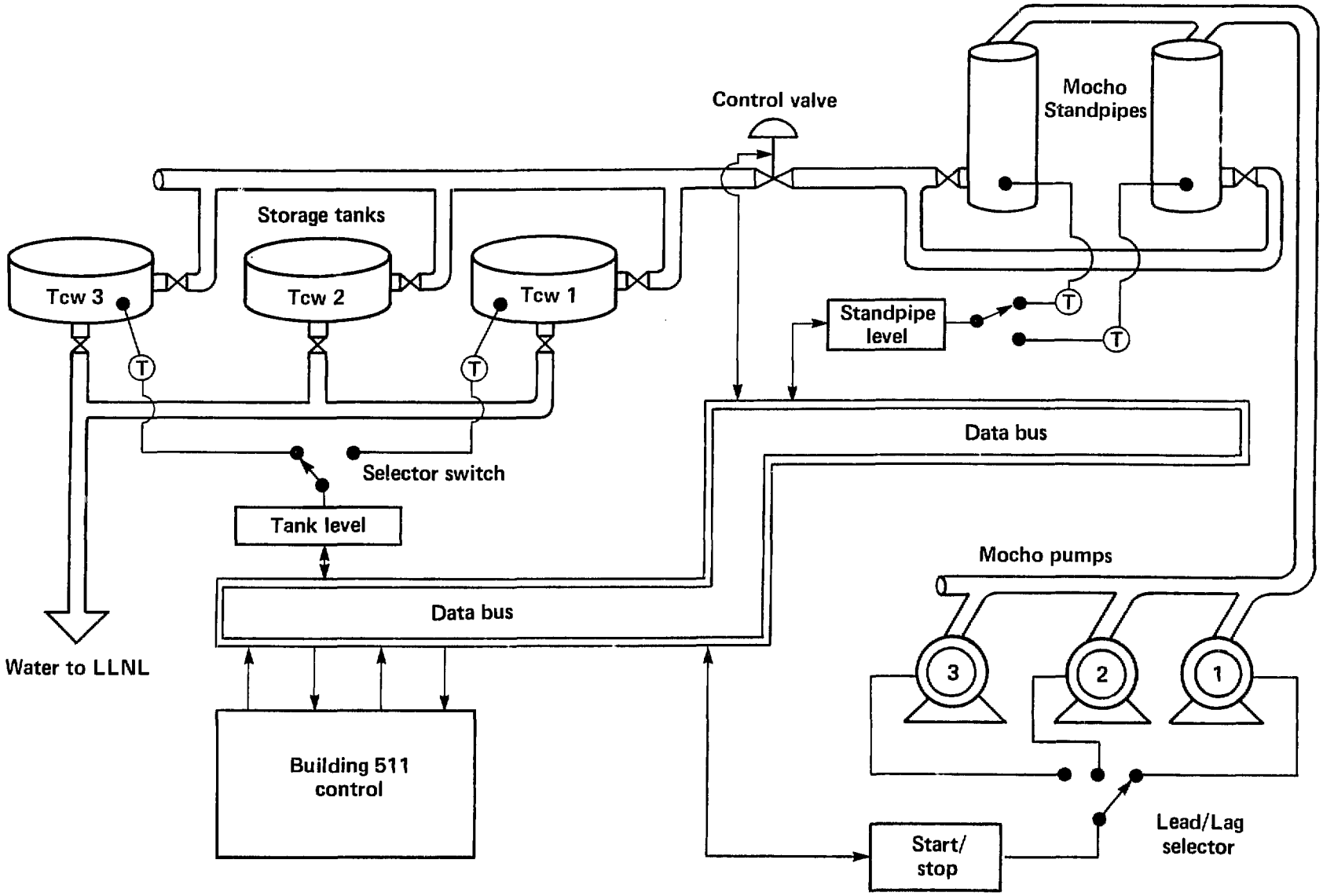

Figure 15. Mocho-water control system.

Understanding the Water-Supply System

By taking tours of the entire water-supply system and interviewing LLNL personnel familiar with the system, we identified the following information, germane to digraph-fault-tree analysis.

The independent measurement of water level in the storage tanks was removed which left only one sensor for three tanks. Pump No. 3, an 1100-gpm pump, is the lead pump; a 500-gpm pump is the lag pump. In a No. 3-failure, either No. 1 or No. 2 becomes the lead pump. A visit to the Site A pumps is required in the event of a No. 3-failure. With No. 3 out of service, the water makeup to the standpipes takes longer but the system can be successfully operated in this mode. The main water valve will not open if the standpipe is in a low-water alarm condition or if the water tanks are in a high-water alarm condition. A spurious signal for either of the above conditions will cause the main water valve to close, and this results in the storage tanks standing at low level. In the event of a complete failure of the Mocho system, it takes approximately 15 min to cut in the Zone 7 water supply. The existing controls for the Mocho system include over 100 mechanical relays for logic and timing. Understanding the operational sequence of the control system was important to analyzing its reliability in any detail.

Event Sequence for Storage-Level Control

Water usage by SNL or LLNL will cause the water level in the storage tanks to drop. When the water level drops to 12 ft–6 in., a water-pressure transducer causes the automatic water valve to open. When the valve opens, water begins to flow from the Mocho standpipes. This water flows into the top of the No. 2 storage tank that is connected to No. 1 and No. 3 through service valves located at the bottom of the tanks. Water continues to flow through the automatic valve and fill the three tanks until a level of about 14 ft is reached, at which time the automatic valve closes and no water flows.

Event Sequence for Standpipe-Level Control

As the automatic water valve at the storage tanks opens and water begins to flow from the Mocho standpipes, the water level in the standpipes drop. When this level drops to 12 ft–6 in., the No. 3 lead pump starts pumping into the top of No. 1 standpipe, connected by bottom piping to No. 2 standpipe, from which water flows to the storage tanks. However, water flows through the automatic water valve faster than No. 3 can pump, so the water level continues to drop. When the standpipe water level reaches 8 ft–8 in., the lag pump starts pumping. The combined output of both lead and lag pump is greater than the amount of water flow through the automatic valve, so the water level will now rise in the standpipe. When the water level reaches 12 ft–10 in., the lag pump drops out. It will, however, continue to cycle on when the standpipe level drops to 8 ft–8 in. and cycle off as the level rises to 12 ft–10 in. When the automatic water valve at the storage tanks closes, the level in the standpipe rises until it reaches 13 ft–5 in., at which point the lead pump cuts off and everything comes to a rest.

Failure Modes and Effects Analysis

We performed a detailed Failure Modes and Effects Analysis (FMEA) on the Mocho system. LLNL personnel provided input for the FMEA. The results from this study provided much of the information to construct the digraph and fault tree and the probabilistic evaluation of the fault tree. The advantage of a FMEA is that LLNL personnel can provide information for the analysis without a knowledge of the digraph-fault tree procedure.

System Digraph

A digraph is a multivalued logic model useful in constructing fault trees of control systems. The digraph consists of nodes and edges (or arrows) that connect the nodes. A node represents a process variable and the edge represents the gain, or the relationship between the nodes. A top event is defined as a deviation, i.e., a disturbance and is the starting variable in the digraph. The digraph is constructed deductively, similar to constructing a fault tree. The limit of resolution in the digraph is equipment failure, human error, or environmental conditions.

The next step in the digraph procedure is to find the control loops in the digraph. A synthesis algorithm is devised to construct the digraph from the fault tree. Basically, the synthesis algorithm delineates how a control loop can cause or pass a disturbance resulting in the occurrence of the Top Event.

The advantages of constructing a digraph is that the topology of the system variables is displayed and that the digraph resembles the system schematic. In addition, the digraph can consider multivalued logic and timing. By contrast, a fault

tree bears no relationship to the schematic, and it is difficult to consider multivalued logic and timing in fault-tree analysis.

Digraph Construction

The system digraph constructed for our study is similar in scope to the system digraph made for the *LLNL Material Control Study.*[13] The purpose of a material-control system is the prevention of theft of Special Nuclear Materials (SNM), like plutonium, from nuclear facilities. The material-control system consists of procedures, monitors, computers, and a security force designed to stop theft, both covert and overt.

The LLNL study focused on covert threat via an insider problem, and a prototype facility, called the Test Bed, was designed.[13] The assessment of the Test Bed facility generated a system digraph with a Top Event Node, "Successful Theft of SNM from the Test Bed." Plutonium nitrate is stored in tanks that contained bubblers which measured static pressure or level. As the adversary attempts to steal SNM, the tank level should decrease and generate an alarm. As the adversary commits acts necessary to steal the SNM, a series of negative feedforward loops are activated, called cancellation loops. These loops generate a safeguards response in preventing the adversary from stealing SNM.

For the adversary to be successful, all these loops must fail. Failure can occur because of random monitor failure, inadequate monitor-measurement sensitivity, and adversary activity, including equipment tampering and collusion. The synthesis algorithm creates an AND gate in the fault tree each time a cancellation loop fails.

In the Mocho study, we are concerned with human error and/or equipment failure that causes a low water level in the storage tanks. Also, we are concerned with failure of LLNL personnel to take action when a low water level occurs. Hence, we see that the methodology used in generating the material-control digraph is applicable directly to our analysis of the Mocho system.

The Preliminary System Digraph

The preliminary system digraph shows the structure of the detailed system digraph (Fig. 16). The top event variable in the digraph is "Flowrate to LLNL." The cycles in the digraph show the two basic feedback loops: (1) the storage-tank-level-control feedback loop and (2) the standpipe-level-control feedback loop.

The sensed variable in both cases is static pressure and the manipulated variable is flowrate through the main control valve (for the storage tanks) or through the Mocho pumps (for the standpipes). An arrow from one variable (the independent variable) to the other variable (the dependent variable) indicates that a change or deviation in the independent variable causes a change in the dependent variable.

The Detailed Digraph

The detailed system digraph is segmented according to sites: Site A, the Mocho pumps; Site B, the Mocho standpipes; Site C, the storage tanks, and Site D, Bldg. 511. Each digraph was made using the control system schematic. Because of the magnitude of the detailed system digraphs, only Site B (the Mocho standpipes) is included as an example in Appendix B.

Fault-Tree Construction

Appendix C displays the fault tree. The causes are displayed for the Top Event:

- One or more storage tank drain valves closed and no detection of low storage tank level.
- Insufficient flow through control valve and no detection in Bldg. 5 1

Once, during the history of the system, a drain valve to a storage tank had been closed and the selector switch had not been changed to measure the water level in tank No. 1. This event caused the system to drain and simultaneously inactivated the control loop that operates the valve since a full tank was being monitored. Hence, the remaining two tanks drained with no detection in Bldg. 511. The event, excessive system demand, has been included in the fault tree for completeness. However, as described earlier, this event is no longer a possibility and so will be excluded from further consideration.

It is important to note that if the storage tank level feedback loop is inactive or out of tolerance, then low level will occur without detection level in Bldg. 511. This is because the feedback loop is used simultaneously to (1) control level in the storage tanks, and (2) to send a signal to Bldg. 511 in the event of low level. Hence, failure of the control elements on the feedback loop directly causes the top event to occur. If the control valve is open, and the loop fails out of tolerance, then the control loop will command the valve to close for a longer period of time than desired, resulting in low level in the storage tank. If the loop is inactive, then the control valve will fail to open when it should, again resulting in low storage tank level.

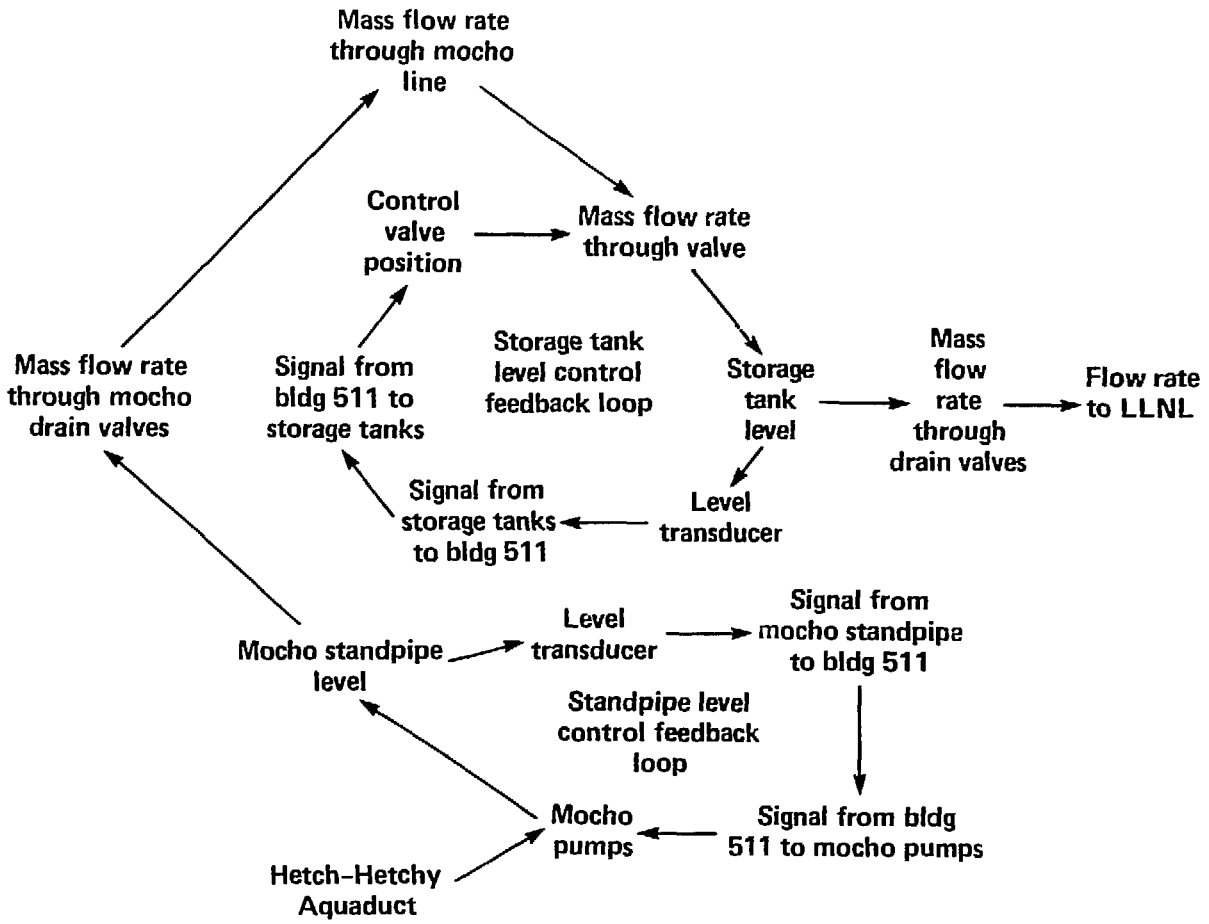

Figure 16. Preliminary system digraph.

A close-all-valve signal can result in the valve being closed too long. Two things can cause this:

- A spurious high storage tank level signal.
- A low standpipe level signal (generated either spuriously or due to actual failures that can cause low standpipe level).

The cause of low standpipe level can be due to the feedback loop being out of tolerance or inactive. Another cause of low tank level is an insufficient supply from the Mocho pumps. Note that we do not consider the case of drained Mocho standpipes. This is because a low standpipe level will cause the control valve to close and result in a low level in the storage tanks, which means that the fault tree logic for draining the standpipes will generate nonminimal cut sets since additional features must occur to drain the standpipes. However, we do consider draining the pipelines from the standpipes. This can occur by simply closing the drain valve in standpipe No. 2. Since the standpipe level is constant in this case, the valve will continue to remain open until the pipe from the standpipe is drained. Note that throughout the fault tree, that when a detection loop fails, an AND gate is generated. This is a result of the feedforward operator described in Lambert.[11]

Qualitative Fault-Tree Evaluation

The fault tree contains 98 basic events. In addition, there are a total of 640 minimum-cut (min-cut) sets. Min-cut sets are combinations of basic events that cause the Top Event to occur. Min-cut sets also are known as the system failure modes. The number of min-cut sets according to order is given below (order refers to the number of basic events in a min-cut set):

Order	1	2	3	4	5	6	7
Min-Cut Sets	16	19	134	244	163	56	8

The 16 single-event min-cut sets are single failures of control devices on the storage tank level feedback loop as described earlier. Of the 98 basic events, 72 are initiating events and 26 are enabling events. As described in Dunglinson *et al.*, enabling events inactivate system mitigative or protective features but do not cause the Top Event to occur.[12] For example, an inactive alarm or burned-out light does not cause low level but does fail the operator in the event of an alarm condition. For initiating events we must compute their frequency of occurrence, for enabling events, their demand unavailability when the initiating event occurs. Reliability data for the 98 basic events were obtained from actual system experience during the last 15 years.

For initiating events, we assume a fault duration time of 1 h. This includes the amount of time required for Bldg. 511 personnel to diagnose the cause of failure and take action after a failure of the Mocho system has occurred.

For the Top Event to occur, we assume no detection in Bldg. 511. However, low water pressure will be detected on-site. The 1-h fault duration time corresponds to the time after detection has occurred on-site. The fault duration time for enabling events, 0.13 years, corresponds to the average time a failure can exist with an inspection interval of three months.

Probabilistic Evaluation of the Fault Tree

We used the computer code, IMPORTANCE, to evaluate probabilistically the Mocho system fault tree.[14] The following probabilistic measures were computed for the Mocho system:

- Frequency of occurrence of initiating events,
- Frequency of occurrence and mean occurrence time when an insufficient supply of water exists in the system,
- Unavailability of the Mocho system when a major fire occurs, and
- Ranking of initiating events, enabling events and min-cut sets according to their probabilistic importance.

Probabilistic importance assesses the quantitative contribution of enabling events, initiating events, and min-cut sets to the occurrence frequency of the Top Event. A probabilistic ranking according to importance is necessary in identifying important contributors because it is virtually impossible for an analyst to visually inspect all the min-cut sets and to assess the relative contribution of a component to system failure. This is particularly true for the Mocho system whose fault tree contains 98 basic events and 640 min-cut sets.

Initiating-Event Fault Tree

One fault tree was generated by simply taking the Boolean union of all initiating events. Hence, this fault tree generated 72 single-event min-cut sets, since there were 72 initiating events. Table 15 displays the results of this fault tree. The Top-Event frequency of occurrence is 20.4 per year. We can think of this number as the number of challenges to the system yearly. This number is consistent with actual historical data. Table 15 also lists the ranking of initiating events through rank 9. We see that the following events are important:

- PG&E power failure.
- Oiler relay failure (at Mocho pumps).
- Noise on transmission line.

We assume that the dominant failure cause of the close-all-valves transmitter is noise on the line.

Mocho System Fault Tree

Table 16 lists the system-reliability characteristics of the Mocho system fault tree. We predict that, on the average of 3.1 times per year, the Mocho system will have an inadequate supply of water to extinguish a major fire at LLNL. It must be pointed out that this number corresponds to a low level in the storage and not necessarily to a totally dry condition. Another measure of system adequacy is the demand unavailability of the system given a major fire. The demand unavailability is calculated to be 3.6×10^{-4}. We compare this number to the actual historical data. During the 15-year life of the system, it has been dry twice. If we assume that the system was unavailable for 4 hours each time, this results in a system unavailability of (8 hours $\times$ 1 year/8760 hours) (system lifetime/15 years) $= 6.1 \times 10^{-5}$.

Since this number does not include other times in which the storage tanks might have been low rather than dry, we see that the calculated unavailability, 3.6×10^{-4}, agrees reasonably well with the historical data, 6.1×10^{-5}. Table 16 also ranks the initiating events through rank 9. We see that the basic events which are single-event min-cut sets rank the highest. The one exception is the PG&E power failure that requires failure of the backup-power supply system. These singles are

Table 15. Results from the initiating-event fault tree. The mission time is 15 yrs.

Rank	Basic event description	Importance	Failure rate per year	Mean fault duration (hr)
1	I-V-C1 PG&E power failure	0.232	5.00	1.00
2	I-P-A2 Oiler failure relay PCW #1	0.155	3.33	1.00
2	I-P-A1 Oiler failure PCW #3	0.155	3.33	1.00
3	I-V-D1 Close all valve transmitter failure on	0.464 E-01	1.00	1.00
3	I-V-D2 Noise on line to control valve transmitter	0.464 E-01	1.00	1.00
3	I-P-D1 Noise on line from standpipe to Bldg. 511	0.464 E-01	1.00	1.00
4	I-P-A2 Control power contacts R3-1 transfer open	0.218 E-01	0.47	1.00
4	I-P-A1 Control power contacts R9-1 transfer open	0.218 E-01	0.47	1.00
5	I-V-C1 High resistance WLT #1 transducer	0.186 E-01	0.40	1.00
5	I-P-B1 High resistance standpipe pressure transducer	0.186 E-01	0.40	1.00
6	I-P-B1 Farmers dig up transmission line	0.155 E-01	0.333	1.00
7	I-P-B1 Power supply Auto-Mod #9109 failure off	0.124 E-01	0.267	1.00
8	I-V-C1 Tank level module voltage high	0.617 E-02	0.133	1.00
8	I-V-D2 Valve module contacts open	0.617 E-02	0.133	1.00
8	I-P-D1 Pump switch module voltage high	0.617 E-02	0.133	1.00
8	I-P-B1 Module #514 voltage signal high	0.617 E-02	0.133	1.00
8	I-P-B1 Module #502 voltage signal high	0.617 E-02	0.133	1.00
8	I-P-A1 PCW #3 motor fails to function	0.617 E-02	0.133	1.00
8	I-V-D2 TCW S-tank level rec card voltage high	0.617 E-02	0.133	1.00
8	I-V-D1 Standpipe level module failure (on)	0.617 E-02	0.133	0.13 yr
8	I-V-D1 Tank level alarm module failure (on)	0.617 E-02	0.133	0.13 yr
9	I-P-A2 Pressure switch out of tolerance	0.311 E-02	0.670 E-01	0.13 yr
9	I-P-A1 Pressure switch out of tolerance	0.311 E-02	0.670 E-01	0.13 yr
9	I-V-C2 2400-Hz receiver fails low	0.311 E-02	0.670 E-01	1.00
9	I-V-C2 Valve stem failure	0.311 E-02	0.670 E-01	1.00
9	I-V-C1 Residual magnetism relay CR1	0.311 E-02	0.670 E-01	1.00
9	I-V-D2 Relay coil CR7 open circuit	0.311 E-02	0.670 E-01	1.00
9	I-V-C1 Open circuit relay CR1	0.311 E-02	0.670 E-01	1.00
9	I-V-D1 CR5-3 contacts close	0.311 E-02	0.670 E-01	1.00
9	I-P-D1 TSCW level receiver voltage high	0.311 E-02	0.670 E-01	1.00
9	I-P-A1 Lead pump receiver failure off	0.311 E-02	0.670 E-01	1.00
9	I-V-C1 Level transmitter fails low	0.311 E-02	0.670 E-01	1.00
9	I-P-D1 CR3-2 contacts transfer open	0.311 E-02	0.670 E-01	1.00
9	I-P-D1 CR1A-1 contacts transfer open	0.311 E-02	0.670 E-01	1.00
9	I-V-C2 Agastat TDR-4 contacts transfer open	0.311 E-02	0.670 E-01	1.00
9	I-V-D2 Flow valve selector switch opens	0.311 E-02	0.670 E-01	1.00
9	I-P-A1 PSR6 contacts transfer open	0.311 E-02	0.670 E-01	1.00
9	I-V-D1 CR2A-1 contacts close	0.311 E-02	0.670-01	1.00

Table 16. Ranking of initiating events (the conditions are listed below).

Insufficient level in storage tank and no detection
Mean time to system failure = 2847.6 Hours 0.32506 years
Mean time to system repair = 1.0367 Hours 0.43197 E-01 days.

Rank	Basic event description	Importance	Failure rate per year	Mean fault duration (hr)
1	I-V-D2 Noise on line to control valve transmitter	0.325	1.000	1.000
2	I-V-C1 PG&E power failure	0.163	5.00	1.000
3	I-V-C1 High resistance WLT #1 transducer	0.130	0.400	1.000
4	I-V-D2 Valve module contacts open	0.432 E-01	0.133	1.000
4	I-V-C1 Tank level module voltage high	0.432 E-01	0.133	1.000
4	I-V-D2 TCW S-tank level rec card voltage high	0.432 E-01	0.133	1.000
5	I-V-C1 Level transmitter fails low	0.218 E-01	0.670 E-01	1.000
5	I-V-D2 TCW storage tank level receiver high	0.218 E-01	0.670 E-01	1.000
5	I-V-C2 2400-Hz receiver fails low	0.218 E-01	0.670 E-01	1.000
5	I-V-C1 Open circuit relay CR1	0.218 E-01	0.670 E-01	1.000
5	I-V-C1 Residual magnetism relay CR1	0.218 E-01	0.670 E-01	1.000
5	I-V-D2 Relay coil CR7 open circuit	0.218 E-01	0.670 E-01	1.000
5	I-V-C2 Agastat TDR-4 contact transfer open	0.218 E-01	0.670 E-01	1.000
5	I-V-D2 Flow valve selector switch opens	0.218 E-01	0.670 E-01	1.000
5	I-V-C2 Valve selector switch contacts open	0.218 E-01	0.670 E-01	1.000
5	I-V-C2 Valve stem failure	0.218 E-01	0.670 E-01	1.000
5	I-V-D2 Valve transmitter fails low	0.218 E-01	0.670 E-01	1.000
6	I-V-D1 Close all valve transmitter failure on	0.921 E-02	1.000	1.000
7	I-V-C1 Storage tank(s) valved out	0.632 E-03	0.670 E-01	1.000
8	I-P-C1 Standpipe #2 valved out	0.617 E-03	0.670 E-01	1.000
8	I-V-D1 CR5-3 contacts close	0.617 E-03	0.670 E-01	1.000
8	I-V-D1 CR2A-1 contacts close	0.617 E-03	0.670 E-01	1.000
9	I-P-D1 Noise on line from standpipe to Bldg. 511	0.958 E-04	1.000	1.000

failure of control devices on the tank level feedback loop which would go undetected in Bldg. 511.

Table 17 ranks the enabling events. We see that failure of components in the backup power supply system, i.e., the inverter, battery, and battery charger are dominant enabling events. The next most important enabling event is failure of the operator in Bldg. 511 to respond to a low-level tank alarm. We assign a probability of 0.01 for this event, which is consistent with data given by Swain and Guttman.[15] Table 17 also ranks the most important min-cut sets. These min-cut sets include the important initiating and enabling events described above.

Table 17. Ranking of enabling events.

Insufficient level in storage tank and no detection Enabler (sequential contributory) basic event importance (measure of interval reliability)				
Rank	Basic event description	Importance	Failure rate per year	Mean fault duration (yr)
1	Inverter failure storage tank	0.564 E-01	0.267	0.130
1	Battery failure at storage tank	0.564 E-01	0.267	0.130
1	Battery charger failure storage tank	0.564 E-01	0.267	0.130
2	No operator response to low storage tank level	0.433 E-02	—	0.100 E-01
3	Relay coil CR6-1 open circuit	0.377 E-02	0.670 E-01	0.130
3	Storage alarm module inactive	0.377 E-02	0.670 E-01	0.130
4	No operator response to low standpipe level	0.557 E-03	—	0.100 E-01
5	Red light indicator low storage-tank burned out	0.522 E-03	0.267	0.130
5	Tank low-level alarm inactive	0.522 E-03	0.267	0.130
6	TDR1A-1 contacts fail to close	0.490 E-04	1.000	0.130
6	TDR3A-1 contacts fail to close	0.490 E-04	1.000	0.130
7	Red light indicating low standpipe level burned	0.170 E-04	0.267	0.130
7	Standpipe low-level alarm inactive	0.170 E-04	0.670 E-01	0.130
8	Tank selector switch in the wrong position	0.149 E-04	6.00	1.000 hr
9	No operator response to high tank level	0.120 E-04	—	0.100 E-01
10	905-Hz OT-30 transmitter inactive	0.328 E-05	0.670 E-01	0.130
10	FR3-2 contacts fail to close	0.328 E-05	0.670 E-01	0.130
10	1325 OT-30 transmitter failure	0.328 E-05	0.670 E-01	0.130
10	FR3-2 contacts fail to close	0.328 E-05	0.670 E-01	0.130
11	Red light indicating high tank level burned out	0.368 E-06	0.267	0.130
11	Tank high level alarm inactive	0.368 E-06	0.670 E-01	0.130
12	PCW #1 light burned out	0.114 E-06	0.267	0.130
12	PCW #3 light burned out	0.114 E-06	0.267	0.130
12	PCW #3 alarm failure (off)	0.114 E-06	0.670 E-01	0.130
12	PCW #1 alarm failure	0.114 E-06	0.670 E-01	0.130

Acknowledgments

The authors thank and appreciate the contributions of Dr. Arnold A. Weintraub for his support and encouragement throughout the execution of this project. His criticism and direction were instrumental in guiding our research to positive progress.

References

1. H. K. Hasegawa, N. J. Alvares, A. E. Lipska-Quinn, D. G. Beason, S. J. Priante, and K. L. Foote, *Fire Protection Research for Energy Technology Projects: FY 82 Year-End Report*, Lawrence Livermore National Laboratory, Livermore, California, UCRL-53179-82 (1983).
2. H. K. Hasegawa, N. J. Alvares, A. E. Lipska-Quinn, D. G. Beason. K. L. Foote, and S. J. Priante, *Fire Protection Research for Energy Technology Projects: FY 81 Year-End Report*, Lawrence Livermore National Laboratory, Livermore, California, UCRL-53179-81 (1982).
3. H. K. Hasegawa, N. J. Alvares, A. E. Lipska, H. W. Ford, S. Priante, and D. G. Beason, *Fire Protection Research for Energy Technology Projects: FY 80 Year-End Report*. Lawrence Livermore National Laboratory, Livermore, California, UCRL-53179 (1981).
4. H. K. Hasegawa, N. J. Alvares, A. E. Lipska, H. W. Ford, and D. G. Beason, *Fire Protection Research for Energy Technology Projects: FY 79 Year-End Report*, Lawrence Livermore National Laboratory, Livermore, California, UCID-18902 (1981).
5. N. J. Alvares, K. L. Foote, and P. J. Pagni, *Forced-Ventilated Enclosure Fires*, Lawrence Livermore National Laboratory, Livermore, California, UCRL-89615 (1984).
6. J. R. Lawson and W. J. Parker, *Development of an Ease-of-Ignition Test Using a Flame Exposure*, National Bureau of Standards, Washington, D.C., NBSIR 82-2503 (June, 1982).
7. J. C. Siegle, L. T. Muus, T. Lin, and H. A. Larsen, "The Molecular Structure of Perfluorocarbon Polymers II: Pyrolysis of Poly (tetrafluoroethylene)," *J. Polym. Sci.* **A2**:391 (1964).
8. H. H. G. Jellinek and H. Kachi, "Thermal Degradation of Poly (tetrafluoroethylene) in a Closed System," *Makromol. Chem.* **85**:1 (1965).
9. L. A. Errede, "The Application of Simple Equations for Calculating Bond Dissociation Energies to Thermal Degradation of Fluorocarbons," *J. of Org. Chem.* **27**:3425 (1962).
10. A. J. Lovinger and D. J. Freed, "Inhomogeneous Thermal Degradation of Poly (vinylidene fluoride) Crystallized from Melt," *Macromolecules* **13**:3425 (1980).
11. H. E. Lambert, *The Digraph-Fault Tree Methodology and Its Use in Transportation Risk Analysis*, Tera Corporation, Berkeley, California.
12. C. Dunglinson and H. E. Lambert, "Interval Reliability for Initiating and Enabling Events," *IEEE Transactions on Reliability*, **R-32**, 2 (1983).
13. H. E. Lambert, J. J. Lim, and F. N. G. Filman, *A Digraph-Fault Tree Methodology for the Assessment of Material Control Systems*, Lawrence Livermore National Laboratory, Livermore, California, UCRL-52170 (1979).
14. H. E. Lambert, *IMPORTANCE: The IMPORTANCE Computer Code*, Lawrence Livermore National Laboratory, Livermore, California, UCRL-79269 (1977).
15. Swain and Guttman, *Handbook of Human Reliability Analysis with Emphasis on Nuclear Power Plant Applications*, Nuclear Regulatory Commission, Washington, D.C., NUREG-1278 (1983).

Appendix A
Forced-Ventilation Enclosure Fires

Abstract

Twenty-seven forced ventilation fire experiments were conducted in the LLNL fire test cell. A wide variety of fuels, ventilation rates and fire strengths were included. Experimental results revealed that "quasi-steady-state" was not reached until approximately 2000 sec after ignition. It was found that 80% ± 5% of the heat produced by the fire was deposited in the enclosure walls. Twice the stoichiometric ventilation was required to insure complete combustion of the provided fuel. Selected data was compared with predictions from several computer models and the attributes and diffculties of each are discussed.

Introduction

The compartment fire experiments described here were conducted in the Lawrence Livermore National Laboratory Fire Test Cell to assess the behavior of fire and fire products where enclosure ventilation is provided by an air-extraction system (Alvares, *et al.*, 1981 and 1982). Such systems are standard in modern laboratory and power-generating facilities (Cleary, W. M., 1979). The 27 tests described here are part of an ongoing series of experimental fires begun in July 1981. The fires, located on the floor on the center line of the test cell, were either naturally burning pool fires or analogue pool fires where the fuel (either gas or liquid) was metered into a burner or pan. The purpose of the analogue pool fires was to control the fire strength and thereby to assess interaction between fire strength and ventilation rate. Designed experimental conditions ran the gamut from fully ventilated to severely ventilation-limited fires.

Two requirements motivated these experiments: (1) to develop insight and experience with characteristics of fires in extraction-ventilated enclosures, and (2) to produce quantitative data to evaluate current mathematical models modified to fit the extraction-ventilation mode. It is intended to use validated portions of the tested models as the initial component of a procedure to predict fire risk in large research and fabrication enclosures.

Instrumentation

Figure A-1 is an artistic conception of enclosure geometry and Fig. A-2 is a detail of the extraction ventilation system. Clean air is introduced along the floor of the test cell, and combustion products are pulled out near the top of the cell by an axial fan. Extraction rate is controlled by a butterfly valve upstream of the fan. Exit gas flowrate from the test cell is measured by a sharp-edge orifice, and inlet flow rate is measured using a calibrated vane anemometer. Table A-1 gives some pertinent properties of the enclosure.

Table A-2 lists experiments conducted during the FY 1982 test series. The first five columns describe the tests done: fuel, type of fire, heat release rate, and initial forced ventilation rate in the exit duct. "Fire type" refers to the method of fuel control and fuel phase.

In the tests designated "gas," bottled methane metered by critical orifice and in-line turbine meter was conveyed to a 0.28-m-diam rock-filled pan on the floor of the test cell. Gas entering the pan at the bottom becomes distributed uniformly through the rock bed as it flows to the rock bed surface. This burner was intended to be a pool fire analog. Unfortunately, the burner diameter was too small and at high fire strengths (i.e., high fuel-flow rates) the burner flame took on characteristics of a momentum jet rather than the intended bouyant plume. This complicated analyses of these methane-fueled fires.

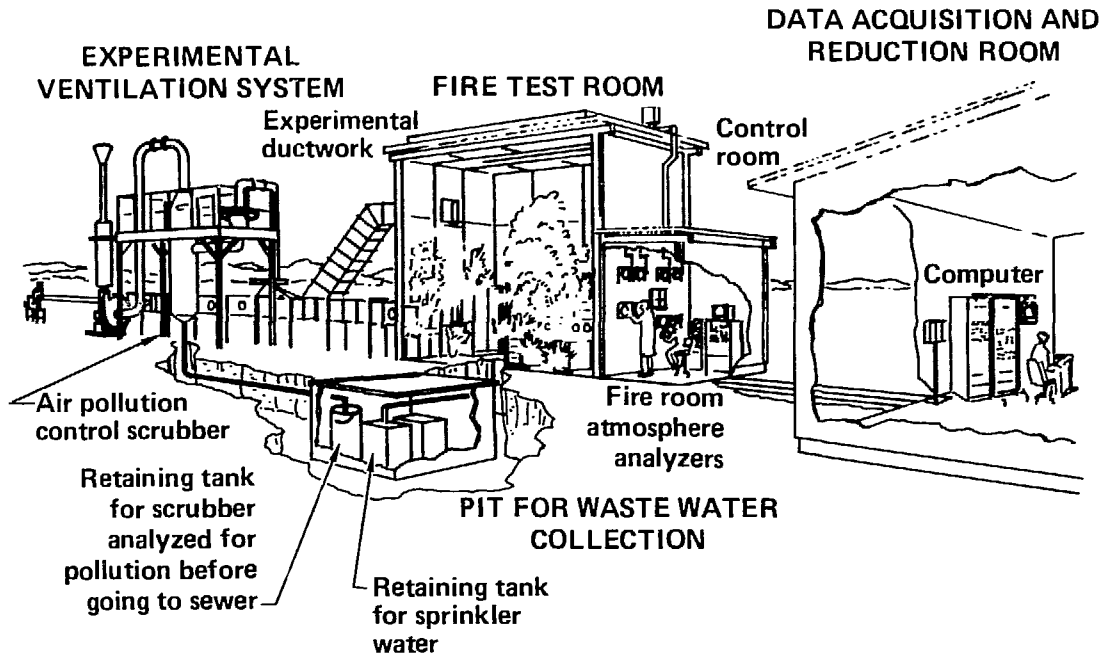

Figure A-1. Artist's conception of LLNL test cell geometry.

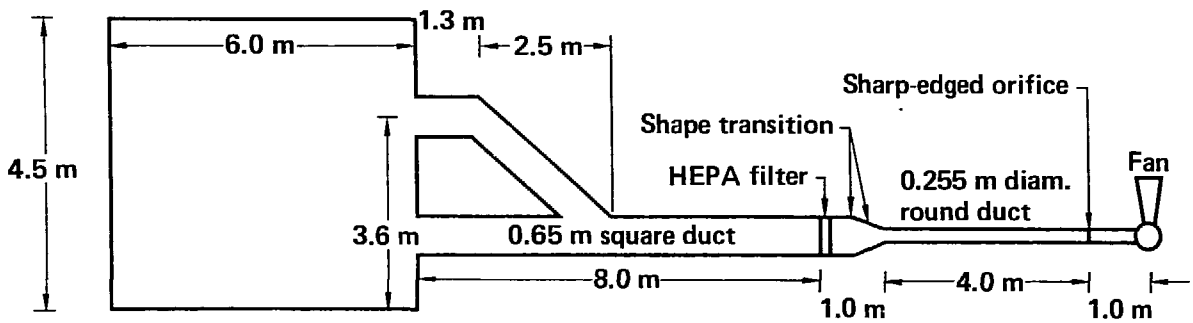

Figure A-2. Detail of LLNL extraction ventilation system.

Table A-1. 1982 LLNL test-cell geometry information.

1. The burn room was 4.5 m high, 4.0 m wide, and 6.0 m long.
2. The exit opening (65 cm × 65 cm) was on the vertical centerline of the west wall (4.0 m wide × 4.5 m high), with its center 3.6 m above the floor.
3. The inlet opening consisted of four horizontal rectangles (0.5 m long × 0.12 m high) with horizontal centerlines 0.1 m above the floor.
4. For radiation calculations, the walls can be assumed to be completely black.
5. The walls, floor and ceiling consist of a 10-cm thick Al_2O_3-S_1O_2 refractory with the following estimated properties:

	Walls	Ceiling
ρ (kg/m^3)	1440	1920
k (W/m°k)	0.39	0.63
c (J/kg°k)	1000	1000

Table A-2. 1982 Fire model test data.

Test	Q kW	V̇ l/s	Fuel formula	Fire type	Steckler layer height (m)	Exit gas temp °C	Zone 6 wall temp °C	% Heat loss to walls	O_2 consumed (g/s)	CO_2 (g/s)	CO (g/s)	CH_4 (g/s)
MOD3	60	100	CH_4	Burner	1.53	100	80	–	4.5	4.2	–	–
MOD2	55	500	CH_4	Burner	1.77	90	65	67	5.0	4.9	–	–
MOD10	100	100	C_3H_8O	Spray	1.27	100	80	87	2.4	5.8	–	–
MOD11	100	500	C_3H_8O	Spray	1.65	90	60	62	6.1	9.8	–	–
MOD11A	100	500	C_3H_8O	Spray	1.48	100	80	64	3.0	8.7	–	–
MOD1	135	250	CH_4	Burner	1.45[a]	130	90	84	8.7[a]	8.7	–	–
MOD7	135	250	CH_4	Burner	1.24	140	105	82	9.3	9.6	–	–
MOD24	200	110	C_8H_{18}	Spray	1.05	150	145[b]	83	10.3	10.5	0.3	0.07
MOD25	200	90	C_3H_8O	Spray	1.24	160	160[b]	86	14.2	12.5	1.7	0.03
MOD4	230	100	CH_4	Burner	1.36[a]	170	150	95	13.8	10.7	1.3	0.3
MOD23	400	130	C_8H_{18}	Spray	1.12	180	150	83	15.9	13.1	–	0.66
MOD26	400	100	C_3H_8O	Spray	1.11	180	180[b]	–	17.8	14.7	5.3	0.37
MOD6	460	100	CH_4	Burner	1.39[a]	200	180	–	12.4[a]	9.9	1.5	0.58
MOD6A	470	100	CH_4	Burner	1.39[a]	190	170	–	13.7[a]	10.8	2.2	0.61
MOD27	400	250	C_3H_8O	Spray	1.10	220	220[b]	95	23.6	21.4	2.9	0.02
MOD27A	400	250	C_3H_8O	Spray	1.02	210	200[b]	91	20.7	23.3	–	0.14
MOD27B	400	250	C_3H_8O	Spray	1.03	205	185[b]	89	24.9	26.4	–	0.11
MOD8	400	500	C_3H_8O	Spray	1.24	200	160	83	29.0	30.3	–	–
MOD13	400	500	C_3H_8O	Spray	1.12	230	180	79	20.9	31.5	–	–
MOD14	400	500	C_8H_{18}	Spray	1.04	200	150	79	12.4[c]	27.1[c]	–[c]	0.04
MOD14A	400	500	C_8H_{18}	Spray	0.90	200	150	68	13.9[c]	23.4[c]	–[c]	0.04
MOD5	455	500	CH_4	Burner	1.44[a]	280	210	83	36.0	32.6	–	0.04
MOD9	800	500	C_3H_8O	Spray	1.10	280	225	88	55.2	50.5	13.2	2.0
MOD9A	800	500	C_3H_8O	Spray	1.47	280	220	87	44.8	46.9	4.3	1.9
MOD15	800	500	C_8H_{18}	Spray	1.11	255	200	82	17.0[c]	29.4[c]	–[c]	1.7
MOD12	800	100	C_3H_8O	Spray	–[a]	–	–	–	–	–	–	–
MOD16	800	100	C_8H_{18}	Spray	–[a]	–	–	–	–	–	–	–
MOD17	600	500	C_3H_8O	Pool	1.08	250	195	63	5.6[c]	6.8[c]	2.2[c]	–
MOD18	400	100	C_3H_8O	Pool	1.12	160	150	83	9.3[c]	7.6[c]	4.3[c]	–
MOD19	1100	500	C_8H_{18}	Pool	1.09	255	200	–	36.3	29.0	9.9	–

[a] Equilibrium not reached.
[b] Test run after polystyrene.
[c] Leak in gas analysis line.

rotometer to an opposed jet nozzle located in the center of a 0.91-m-diam steel pan with a 15-cm lip on the floor of the test cell. Liquid from the nozzle is sprayed on a plane normal to the orifice axes with a uniform radial distribution. Ignition is by a remotely energized electric arc. The atomized spray quickly evaporates and burns before it contacts pan surfaces; and the resulting fire has every appearance of a natural pool fire. Figure A-3, plates "a" through "d," show photographs of the opposed jet nozzle, the pan with jet installed, the opposed jet nozzle spray pattern, and the resulting fire.

For tests designated as "pool," approximately 40 liters of liquid fuel were placed in the 0.91-m steel pan. The intial fuel level came to 7 cm from the top of the 15-cm-high wall. The effects of the pan walls on the fuel-burning rate become asymptotic for lip heights greater than 7 cm for this size pool (i.e., $1/d \geq 0.08$), (Orloff, 1981). The mass pyrolysis rate was determined using a calibrated load cell.

Instrumentation of the enclosure and ventilation circuits was extensive and consisted of gas and surface thermocouples, calorimeters, radiometers, combustion gas and oxygen detectors, fuel and ventilation-flow sensors, and a video camera for recording the fire shape. Data were recorded and reduced on a PDP-11 computer. Table A-3 summarizes sensor and instrumentation parameters. Previous work (Alvares, *et al.*, 1982) indicate that the majority of energy produced by fire (up to 80%) is absorbed by the enclosure surfaces. To confirm this finding and assess the distribution of the surface energy deposition, 23 thermocouples were installed on test cell surfaces in the array displayed in Fig. A-4. These thermocouples were simply pressed onto the Kastolite surface and held there with spring tension. This distribution was designed assuming a symmetrical energy source field.

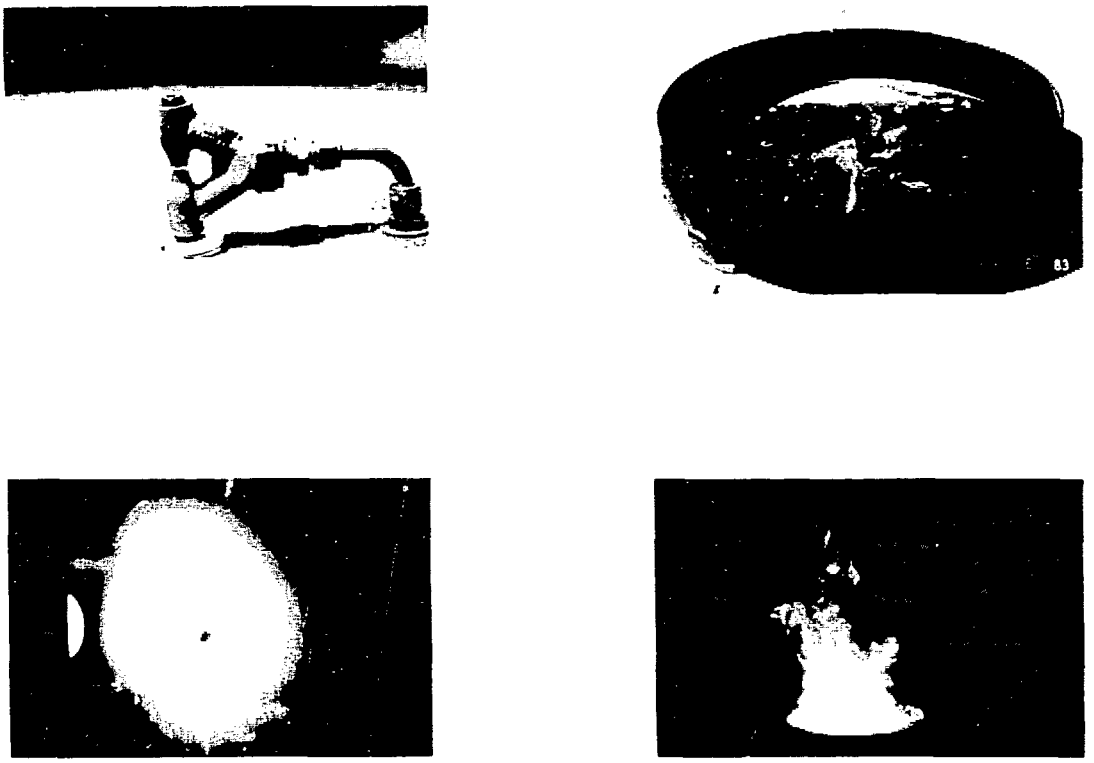

Figure A-3. Photographs of spray injection system.

For fires designated "spray," liquid fuel from a pressurized reservoir flows through a calibrated The standard experimental procedure depended on the fuel involved. Essentially, ventilation and fuel flow rates were initially fixed, and pre-calibration of gas analyzers was done before the test cell was secured for the test. Then, five minutes of pre-ignition operation was allowed to insure stable instrument operation and to provide initial data values. Fuel flow and spark ignition were simultaneously initiated and data were recorded until quasi-steady-state conditions were reached.

Experimental Results

Figures A-5(a)–(d) are examples of data produced. MOD 27B was an isopropanol spray fire with the fire strength set to 400 kW and the ventilation rate maintained at 250 L/s. Figure A-5(a) contains typical gas and wall temperatures within the enclosure. Figures A-5(b)–(d) show the consumption and production of combustion gases. (Note the relativley low temperatures, <300°C.) Figure A-5(c) shows the inlet and outlet air flows.

One feature common to all tests is the appearance of a reversal inlet air flow spike, whereupon fire initiation the inlet flow is reduced, and sometimes, as in the case of Mod 27B, flow is reversed. The magnitude of this negative peak varies directly with fire strength. It is caused by the need to reduce the mass in the test cell to keep a constant energy per unit volume in the approximately constant pressure test cell. Also, at early times, the wall temperature may rise faster than the gas air temperature, indicating that initially direct thermal radiation heat transfer from the fire to the walls is important.

The exit air flow was adjusted to compensate for reduced flow because of wetting and plugging of a particulate filter located between the test cell and the extraction fan. All tests where the fire strength was greater than 400 kW had this problem, even though new filters were installed prior to each test.

Table A-3. Instrumentation for 1982 fire model test series.

Parameter	Instrument	Characteristics	Range	Accuracy	Stability
Ceiling and wall temperature	Exposed-bead thermocouples	Chrome-Alumel Junction, American wire gauge 22 0.6 + 0.01 mm bead	−18 to 1200°C	± 1°C	
Compartment gas temp. (horizontal array at 2.1 and 3.7 m elevation)	Shielded-bead thermocouples	Same as above	−18 to 1200°C	± 1°C	
Compartment gas temp. (vertical rake)	Exposed beads shielded from plume radiation by aluminum screen	Chrome-Alumel Junction, American wire gauge 36	−18 to 1200°C	± 1°C	
Pressure	*One pitot tube at 2.1 and 3.7 m elevations*				
Wall pressure just upstream of HEPA filter	Validyne transducers, Model P24		0.01 to 3000 psi	0.05 psi	± 0.1 psi for DC power changes between 22 and 35 V
Volumetric exhaust flux	Wall pressure differential across orifice 15.2 m downstream of exhaust inlet and downstream of HEPA filter		0.01 to 3000 psi	0.05 psi	Same as above
Intake air velocity	R. M. Young vane anemometer	Lower threshold 0.2 m/s	1 to 50 m/s linear range		
O_2 volume concentration	Beckman Model 402	Exhaust sample 3/m downstream duct inlet, 10% full-scale response in 1 s	0 to 25%	1 to 5% ppm in clean air	Recalibrated after each test
	Beckman Model OM-11	90% full-scale response in 80 s	0 to 100%	± 5% of measured value	Recalibrated after each test
CO_2 volume concentration	Beckman Model 864, exhaust air sample	90% full-scale response in 0.5 s	0 to 100%	± 5% of measurement	Recalibrated after each test
CO volume concentration	Beckman Model 864				
CH_4 volume concentration	Beckman Model 402 exhaust air sample	90% full-scale response in 1 s	0 to 25%	± 1% of measurement	± 1% of full scale
Liquid fuel flow	Fisher-Porter flow rater FP-1/2-27/-6-10/58	Calibrated at constant pressure metering volume change of decanted fuel	0 to 2000 ml/min	± 2% of measured value at ambient conditions	0.5% of full scale
Gas (CH_4) fuel flow	Brooks full view rotameter Model 1100-08 H2 G1B	No gas pressure and temperature information	0 to 200 ml/min	1% of measured value at ambient conditions	0.5% of full scale
Total and radioactive heat flux	Hy-Cal calorimeter and radiometer	Placed in hot layer outside fire plume	0 to 300 BTU/ft^2 s	3% of measurement	5% of full scale

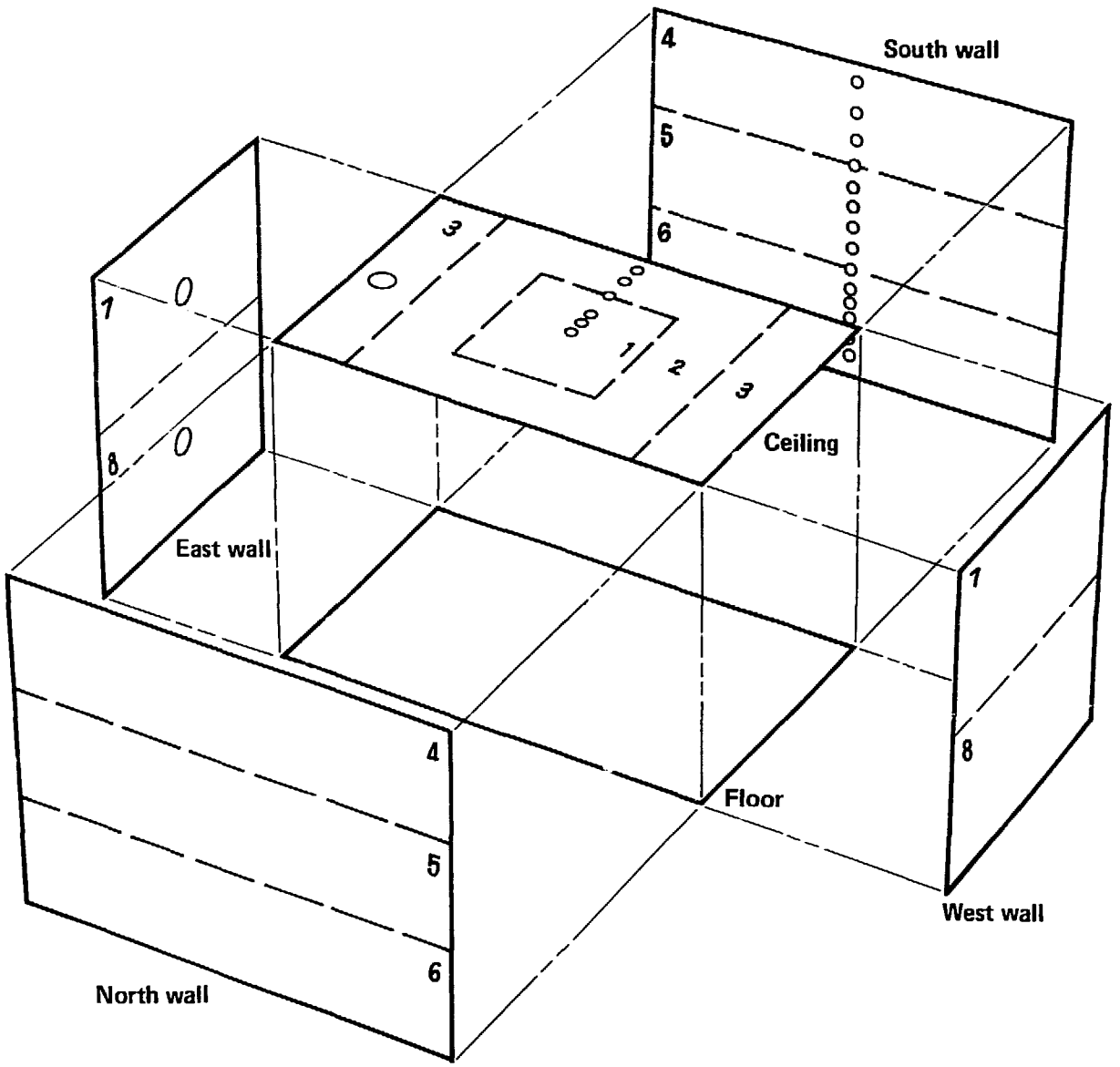

Figure A-4. Detail of wall thermocouple placement and wall zone areas used for Duhamel analysis.

MOD 27B is an example of an underventilated fire, where CO is produced and CH_4 is found in test cell exhaust, Fig. A-5(d). To identify when to expect ventilation-controlled conditions, stoichiometric conditions were precalculated for each fire strength and ventilation. In Fig. A-6, the solid line is the stoichiometric line for methane, which needs the most oxygen per gram of fuel. Fires below this line were expected to be under-ventilated and fires above this line fully ventilated. This, however, was not the case. For these forced-ventilation tests, the inlet ventilation needed to be twice that of stoichiometry (the dashed line), or incomplete combustion occurred, as MOD 27B shows. This suggests that air entrained by the fire does not completely react with fuel gases in the reaction plume, and that some of the entrained oxygen survives the fire to be pumped into the upper layer intact. This is confirmed by oxygen sensors in the upper layer and exit duct.

Figures A-7(a) and A-7(b) contrast an over-ventilated fire with an under-ventilated fire. (Mod 8; 400 kW at 500 L/s and Mod 12; 800 kW at 100 l/s). Mod 12 was terminated at approximately 300 s for safety

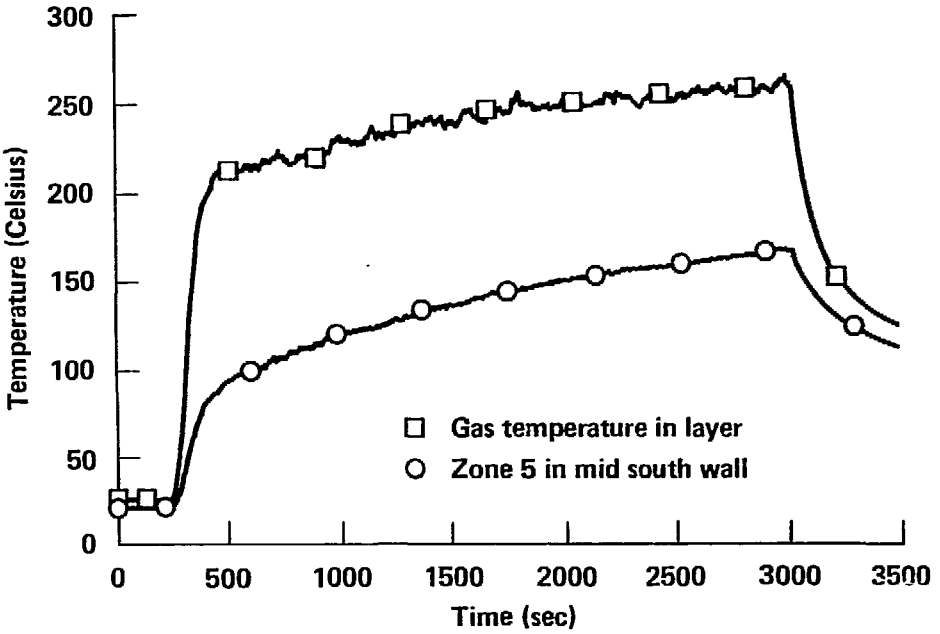

Figure A-5(a). Example temperature history for MCD 27B.

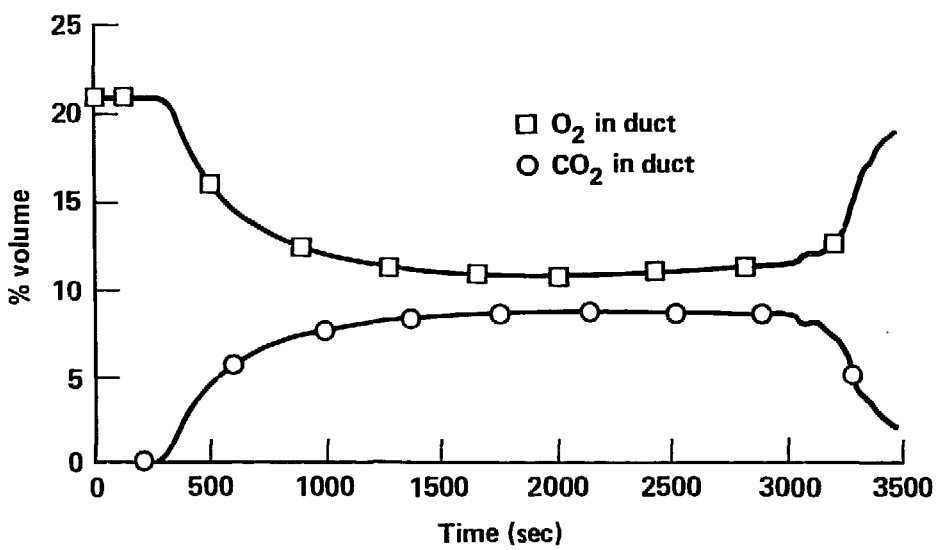

Figure A-5(b). Example major gas (O_2 and CO_2 history) for MOD 27B.

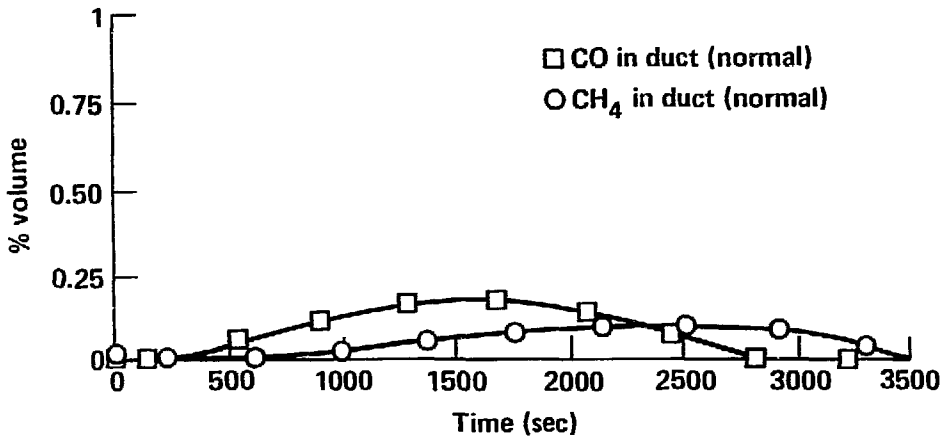

Figure A-5(c). Example minor gas (CO and CH_4 history) for MOD 27B.

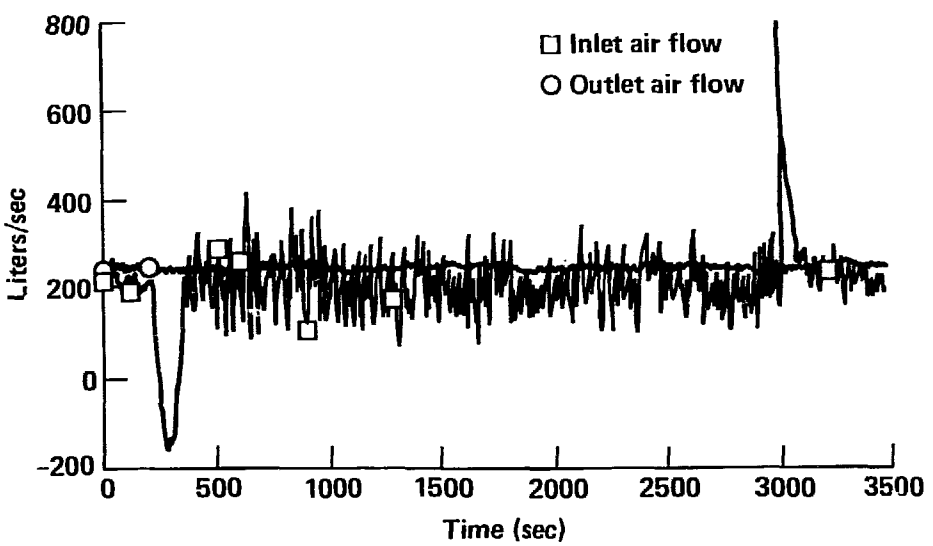

Figure A-5(d). Example airflow history for MOD 27B.

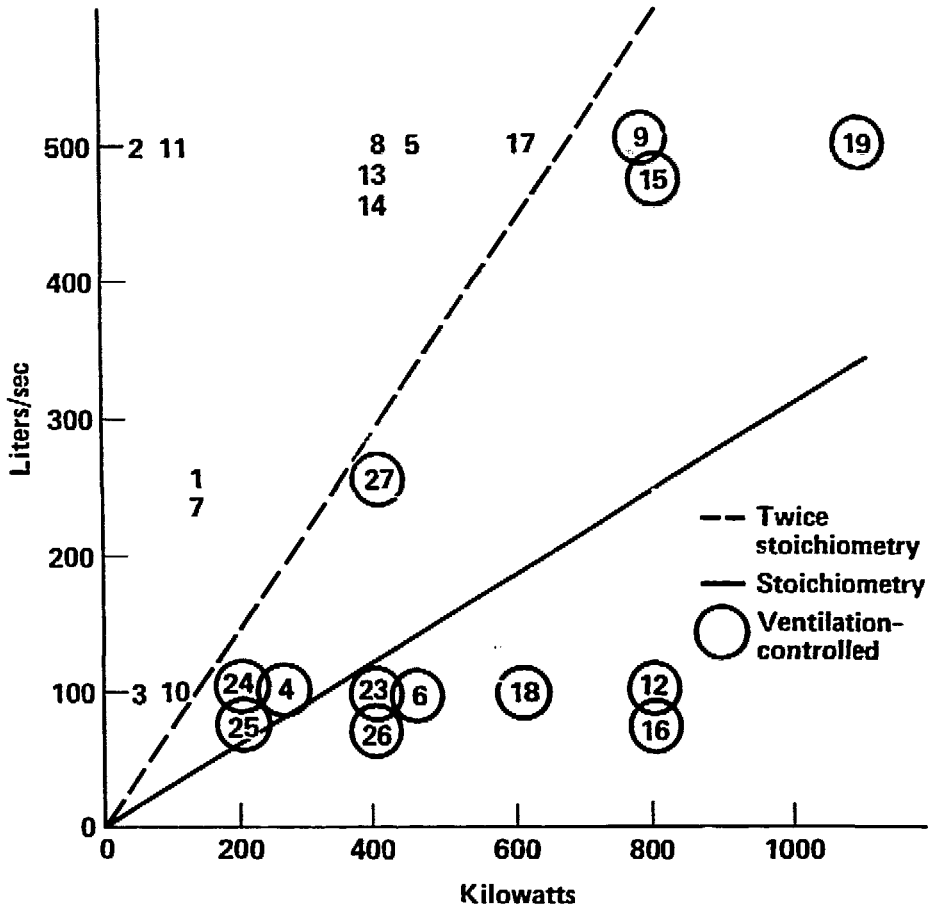

Figure A-6. Conditions of fire relative to stoichiometric fuel/air ratio.

reasons. All tests were terminated if total hydrocarbon level exceeded 10 000 ppm, the lower ignition limit of methane, to avoid the potential danger of accidental deflagration. Note the rapid rise of CO and CH_4 in Fig. A-7(b) for Mod 12. These signals illustrate extreme ventilation-limited conditions. In comparison, Mod 8 exhibits relatively well-behaved data; e.g., very low production of CO and CH_4.

Figures A-8(a) and A-8(b) shows data from two fires with different fuels at the same initial ventilation rate and fire strength. MOD 26 is an isopropanol (C_3H_8O) spray fire and MOD 23 is an isooctane (C_8H_{18}) spray fire. These two very different fuels give remarkably similar results for most measurements. Table A-3 contains tabular data for the other tests done during the 1982 series.

Figure A-9(a) shows temperature profiles of rake thermocouples at various times for Mod 27B. Two vertical columns (rakes) of thermocouples were positioned symmetrically east and west of the burn pan. Each rake contained 15 5-mil chrome-alumel thermocouples at 30-cm vertical intervals. The shape of the cell thermal profile or "upper layer" is quickly established (within 250 s) and remains essentially unchanged throughout the fire. For MOD 27B this upper layer temperature is 200°C, and rises to only 250°C at long times. One characteristic of these tests is that the temperature interface between the hot and cold layers is not well defined. It is more of a temperature gradient that asymptotically approaches infinity in the upper layer. In Fig. A-9(a), the history of the temperature profile to 1500 s shows this well. (Note that from here on all time references are from the start of the fire.) To make model evaluation easier, Steckler's two-layer equivalency technique (Alvares, *et al.*, 1982) was applied to these temperature profiles. This technique simplifies profile data into the two distinct layers used by most zone models. The results of this procedure are shown in Fig. A-9(b) for test MOD 27B at 1500 s. Table A-4 summarizes these calculated Steckler two-layer data for all tests in this series.

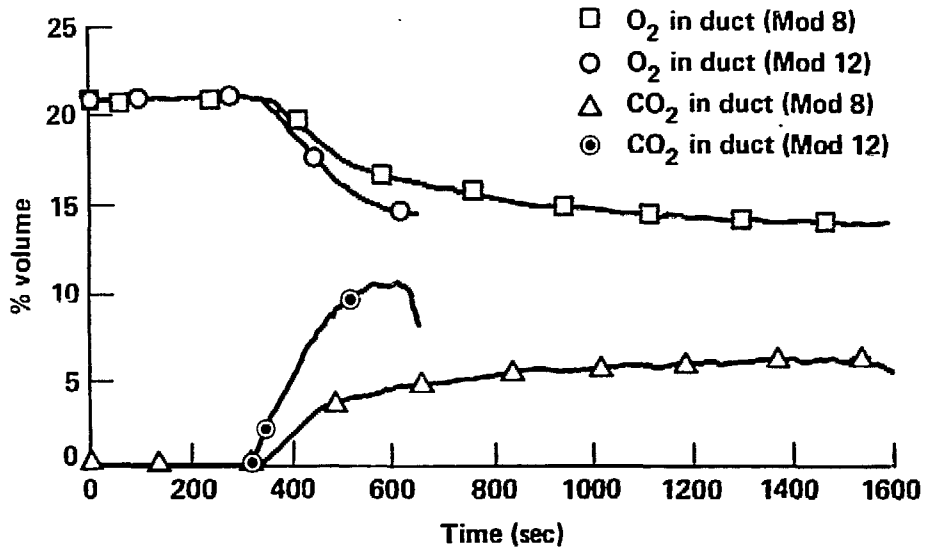

Figure A-7(a). Comparison of major gas (O_2 and CO_2) histories for MOD 8, an overventilated fire, and MOD 12, an underventilated fire.

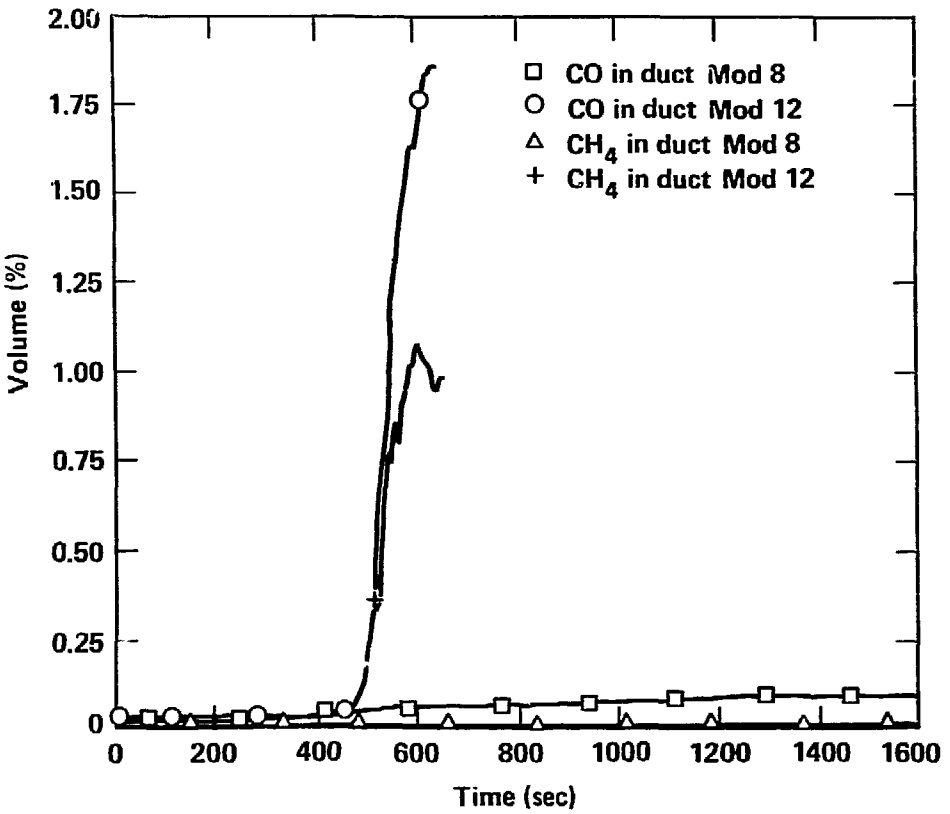

Figure A-7(b). Comparison of minor gas (CO and CH_4) histories for MOD 8, an overventilated fire, and MOD 12, an underventilated fire.

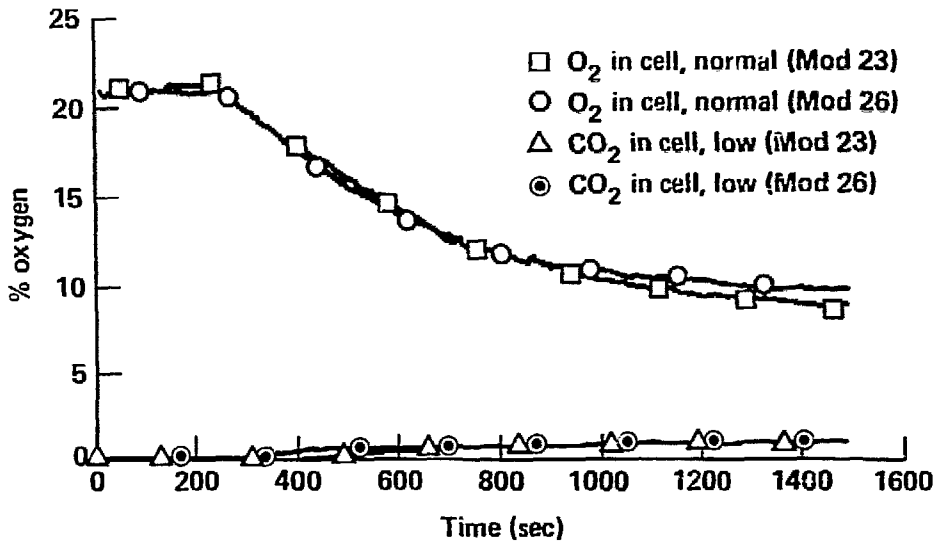

Figure A-8(a). Comparison of major gas (O_2 and CO_2) histories for similar isopropanol and isooctane fires.

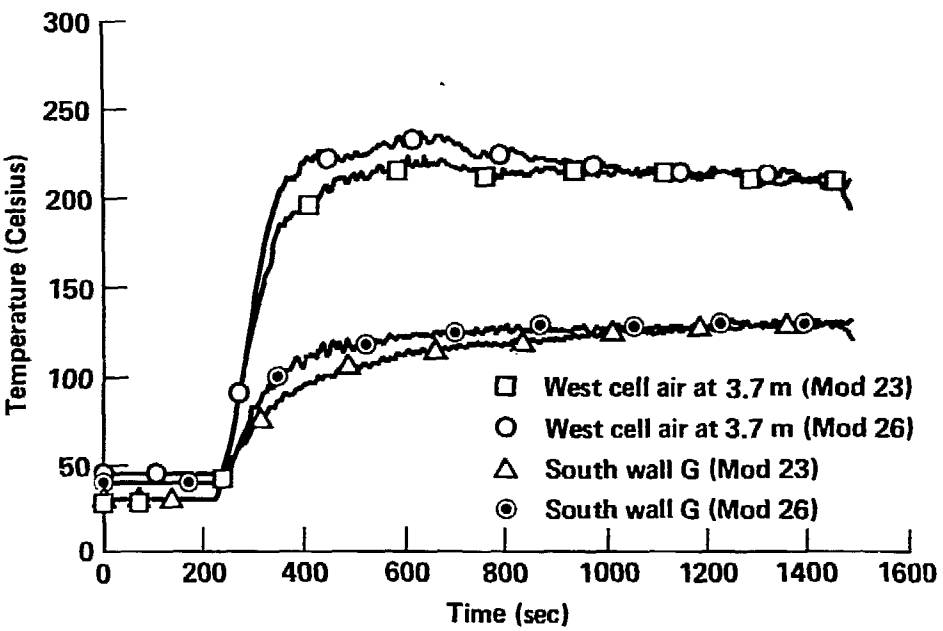

Figure A-8(b). Comparison of temperature histories for similar isopropanol and isooctane fires.

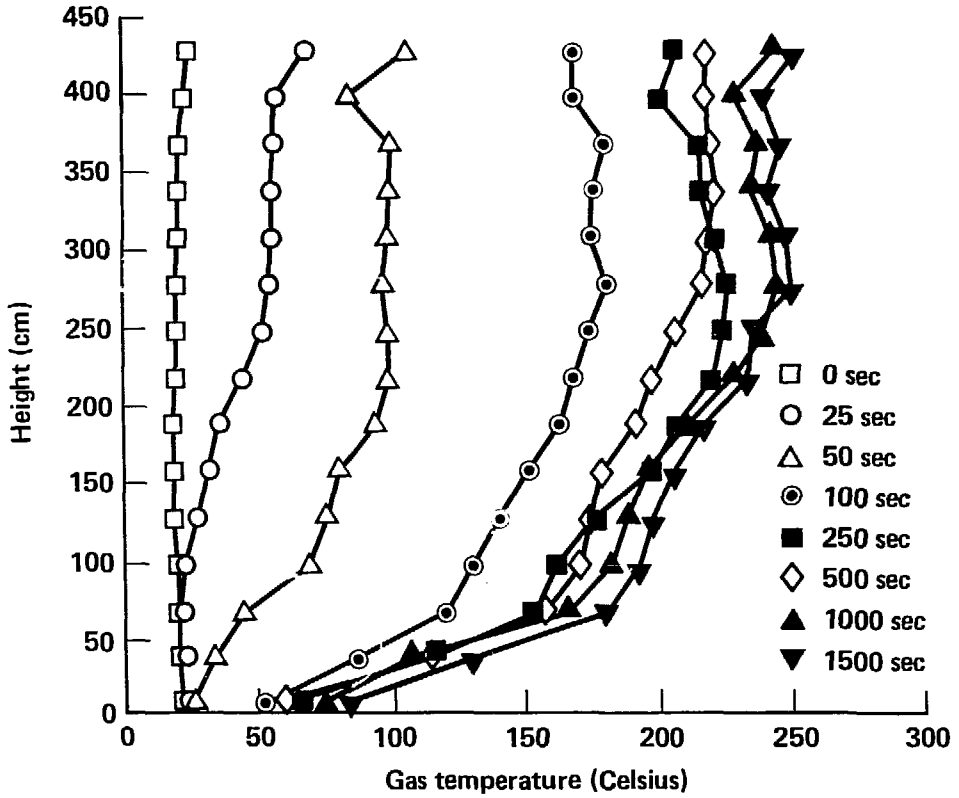

Figure A-9(a). Actual room gas temperature profiles for MOD 27B at early times.

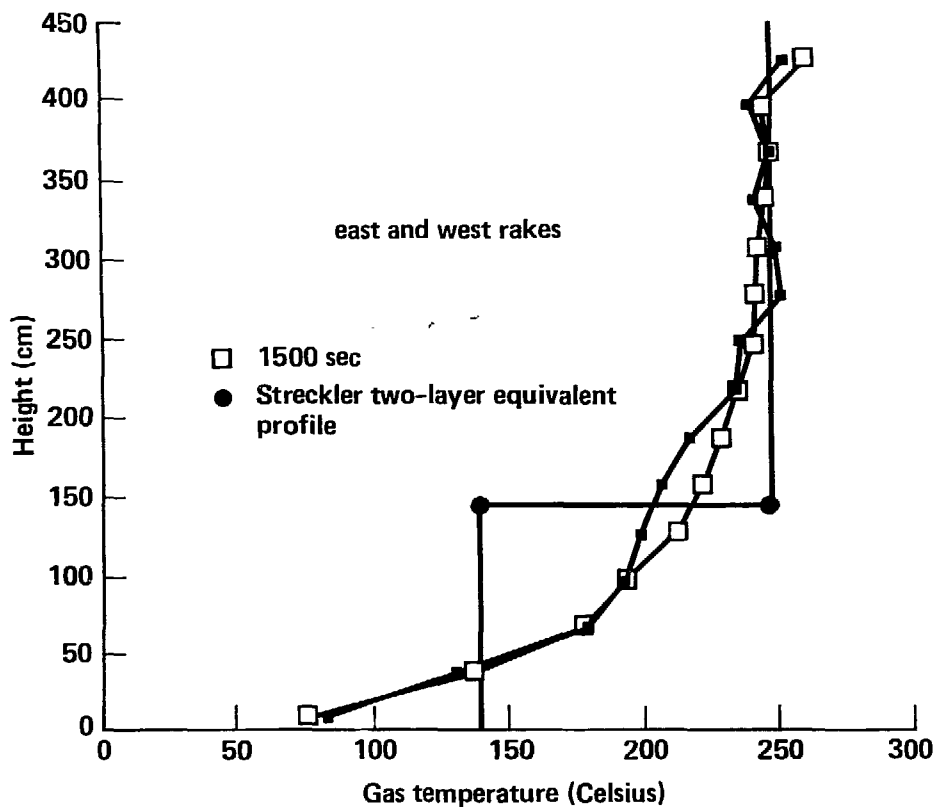

Figure A-9(b). Actual room gas temperature profile and Steckler two-layer equivalent profile for MOD 27B at 1500 s.

Table A-4. Steckler two-layer temperatures.

Test	Time (sec)	Lower layer temp (°C)	Upper layer temp(°C)	Height of layer interface (m)
MOD 1	900	59	134	1.58
MOD 2	1700	48	87	1.77
MOD 3	2200	59	107	1.53
MOD 4	1700	84	198	1.39
MOD 5	1700	111	294	1.51
MOD 6	400	105	253	1.54
MOD 6A	500	99	232	1.52
MOD 7	1700	70	156	1.52
MOD 8	1200	116	237	1.41
MOD 9	600	142	297	1.17
MOD 9A	800	147	292	1.22
MOD 10	1500	75	118	1.50
MOD 11	1200	54	91	1.65
MOD 11A	1200	58	103	1.48
MOD 12	300	128	240	1.26
MOD 13	1200	129	245	1.49
MOD 14	1300	122	214	1.15
MOD 14A	1200	119	213	1.22
MOD 15	800	155	272	1.15
MOD 16	300	135	215	1.15
MOD 17	1500	118	262	1.21
MOD 18	2300	107	202	1.35
MOD 19	1300	154	284	1.26
MOD 20	1700	63	98	1.45
MOD 23	1200	123	200	1.26
MOD 24	3300	114	189	1.25
MOD 25	2800	107	191	1.14
MOD 26	1300	113	202	1.08
MOD 27	1200	142	258	1.28
MOD 27	2200	148	258	1.20
MOD 27A	1500	124	242	1.20
MOD 27A	2300	119	229	1.15
MOD 27B	2700	133	256	1.10

To validate the accuracy of the instrumentation, stringent-mass, energy, and species-balancing criteria were applied to all raw data (Alvares, *et al.*, 1982). Mass flows in and out were corrected for temperature and density changes and checked to balance. Gas species are similarly checked to insure elemental balances. Measured fire strengths were compared against calculated fire strengths from CO_2 and CO production and O_2 consumption. This procedure provides a good measure of the data quality and identified when the quasi-steady-state was reached. The definition of quasi-steady-state is taken as the establishment of conditions where oxygen consumption and combustion gas formation becomes constant and species balancing occurs. For these tests, this occurs approximately 2000 s after the start of the fire and is highly dependent on the ventilation rate. The long time necessary to reach quasi-steady-state conditions is due to the large volume of the test cell. Balancing also indicated that approximately 80% of the energy from the fire was deposited in the thick Kastolite enclosure walls.

To validate these findings, the total heat flux to the walls was calculated using the wall surface temperature histories and Duhamel integral techniques (Arpaci, V. S., 1966, and Nikanja, M. and Greif, R., 1978). Wall temperatures were extrapolated and averaged (McGehee, D., 1983) to represent the eight zones shown in Fig. A-4.

Figure A-10 shows four typical wall temperature curves for Mod 27B. The four zones represented are: 1 - the ceiling above the fire; 4 - top near wall; 5 - middle near wall; and 6 - bottom near wall. All eight zones behave similarly at early times with a rapid temperature rise, (~50°C in 4 min), before beginning their long approach to a quasi-steady distribution. The middle wall zone, 5, initially leads the top wall zone, 4, due to its greater view factor for direct radiation from the flame. However, after ~10 min, zone 4

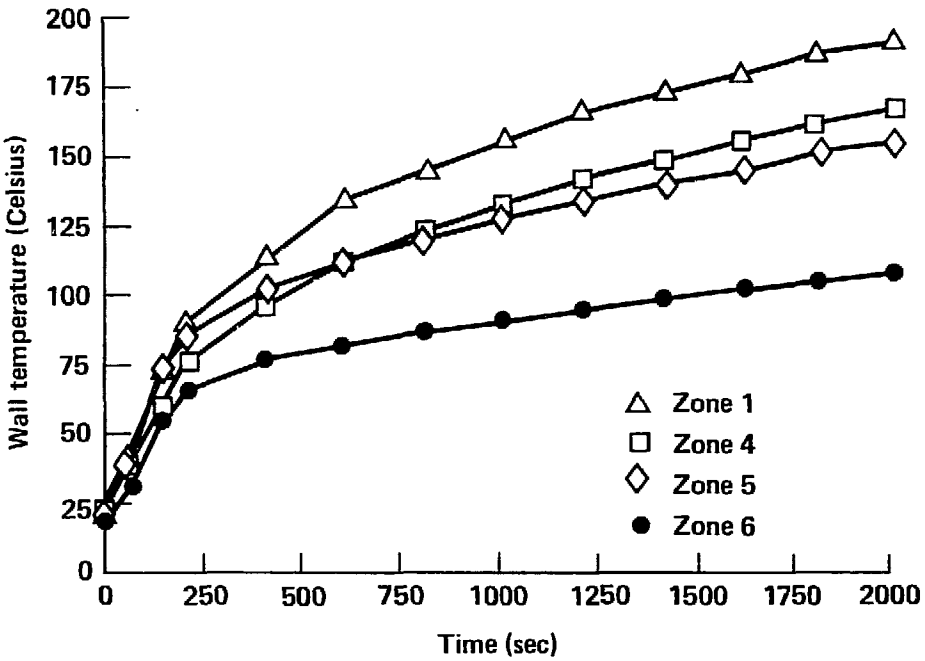

Figure A-10. Zonal wall temperatures for MOD 27B.

catches up with zone 5 because of increased radiation from the ceiling and hot upper layer. At long times, the upper zone, 4, temperatures exceed the middle zone, 5, by ~10°C.

The fast, early rise is attributed to the cold walls experiencing direct flame radiation, much like coming inside during winter to stand in front of a fireplace. Numerical curve fitting was done mimicking the two time regime behaviors shown in Fig. A-10, with a linear rise followed by a slow "baking" as the half power of time.

The data from each thermocouple in each zone was fit with

$$\theta_w = bt, \qquad \text{for } t < t_{tr} \qquad (1a)$$

and

$$\theta_w = c + ft^{1/2}, \qquad \text{for } t \geq t_{tr} \qquad (1b)$$

where $\theta_w = T_w - T_{wi}$, is the surface temperature increase above its initial value. t_{tr} is ~3 min. This time dependence, along with approximate wall thermal properties, in the standard Duhamel integral

$$q''(t) = \left(\frac{\kappa\rho c}{\pi}\right)^{1/2}\left[\frac{\theta_w(t)}{t^{1/2}} + \int_0^t \frac{\theta_w(t) - \theta_w(s)}{2(t-s)^{3/2}}\,ds\right] \qquad (2)$$

gives a local heat flux

$$q''(t) = (4b^2 t\,\kappa\rho\, c/\pi)^{1/2}, \qquad \text{for } t < t_{tr} \qquad (3a)$$

and

$$q''(t) = \left(\frac{\kappa\rho c}{\pi}\right)^{1/2}\left[\frac{c}{t^{1/2}} + bt_{tr}^{1/2} + f\left[2.57 - \sin^{-1}\frac{t_{tr}^{1/2}}{t} - \frac{(t^{1/2} - t_{tr}^{1/2})}{(t - t_{tr})^{1/2}}\right]\right] \text{ for } t > t_{tr}, \qquad (3b)$$

where $t_{tr} = (f + (f^2 + 4bc)^{1/2}/(2b))^2$.

To compensate for the error of concentrating the thermocouple array on that portion of the wall closest to the fire, a steric factor of 0.5 for the walls was introduced. This lowered the flux calculated from Eq. (3) to the level shown in Fig. A-11. The floor zones were deleted as negligible. Each thermocuople's flux was calculated and the flux average applied to the zone surface area to determine the total power into each zone as a function of time. Summing over all zones then gave the total power history to the test cell surface (McGehee, D., 1983).

Figure A-12 shows a comparison of this calculation with the estimate of Q determined from data obtained using the species, temperature and flow measurements in the exit duct for test 27B, 400 kW at 250 l/s. The total heat flux to the walls exhibits a peak that occurs at roughly the same time as the peak in the air inflow. Initially, both the convective and radiative heat transfer is large because of the large temperature difference between gas and surfaces and the direct view from the fire. The gas and wall temperatures rise in parallel and are somewhat interdependent. When the rate of gas temperature rise is reduced (~250 s), the rate of change in the wall temperature is slowed down, indicating a significantly reduced rate of heat transfer. As noted earlier, the magnitude of the air flow peak is directly dependent on fire strength. The same relationship holds for the heat rate peak corresponding to the heat transfer transition time, thus illustrating that the enclosure volume is so large that no ventilation control can occur during the first minutes of burning.

In addition, Fig. A-12 shows the results of calculating the convective fraction of the total heat flux using published correlations (Cooper, 1982 and Zukoski, *et al.*, 1975). The radiative fraction was then calculated as the difference between the total and the convective flux. In all cases, net radiation is from 2 to 4 times greater than convection. Spot checks with radiometer measurements indicate these radiation estimates are of the correct magnitude.

Table A-5 gives the flux distribution among zones and the partition of the absorbed energy into net radiation and convection at the long times indicated for several different tests. The fire strengths and mass flow rates for these tests are given in Table A-2. The last two columns give the calculated and measured fluxes averaged over the wall and ceiling surface areas. This agreement is good, considering the geometric averaging required and the uncertainties in measuring the surface temperatures. It is also difficult to get accurate average wall properties (Somerton, 1958). In the future, more complete radiation calculations are planned, both because of their own importance and their value in making a critical, full-scale evaluation

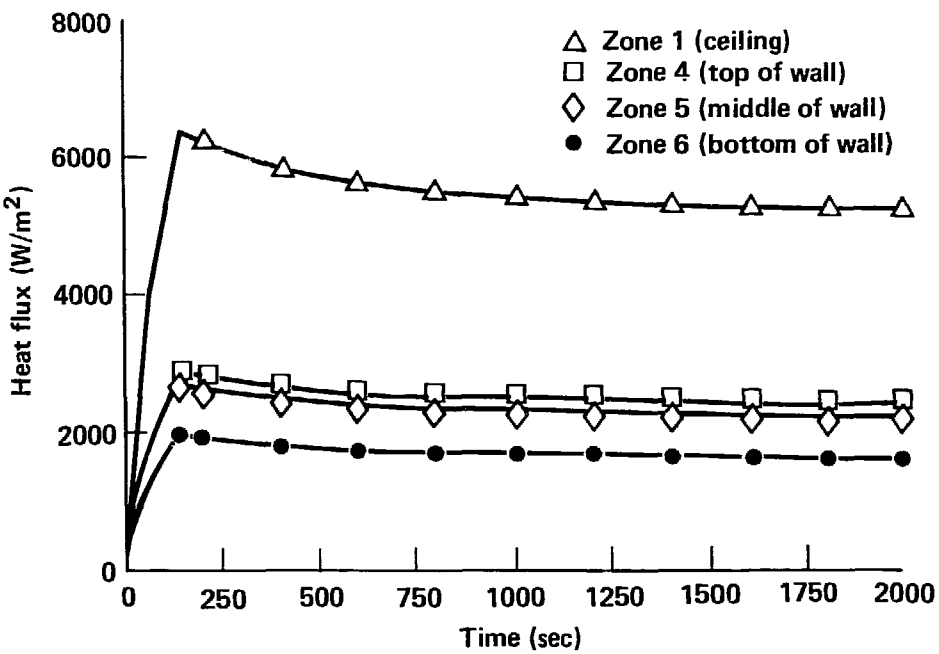

Figure A-11. Projected heat flux to wall zones for MOD 27B.

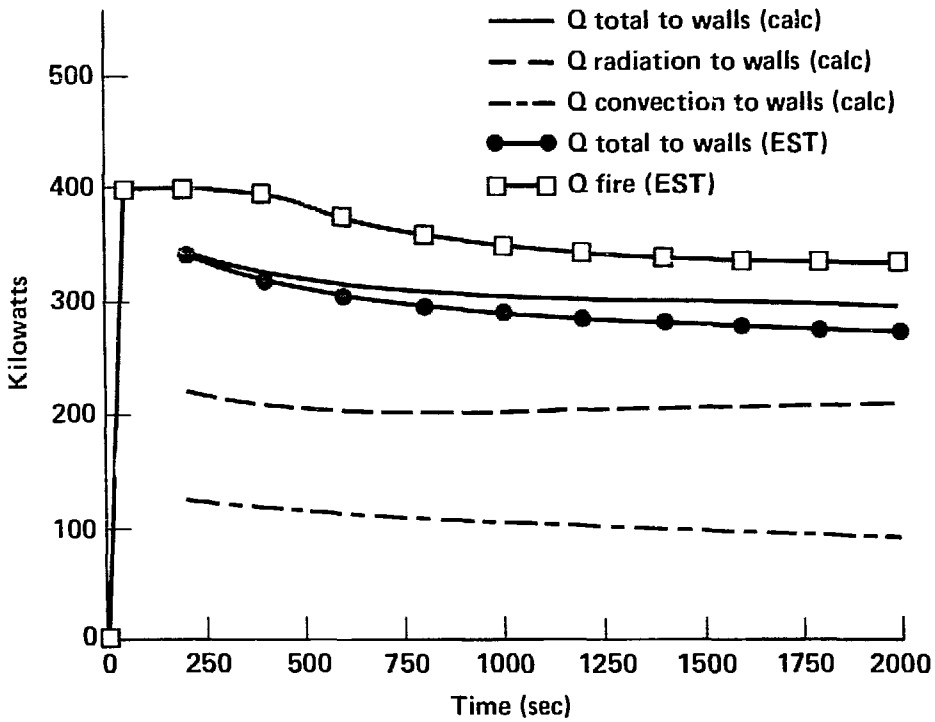

Figure A-12. Results of Duhamel analysis for MOD 27B.

of the convective correlations. Further tests are planned with a more representative thermocouple array embedded very slightly beneath the enclosure surface.

The literature suggests these tests are unique. The low inlet-high outlet ventilation pattern does not allow intermixing of the hot and cold layers. The thick Kastolite walls absorb 80% of the energy of the fire, keeping gas temperatures below 350°C. Half an hour is required to reach quasi-steady-state because of the large room volume. Having established these data as reliable and representative for these specific conditions, they are is used to compare several fire model predictions.

Enclosure-Fire-Model Validation

The model selection procedure used was unsophisticated. Data were sent to any organization or institution that expressed an interest in attempting to predict fire characteristics from the initial conditions of our tests. Three tests were selected for model validation analysis: MOD 8, MOD 9, and MOD 27B. These tests represent ventilated (400 kW at 500 L/s), and under-ventilated (800 kW at 500 L/s), and (400 kW at 250 L/s) fires. The six models compared in this report consist of those respondents who had the ability to modify their model to account for the unusual condition of forced ventilation. Five of the six codes were two-layer zone models from Harvard (Mitler and Emmons, 1981, and Mitler, 1982), LANL (Krause, 1982), LLNL (Creighton, 1982), Cal Tech II (Zukoski, 1980), and PNL (Orzawski, *et al.*, 1982). One code has a single layer zone code, Cal Tech I (Zukoski, 1982).

Eight fire parameters were selected for comparison of the models. They are listed here in order of their importance, both as model indicators and as parameters for risk analysis.

1. Upper layer gas tempreature (°C).
2. Fire strength (kW).
3. Total heat loss to walls (kW).
4. Oxygen concentration (% vol).
5. Lower layer height (m).
6. Inlet ventilation (g/sec).
7. Wall temperature (°C).
8. Lower layer gas temperature (°C).

Table A-5. Calculated heat fluxes.

Zone Number Area (m^2)	1 8 (kW/m^2)	2 8 (kW/m^2)	3 8 (kW/m^2)	4 18 (kW/m^2)	5 18 (kW/m^2)	6 18 (kW/m^2)	7 18 (kW/m^2)	8 18 (kW/m^2)	Ceiling Fluence 24 (kW)	Wall Fluence 90 (kW)	Cell Fluence 114 (kW)	Calc. Avg. Flux	Meas. Avg. Flux
Mod 7 at 1700 sec													
Convective	0.7	0.6	0.4	0.4	0.3	0.3	0.3	0.2	13.6	27.0	40.6	0.4	
Radiative	2.3	1.4	2.3	0.6	0.6	0.2	0.5	0.2	48.0	37.8	85.8	0.7	
Total	3.0	2.0	2.7	1.0	0.9	0.5	0.8	0.4	61.6	64.8	126.4	1.3	1.1
Mod 8 at 1100 sec													
Convective	1.8	1.2	0.9	0.9	0.6	0.6	0.7	0.5	31.2	59.4	90.6	0.8	
Radiative	4.8	5.5	5.2	1.4	1.8	1.1	1.3	1.3	124.0	124.2	248.2	2.2	
Total	6.6	6.7	6.1	2.3	2.4	1.7	2.0	1.8	155.2	183.6	338.8	3.0	3.1
Mod 9 at 550 sec													
Convective	3.1	1.9	1.4	1.3	0.9	0.8	0.9	0.6	51.2	81.0	132.2	1.1	
Radiative	9.0	11.6	11.0	3.8	3.5	2.3	3.1	2.8	252.8	279.0	531.8	2.2	
Total	12.1	13.5	12.4	5.1	4.4	3.1	4.0	3.4	304.0	360.0	664.0	5.8	5.5
Mod 17 at 2000 sec													
Convective	1.6	1.4	1.1	0.8	0.6	0.7	0.5	0.5	32.8	55.8	88.6	0.8	
Radiative	6.8	6.0	5.1	2.2	2.2	1.1	2.3	1.2	143.2	162.0	305.2	2.7	
Total	8.4	7.4	6.2	3.0	2.8	1.8	2.8	1.7	176.0	217.8	393.8	3.5	4.7
Mod 27B at 2000 sec													
Convective	1.9	1.4	1.0	0.8	0.6	0.6	0.6	0.4	34.4	54.0	88.4	0.8	
Radiative	3.3	3.4	3.2	1.6	1.6	1.0	1.4	1.3	79.2	124.2	203.4	1.8	
Total	5.2	4.8	4.2	2.4	2.2	1.6	2.0	1.7	113.6	178.2	291.8	2.6	2.6

Table A-6 contains quasi-steady-state test data and long-time model predictions for the three comparison tests. These tables present an overview of a model's abilities and performance relative to the other models, but they can be deceiving. A time history is a better indication of a model's accuracy. An example of this is illustrated in Table A-6(b). The upper layer temperature predictions of Cal Tech I and II, LANL and LLNL appear to agree well with the data. However, in Fig. A-13 (a)-(b), it is clear that the Cal Tech I program is simply intersecting the other predictions and the real data on the way to higher temperatures. The Cal Tech I program does not appear to approach quasi-steady state. LANL, PNL and Harvard have substantially better upper layer temperature "temporal shapes" but predict temperatures too high or too low. For all tests, Harvard's "temporal shape" agrees well with the data; however, it is significantly lower (80–120°C) than the data. It needs some improvement to allow more energy into the hot layer.

Looking at Table A-6, the Harvard code appears to have the best prediction of the fire strength in the ventilation limited condition. The Cal Tech I code requires that the oxygen concentration goes to zero before oxygen starvation occurs, limiting the fire strength. The oxygen concentration never approaches zero in these tests since ventilation control limits the burning rate. A realistic empirical O_2 limit could be incorporated into this code to improve it. The LLNL, LANL and Cal Tech II codes do not account for the possibility of oxygen starvation.

When comparing the prediction for heat loss to the walls it was clear that models which incorrectly predicted the fire strength would have problems. Therefore, they are compared using the ratio of the heat lost to the walls to the predicted fire strength. The Cal Tech I code was clearly better than the others in this regard (80–86%). The Harvard code (50%) was again troubled by its lack of energy in the hot layer, as was PNL (30–60%). The other three models require this ratio as an input parameter. The Borhamwood Fire Research Station finite difference program (Cox, 1983) was run for MOD 8 and predicted the heat loss quite well. The datra showed a 75% heat loss to the walls, and Cox predicted 76–77%.

Figure A-14 (a)-(b) compares the actual oxygen depletion curves for MOD 9 and MOD 27B with the four models that attempt to predict it. None of the programs predict oxygen depletion very well in these underventilated tests. The Cal Tech I model does, however, predict a consistently low depletion value (i.e., more O_2 consumption). This is a more useful program from a risk-analysis viewpoint in that it doesn't underestimate the hazard. The PNL prediction for MOD 9 diverges from the data and other predictions at 11% O_2, illustrating this model's threshold of ventilation control.

No model was completely successful in predicting all eight parameters evaluated. In fact, no model was consistently close ($\pm 5\%$) on any parameter except fire strength. Most models were inconsistent, giving good predictions on one parameter and missing altogether on others. The overall performance evaluation process was very difficult. Nevertheless, it is possible to tentatively order the models relative to their usefulness in predicting the results of forced ventilation enclosure fires. In this order, the Cal Tech I and the PNL codes were the most successful. The Harvard and LANL codes were found to be moderately useful, whereas the modest abilities and questionable results of the LLNL and Cal Tech II codes make their usefulness limited.

Conclusions

These tests provide new insights on the complexities of a fire in forced ventilation enclosures and should prove useful in future fire risk analyses of fires in these enclosures. They provide a firm foundation for further tests. Additional tests have been completed, in which the position of the fire was moved within the room and the location of ventilation ducts and wall thermocouples was changed. Preliminary results indicate that sharper thermal layering occurs when the fire is elevated. Subsequent tests will better define the interaction of ventilation and fire locations.

Data comparisons also point out the deficiencies of the current fire models to predict the important parameters of a fire in a forced ventilation enclosure. Some of the difficulties are minor problems with simple solutions; others are more complex. As more data become available, these problems may be solved. None of the current programs, however, are ready for unqualified use in fire hazard risk analyses.

Table A-6. Comparison of model predictions with tests data MOD 8.

Units	Data	Harvard	Cal Tech I	PNL	LANL	Cal Tech II	LLNL
Time (sec)	1200	1200	1200	1000	500	800	300
Upper Layer Temp (°C)	232	152	228	272	163	160	191
Fire strength (kW)	400	395	399	400	391	400	400
Heat loss to walls (kW)	300	182	317	126	313	320	320
Oxygen concentration (% vol)	14.0	12.1	13.3	16.3	14.7	–	–
Lower layer height (m)	1.30	0.36	–	0.80	2.84	0.30	0.99
Wall temperature (°C)	135-180	113	151	–	–	–	–
Lower layer temp (°C)	112	21	228	272	80	21	21
Inlet spike min (sec)	(40)	(2)	(50)	(20)	(11)	(30)	–
Inlet spike (g/sec)	25.0	90	100	−80	75	344	–

MOD 9

Units	Data	Harvard	Cal Tech I	PNL	LANL	Cal Tech II	LLNL
Time (sec)	600	600	600	600	630	800	300
Upper Layer Temp (°C)	299	175	351	267	329	304	388
Fire strength (kW)	700	482	801	556	786	800	800
Heat loss to walls (kW)	600	231	682	327	629	640	640
Oxygen concentration (% vol)	6.5	7.6	4.0	10.8	7.9	–	–
Lower layer height (m)	1.29	0.33	–	0.75	2.25	0.25	0.87
Wall temperature (°C)	170-270	126	215	–	–	–	–
Lower layer temp (°C)	146	34	351	34	136	34	34
Inlet spike min (sec)	(15)	(2)	(20)	(20)	(11)	(30)	–
Inlet spike (g/sec)	−420	−554	−570	-180	−400	117	–

MOD 27B

Units	Data	Harvard	Cal Tech I	PNL	LANL	Cal Tech II	LLNL
Time (sec)	2200	2200	2200	2200	1800	800	300
Upper Layer Temp (°C)	252	158	287	222	282	287	287
Fire strength (kW)	330	341	399	295	391	400	400
Heat loss to walls (kW)	270	165	329	154	313	320	320
Oxygen concentration (% vol)	11.0	6.8	9.4	11.3	9.6	–	–
Lower layer height (m)	1.22	0.28	–	0.64	0.73	0.15	0.75
Wall temperature (°C)	180-210	123	206	–	–	–	–
Lower layer temp (°C)	136	18	287	87	111	18	18
Inlet spike min (sec)	(15)	(2)	(20)	(20)	(20)	(30)	–
Inlet spike (g/sec)	−200	−210	−300	−410	−210	34	–

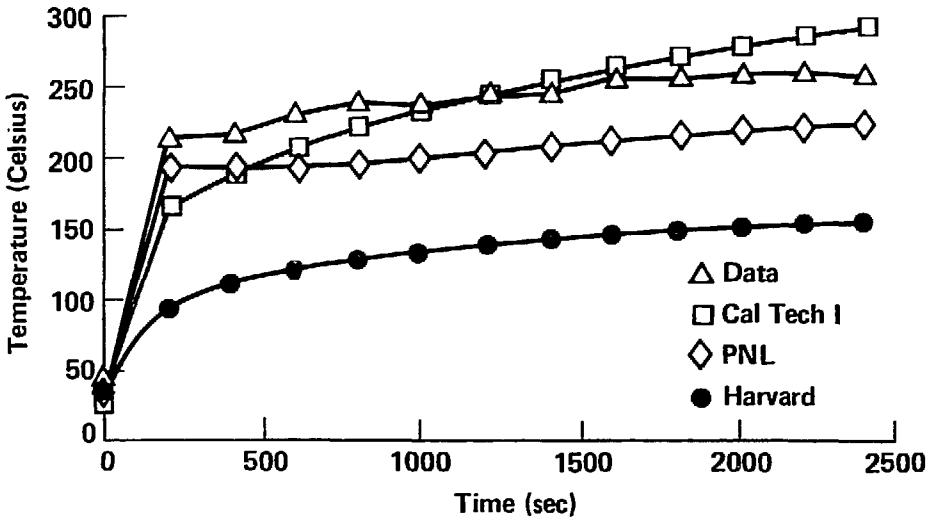

Figure A-13(a). Comparison of several models' gas temperature predictions for MOD 27B.

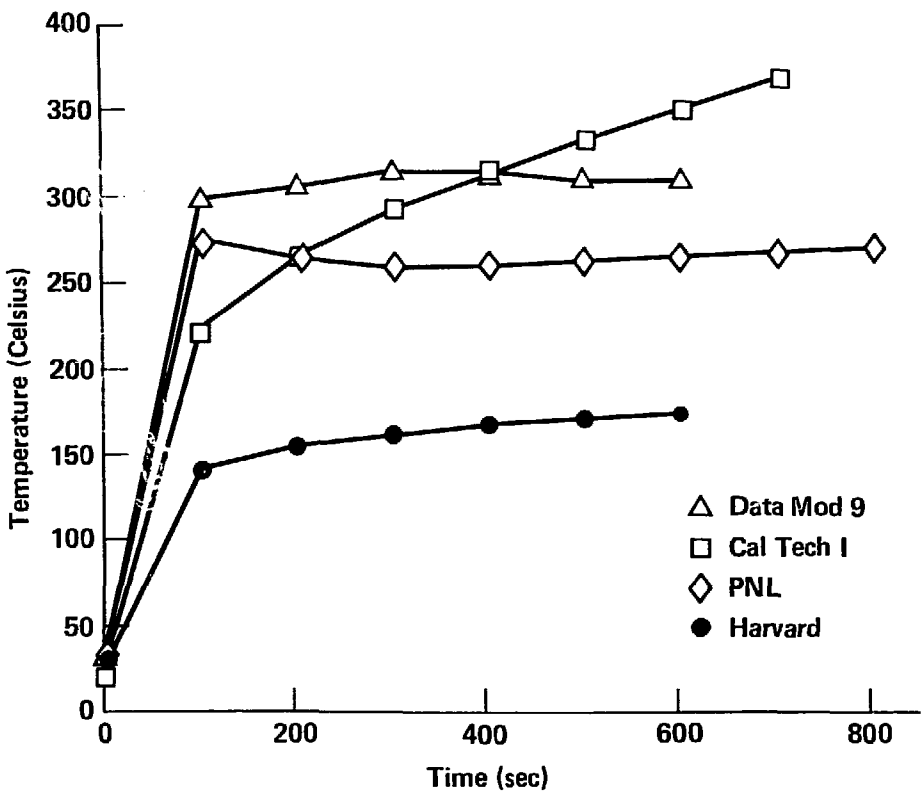

Figure A-13(b). Comparison of several models' gas temperature predictions for MOD 9B.

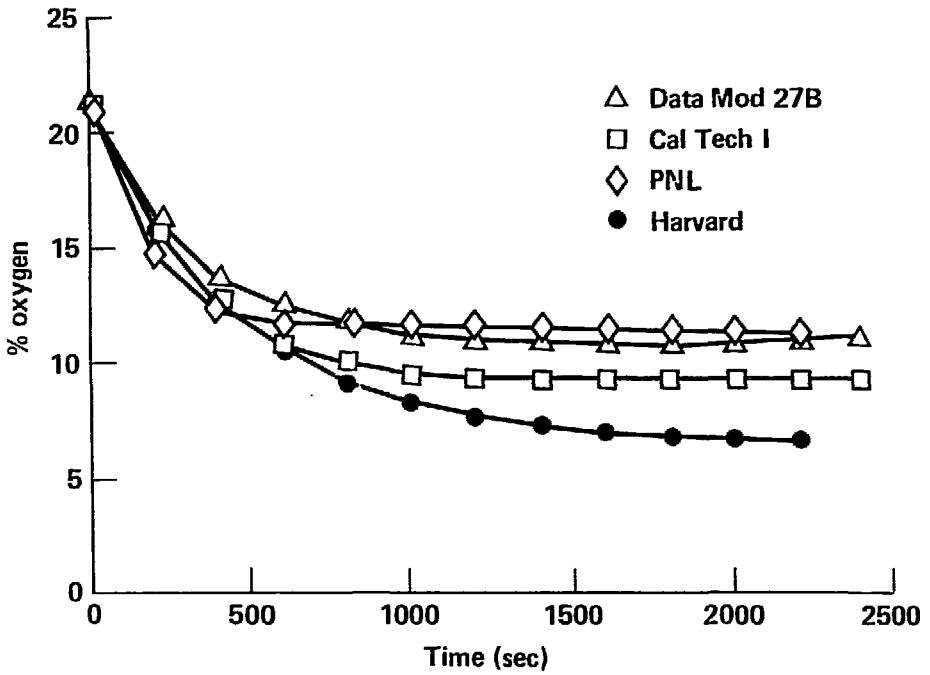

Figure A-14(a). Comparison of several models' oxygen depletion predictions for MOD 27B.

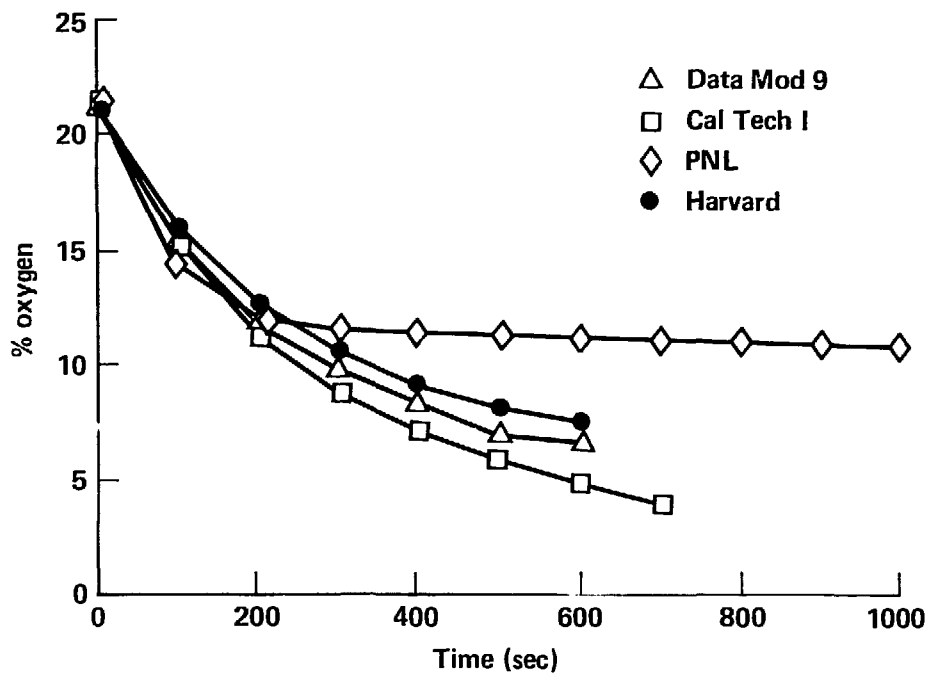

Figure A-14(b). Comparison of several models' oxygen depletion predictions for MOD 9.

Acknowledgments

We wish to thank all the modelers who took interest and participated in the model-evaluation process. We particularly thank Professor E. E. Zukoski from Cal Tech and Dr. Dick Gregory, Dr. Fritz Krause and Mr. Dick Martin from LANL for their help in designing the experimental series. We are grateful for the work done by Don Beason, Steve Priante and Kirk Staggs in setting up and performing the actual tests.

References

Alvares, N. J., Hasegawa, H. K., Lipska-Quinn, A. E., (1981), "Fire Protection Countermeasures for Containment Ventilation Systems," *Proc. 16th DOE Nuc. Air Cleaning Conf.*, p. 1213–1277.

Alvares, N. J., Hasegawa, H. K., Lipska-Quinn, A. E., (1982). Fire Protection Research for Energy Technology Projects. Report UCRL-53179, LLNL, University of California, Livermore, 18–27.

Arpaci, V. S. (1966). *Conduction Heat Transfer*, Addison-Wesley, Reading, Mass. p. 307.

Cleary, W. M. (Ed). (1979). *Industrial Ventilation*, Edward Brothers, Inc., Ann Arbor, MI.

Cooper, L. Y. (1981). Heat Transfer from a Buoyant Plume to an Unconfined Ceiling, Paper 81-MT-7, 20th ASME-AICME, Nat'l. Heat Transfer Conf.

Cox, G. (1983). A Field Model of Fire and Its Application to Nuclear Containment Problems. Proc. CSNI Specialist Meeting, CSNI Report.

Creighton, J. R., (1982). Simplified Two-Layer Model for LLNL Test Cell, LLNL, University of California.

Krause, F. R., and Gregory, W. S. (1982). Simulation of Forced Ventilation Fires. Proc. 17th DOE Air Cleaning Conf., Paper 9-3.

Mitler, H. E., and Emmons, H. W. (1981). Documentation for CFCV, The Fifth Harvard Computer Fire Code. Nat'l. Bureau of Standards Report, NBS Grant, 67-9011.

Mitler, H. E. (1982). Simulation of Large Fires with Forced Ventilation. Fuel Cycle Facility Safety Research Program Review Meeting #11, FMRC.

McGehee, D. (1983). Radiative and Convective Heat Transfer in a Compartment Fire. LLNL Report in press 1984.

Nikanja, M., and Greif, R. (1978). Heat Transfer During Piston Compression. Journal of Heat Transfer, Vol. 100, Aug. 1978, p. 527–530.

Orloff, L. (1981). Simplified Radiation Modeling of Pool Fires. 18th Combustion Symposium, p. 549–561, The Combustion Institute.

Orzawski, P. C., Chan, M. K. W., Ballinger, M. Y., (1982). FIRIN1 - A Fire Source Term Computer Code, Fuel Cycle Facility Safety Research Program Review Meeting #11, FMRC.

Sumerton, W. M. (1958). Some Thermal Properties of Porous Rocks. AIME PET. TRANs. 213, p. 61.

Zukoski, E. E. and Kubota, T. (1975). An Experimental Investigation of the Heat Transfer from a Buoyant Gas Plume to a Horizontal Ceiling - Part 2: Effects of Ceiling Layer. Cal. Inst. Tech. Nat. Bur. Stand. NBS. GRC 77-98.

Zukoski, E. E. and Kubota, T. (1980). Two-Layer Modeling of Smoke Movement in Building Fires. Fire and Materials, 4, p. 19.

Zukoski, E. E. (1982). Personal Correspondence.

Appendix B
Mocho Standpipe Digraph

The bold arrows in Fig. B-1 represent normal information flow and logic. That is, if the system is operating normally, these bold lines describe the normal cause-and-effect between dependent and independent system variables. The detailed system digraph is rearranged around the following control loops: (1) control loop to turn the lead pump on and off, (2) control loop to turn the lag pump on and off, and (3) control loop to open and close the main control valve.

Disturbances and Upset Conditions

After these control loops, which are negative feedback loops, are identified, events such as equipment and instrument failure are included. These events can affect the control loops by either creating a low-level condition in the standpipes or storage tanks, or can shut down the system. These events are circled by dashed lines. As described in Dunglinson *et al.*, these are initiating events that upset conditions which in turn causes the Top Event to occur.

Modeling Information Flow to the Operator in Bldg. 511

Alarms in Bldg. 511 indicating upset conditions are modeled as feedforward loops. These feedforward loops symbolize mitigative actions the operator must take to restore an adequate water supply such as (1) manually opening the main control valve, or (2) cutting in Zone 7 in the event of failure of the Mocho system. In order for the operator to fail to take the corrective action, failure of the alarm system or operator must occur. The events are modeled as zero gain events, symbolized by "0." Zero gain events represent events which nullify the information flow.

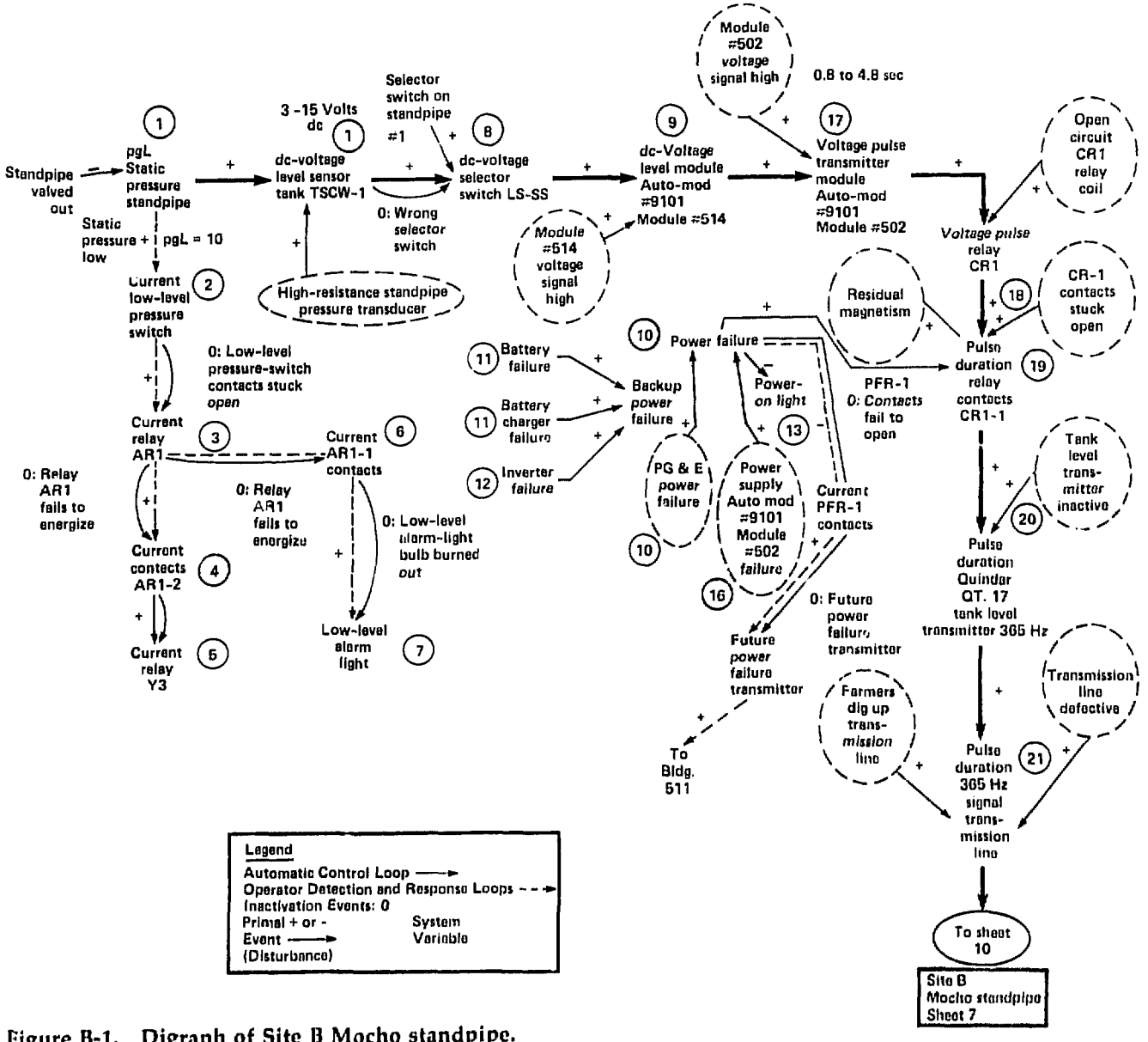

Figure B-1. Digraph of Site B Mocho standpipe.

Appendix C
Water-Supply-System Fault Tree

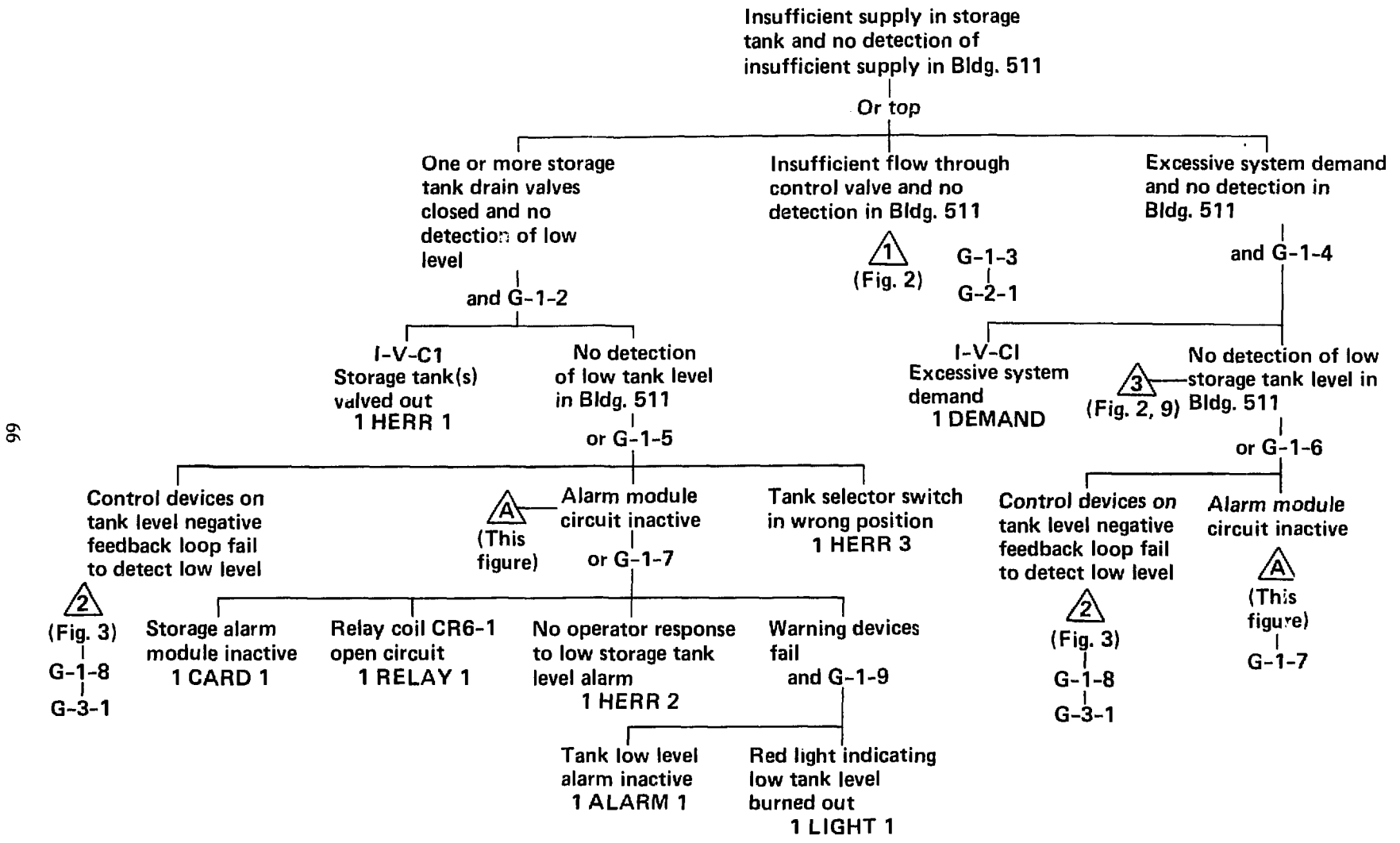
Insufficient supply in storage tank and no detection of insufficient supply in Bldg. 511
Or top
One or more storage tank drain valves closed and no detection of low level
and G-1-2
I-V-C1 Storage tank(s) valved out 1 HERR 1
No detection of low tank level in Bldg. 511
or G-1-5
Control devices on tank level negative feedback loop fail to detect low level
2 (Fig. 3)
G-1-8
G-3-1
A (This figure)
Alarm module circuit inactive
or G-1-7
Storage alarm module inactive 1 CARD 1
Relay coil CR6-1 open circuit 1 RELAY 1
No operator response to low storage tank level alarm 1 HERR 2
Warning devices fail
and G-1-9
Tank low level alarm inactive 1 ALARM 1
Red light indicating low tank level burned out 1 LIGHT 1
Tank selector switch in wrong position 1 HERR 3
Insufficient flow through control valve and no detection in Bldg. 511
1 (Fig. 2)
G-1-3
G-2-1
Excessive system demand and no detection in Bldg. 511
and G-1-4
I-V-CI Excessive system demand 1 DEMAND
3 (Fig. 2, 9)
No detection of low storage tank level in Bldg. 511
or G-1-6
Control devices on tank level negative feedback loop fail to detect low level
2 (Fig. 3)
G-1-8
G-3-1
Alarm module circuit inactive
A (This figure)
G-1-7

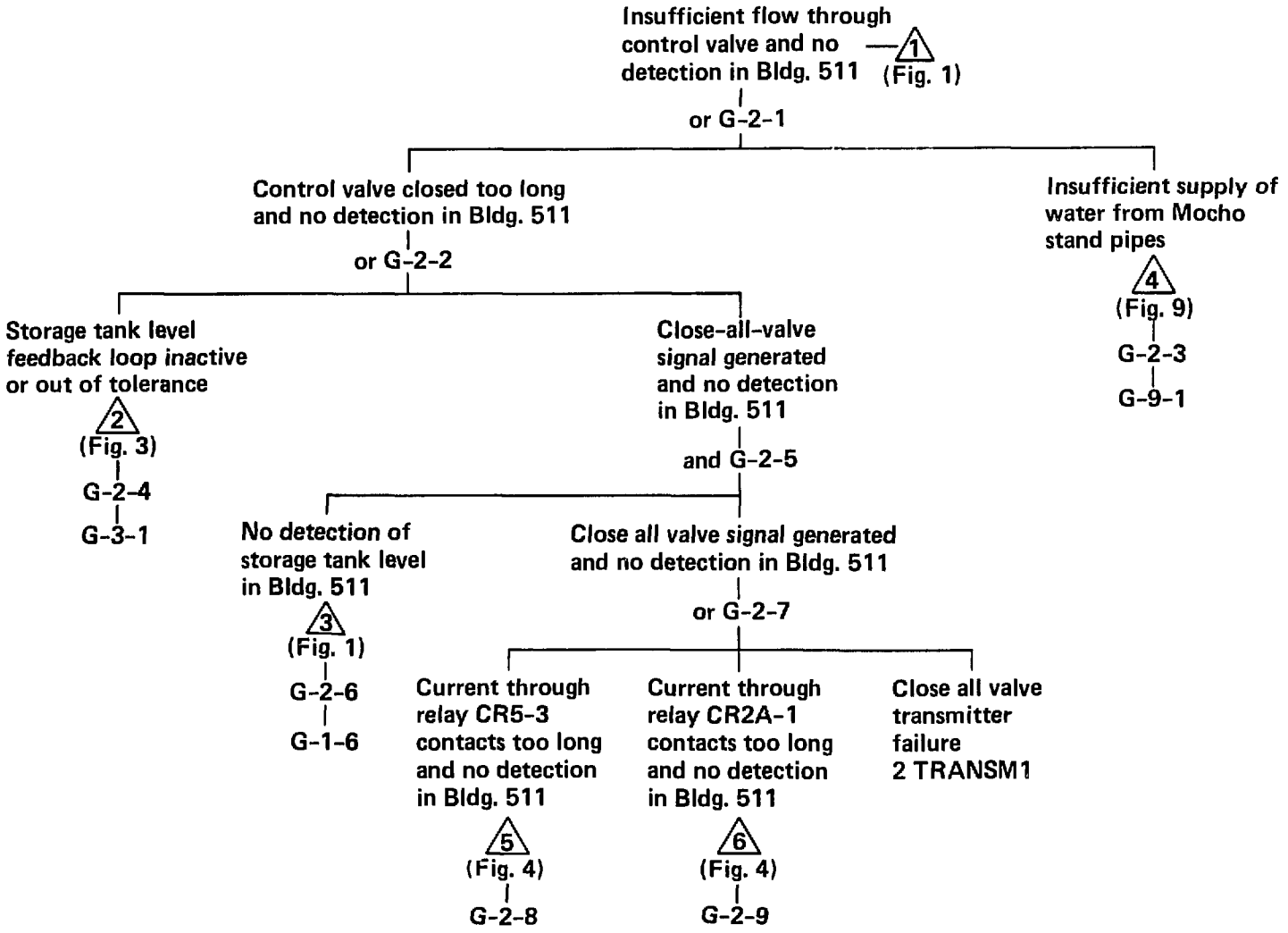
Insufficient flow through control valve and no detection in Bldg. 511
1
(Fig. 1)
or G-2-1
Control valve closed too long and no detection in Bldg. 511
or G-2-2
Insufficient supply of water from Mocho stand pipes
4
(Fig. 9)
G-2-3
G-9-1
Storage tank level feedback loop inactive or out of tolerance
2
(Fig. 3)
G-2-4
G-3-1
Close-all-valve signal generated and no detection in Bldg. 511
and G-2-5
No detection of storage tank level in Bldg. 511
3
(Fig. 1)
G-2-6
G-1-6
Close all valve signal generated and no detection in Bldg. 511
or G-2-7
Current through relay CR5-3 contacts too long and no detection in Bldg. 511
5
(Fig. 4)
G-2-8
Current through relay CR2A-1 contacts too long and no detection in Bldg. 511
6
(Fig. 4)
G-2-9
Close all valve transmitter failure 2 TRANSM1

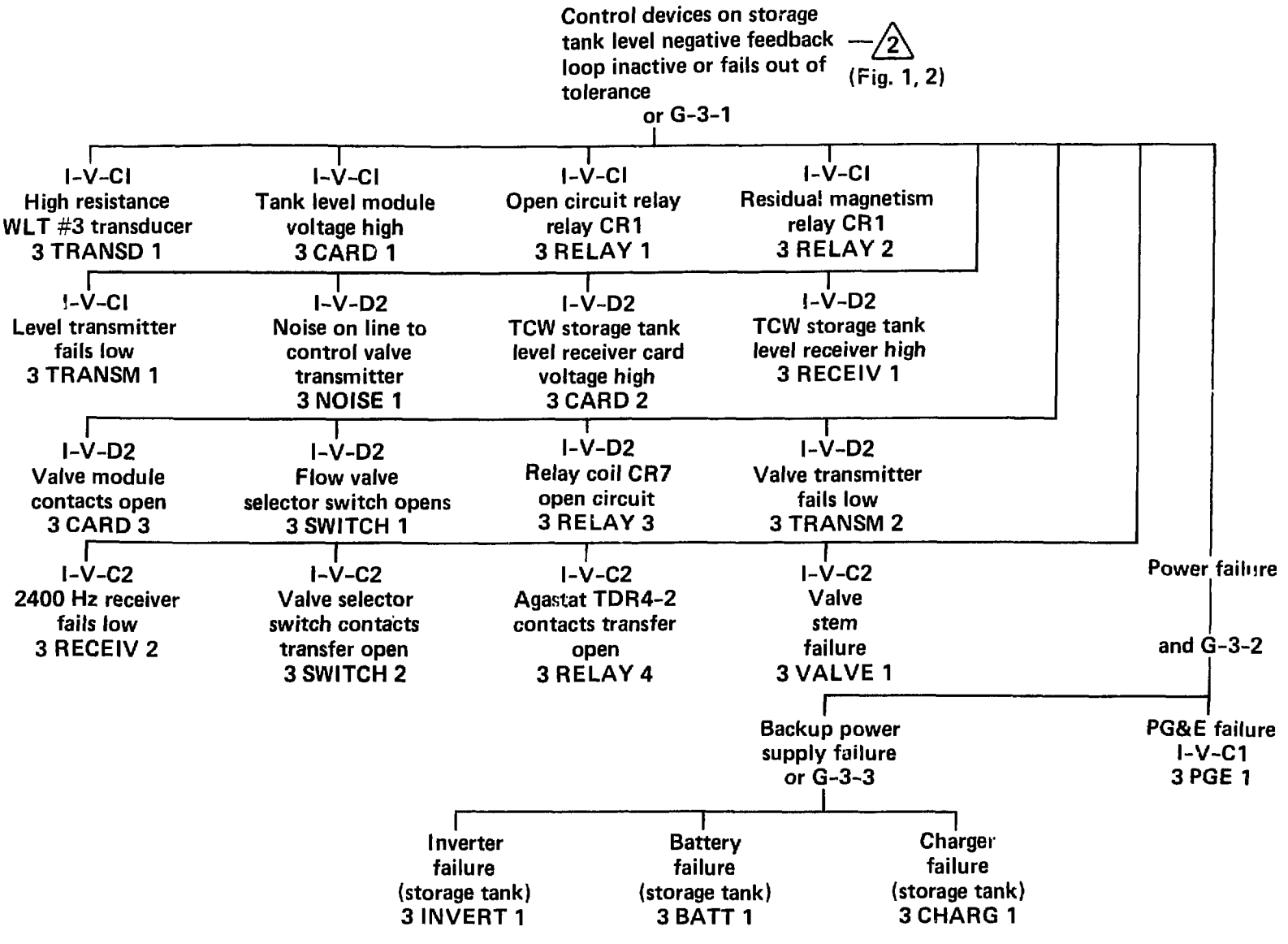
Control devices on storage tank level negative feedback loop inactive or fails out of tolerance
or G-3-1
2
(Fig. 1, 2)
I-V-CI
High resistance WLT #3 transducer
3 TRANSD 1
I-V-CI
Tank level module voltage high
3 CARD 1
I-V-CI
Open circuit relay relay CR1
3 RELAY 1
I-V-CI
Residual magnetism relay CR1
3 RELAY 2
I-V-CI
Level transmitter fails low
3 TRANSM 1
I-V-D2
Noise on line to control valve transmitter
3 NOISE 1
I-V-D2
TCW storage tank level receiver card voltage high
3 CARD 2
I-V-D2
TCW storage tank level receiver high
3 RECEIV 1
I-V-D2
Valve module contacts open
3 CARD 3
I-V-D2
Flow valve selector switch opens
3 SWITCH 1
I-V-D2
Relay coil CR7 open circuit
3 RELAY 3
I-V-D2
Valve transmitter fails low
3 TRANSM 2
I-V-C2
2400 Hz receiver fails low
3 RECEIV 2
I-V-C2
Valve selector switch contacts transfer open
3 SWITCH 2
I-V-C2
Agastat TDR4-2 contacts transfer open
3 RELAY 4
I-V-C2
Valve stem failure
3 VALVE 1
Power failure
and G-3-2
Backup power supply failure
or G-3-3
PG&E failure
I-V-C1
3 PGE 1
Inverter failure (storage tank)
3 INVERT 1
Battery failure (storage tank)
3 BATT 1
Charger failure (storage tank)
3 CHARG 1

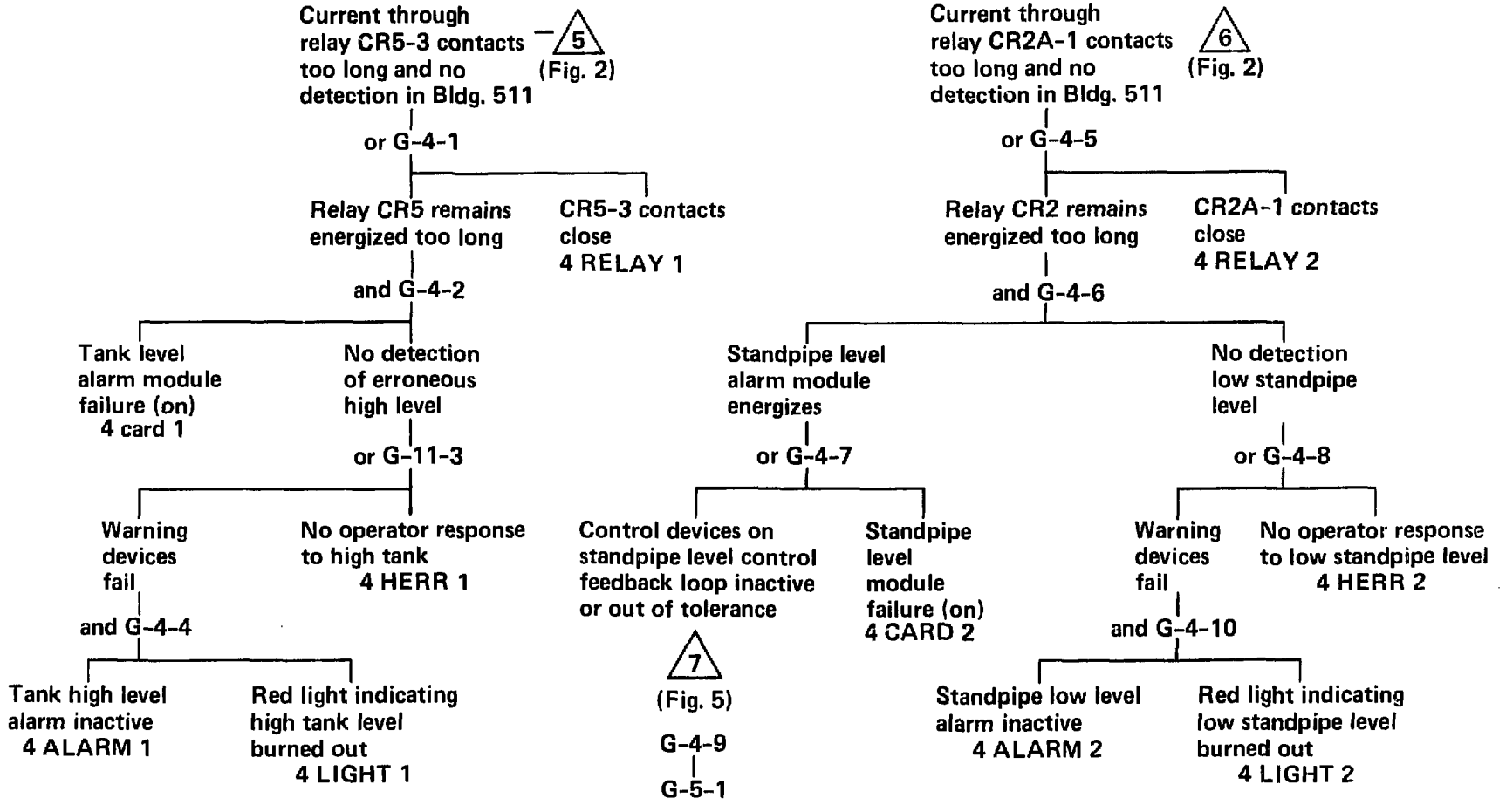
Current through relay CR5-3 contacts too long and no detection in Bldg. 511
5
(Fig. 2)
or G-4-1
Relay CR5 remains energized too long
CR5-3 contacts close
4 RELAY 1
and G-4-2
Tank level alarm module failure (on)
4 card 1
No detection of erroneous high level
or G-11-3
Warning devices fail
No operator response to high tank
4 HERR 1
and G-4-4
Tank high level alarm inactive
4 ALARM 1
Red light indicating high tank level burned out
4 LIGHT 1
Current through relay CR2A-1 contacts too long and no detection in Bldg. 511
6
(Fig. 2)
or G-4-5
Relay CR2 remains energized too long
CR2A-1 contacts close
4 RELAY 2
and G-4-6
Standpipe level alarm module energizes
No detection low standpipe level
or G-4-7
or G-4-8
Control devices on standpipe level control feedback loop inactive or out of tolerance
Standpipe level module failure (on)
4 CARD 2
Warning devices fail
No operator response to low standpipe level
4 HERR 2
and G-4-10
7
(Fig. 5)
G-4-9
G-5-1
Standpipe low level alarm inactive
4 ALARM 2
Red light indicating low standpipe level burned out
4 LIGHT 2

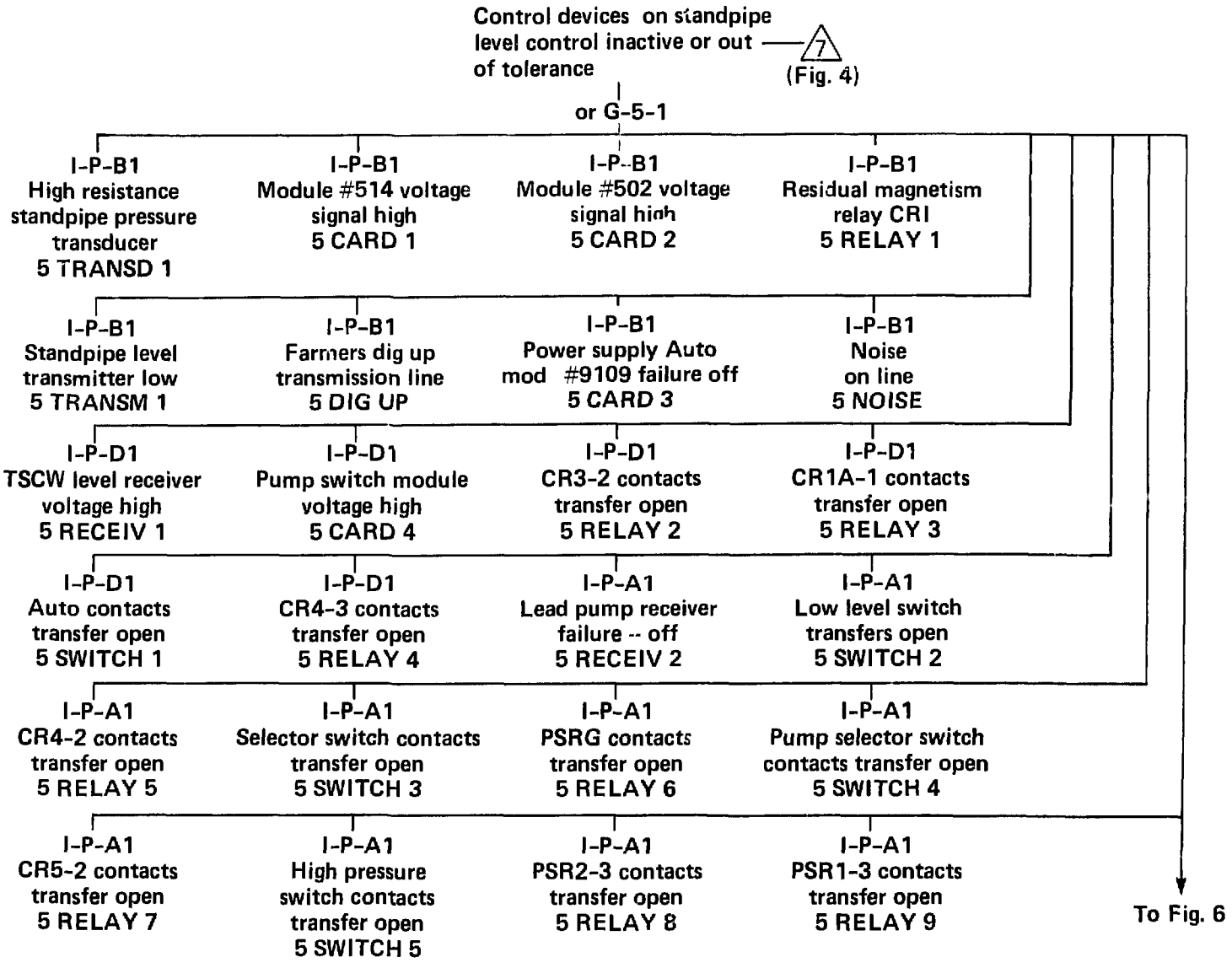
Control devices on standpipe level control inactive or out of tolerance
7
(Fig. 4)
or G-5-1
I-P-B1 High resistance standpipe pressure transducer 5 TRANSD 1
I-P-B1 Module #514 voltage signal high 5 CARD 1
I-P-B1 Module #502 voltage signal high 5 CARD 2
I-P-B1 Residual magnetism relay CR1 5 RELAY 1
I-P-B1 Standpipe level transmitter low 5 TRANSM 1
I-P-B1 Farmers dig up transmission line 5 DIG UP
I-P-B1 Power supply Auto mod #9109 failure off 5 CARD 3
I-P-B1 Noise on line 5 NOISE
I-P-D1 TSCW level receiver voltage high 5 RECEIV 1
I-P-D1 Pump switch module voltage high 5 CARD 4
I-P-D1 CR3-2 contacts transfer open 5 RELAY 2
I-P-D1 CR1A-1 contacts transfer open 5 RELAY 3
I-P-D1 Auto contacts transfer open 5 SWITCH 1
I-P-D1 CR4-3 contacts transfer open 5 RELAY 4
I-P-A1 Lead pump receiver failure -- off 5 RECEIV 2
I-P-A1 Low level switch transfers open 5 SWITCH 2
I-P-A1 CR4-2 contacts transfer open 5 RELAY 5
I-P-A1 Selector switch contacts transfer open 5 SWITCH 3
I-P-A1 PSRG contacts transfer open 5 RELAY 6
I-P-A1 Pump selector switch contacts transfer open 5 SWITCH 4
I-P-A1 CR5-2 contacts transfer open 5 RELAY 7
I-P-A1 High pressure switch contacts transfer open 5 SWITCH 5
I-P-A1 PSR2-3 contacts transfer open 5 RELAY 8
I-P-A1 PSR1-3 contacts transfer open 5 RELAY 9
To Fig. 6

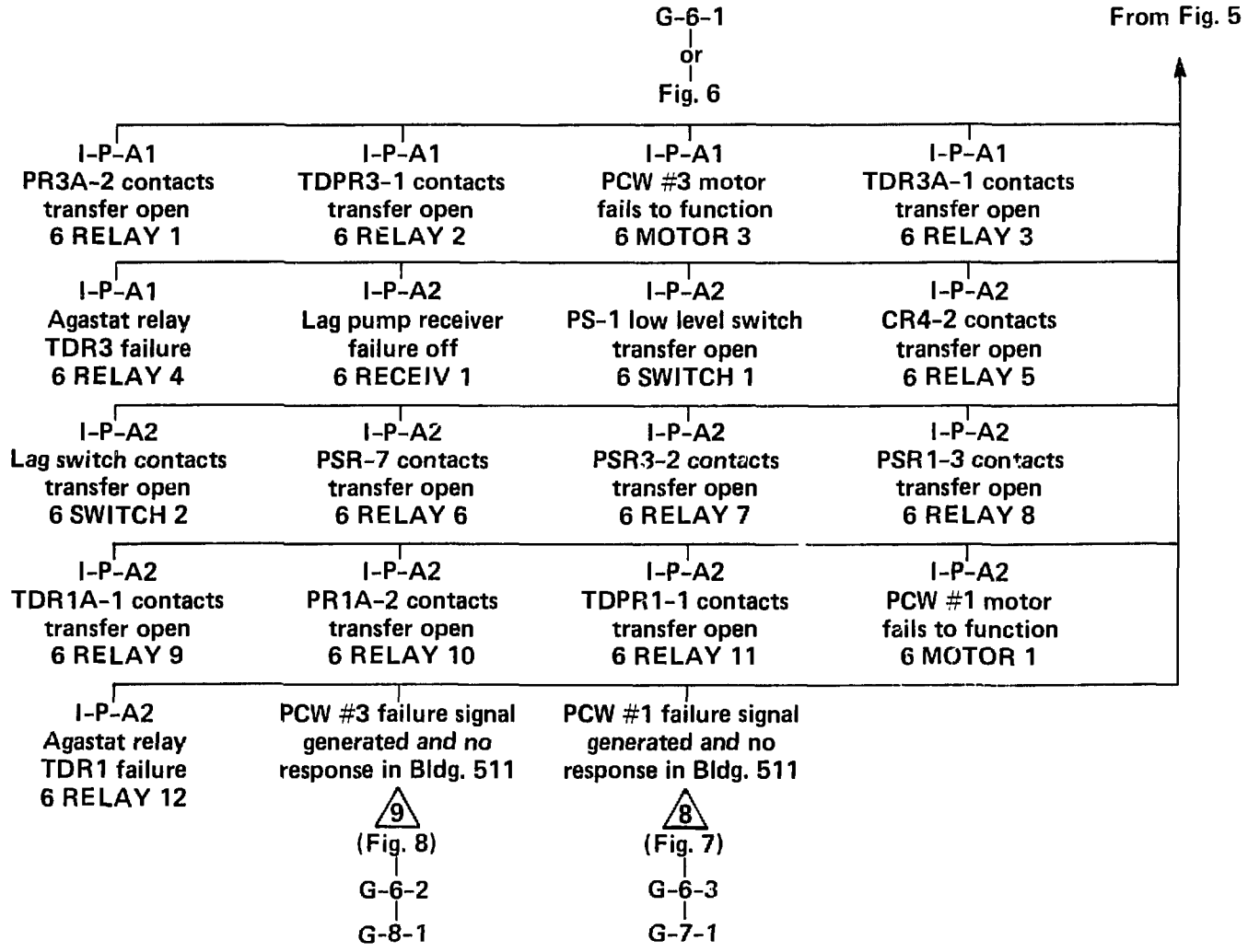
G-6-1
or
Fig. 6
From Fig. 5
I-P-A1
PR3A-2 contacts
transfer open
6 RELAY 1
I-P-A1
TDPR3-1 contacts
transfer open
6 RELAY 2
I-P-A1
PCW #3 motor
fails to function
6 MOTOR 3
I-P-A1
TDR3A-1 contacts
transfer open
6 RELAY 3
I-P-A1
Agastat relay
TDR3 failure
6 RELAY 4
I-P-A2
Lag pump receiver
failure off
6 RECEIV 1
I-P-A2
PS-1 low level switch
transfer open
6 SWITCH 1
I-P-A2
CR4-2 contacts
transfer open
6 RELAY 5
I-P-A2
Lag switch contacts
transfer open
6 SWITCH 2
I-P-A2
PSR-7 contacts
transfer open
6 RELAY 6
I-P-A2
PSR3-2 contacts
transfer open
6 RELAY 7
I-P-A2
PSR1-3 contacts
transfer open
6 RELAY 8
I-P-A2
TDR1A-1 contacts
transfer open
6 RELAY 9
I-P-A2
PR1A-2 contacts
transfer open
6 RELAY 10
I-P-A2
TDPR1-1 contacts
transfer open
6 RELAY 11
I-P-A2
PCW #1 motor
fails to function
6 MOTOR 1
I-P-A2
Agastat relay
TDR1 failure
6 RELAY 12
PCW #3 failure signal
generated and no
response in Bldg. 511
9
(Fig. 8)
G-6-2
G-8-1
PCW #1 failure signal
generated and no
response in Bldg. 511
8
(Fig. 7)
G-6-3
G-7-1

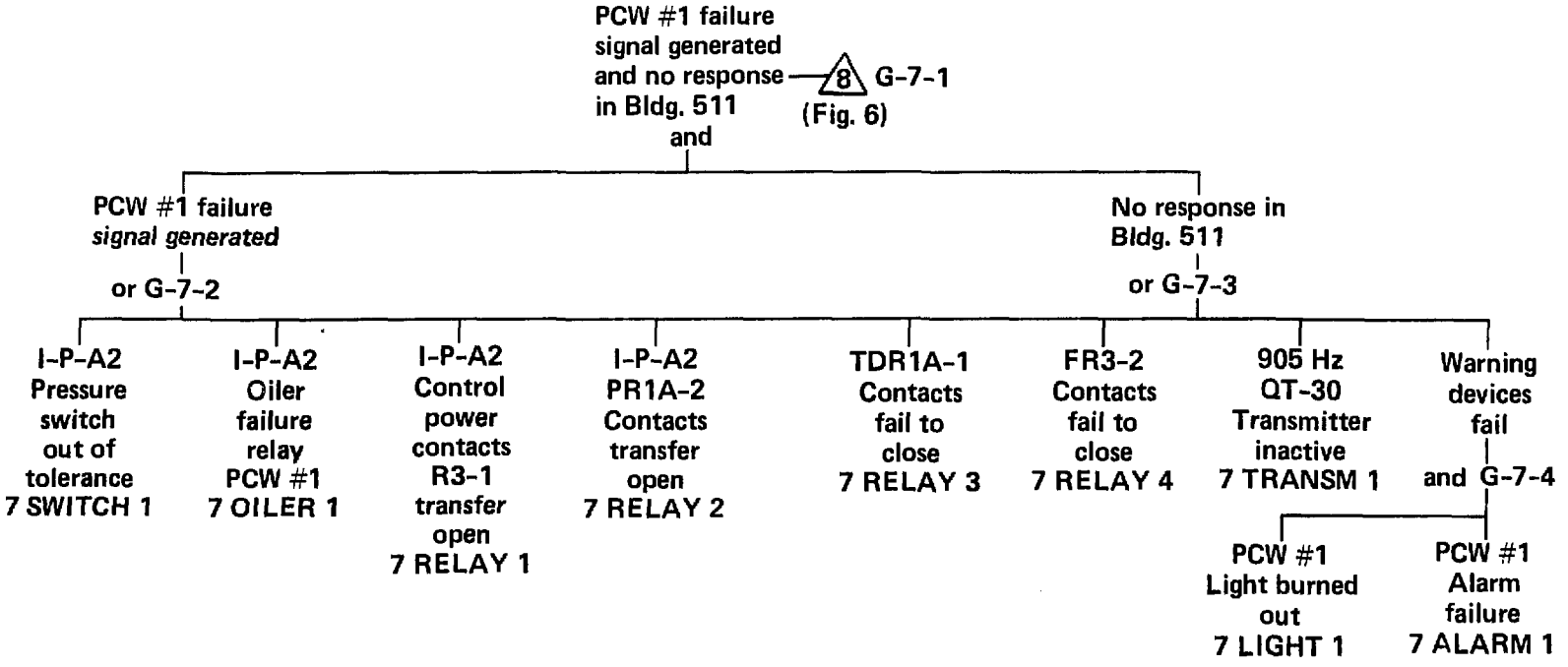
PCW #1 failure signal generated and no response in Bldg. 511
and
8 G-7-1 (Fig. 6)
PCW #1 failure signal generated
or G-7-2
No response in Bldg. 511
or G-7-3
I-P-A2 Pressure switch out of tolerance 7 SWITCH 1
I-P-A2 Oiler failure relay PCW #1 7 OILER 1
I-P-A2 Control power contacts R3-1 transfer open 7 RELAY 1
I-P-A2 PR1A-2 Contacts transfer open 7 RELAY 2
TDR1A-1 Contacts fail to close 7 RELAY 3
FR3-2 Contacts fail to close 7 RELAY 4
905 Hz QT-30 Transmitter inactive 7 TRANSM 1
Warning devices fail
and G-7-4
PCW #1 Light burned out 7 LIGHT 1
PCW #1 Alarm failure 7 ALARM 1

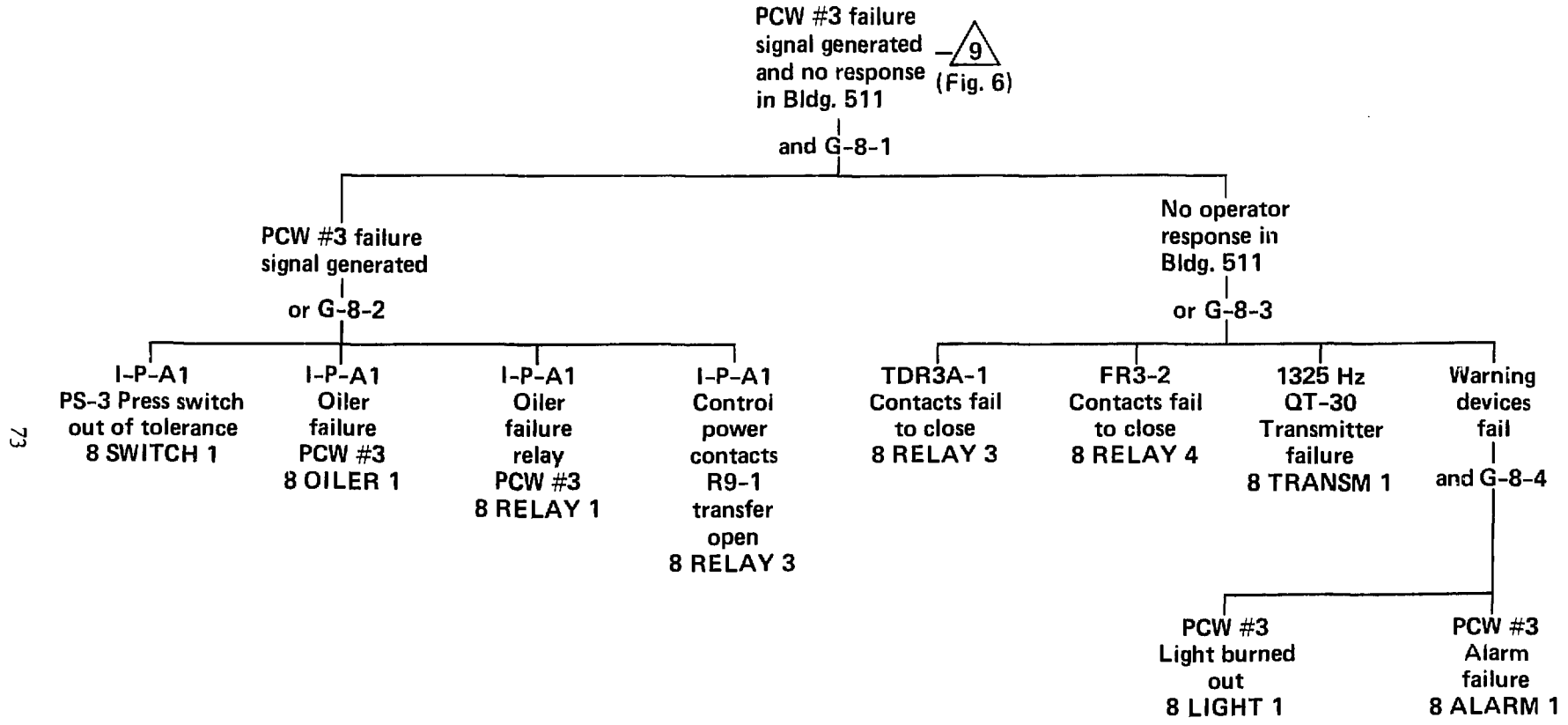
PCW #3 failure signal generated and no response in Bldg. 511
9
(Fig. 6)
and G-8-1
PCW #3 failure signal generated
or G-8-2
No operator response in Bldg. 511
or G-8-3
I-P-A1 PS-3 Press switch out of tolerance 8 SWITCH 1
I-P-A1 Oiler failure PCW #3 8 OILER 1
I-P-A1 Oiler failure relay PCW #3 8 RELAY 1
I-P-A1 Control power contacts R9-1 transfer open 8 RELAY 3
TDR3A-1 Contacts fail to close 8 RELAY 3
FR3-2 Contacts fail to close 8 RELAY 4
1325 Hz QT-30 Transmitter failure 8 TRANSM 1
Warning devices fail
and G-8-4
PCW #3 Light burned out 8 LIGHT 1
PCW #3 Alarm failure 8 ALARM 1

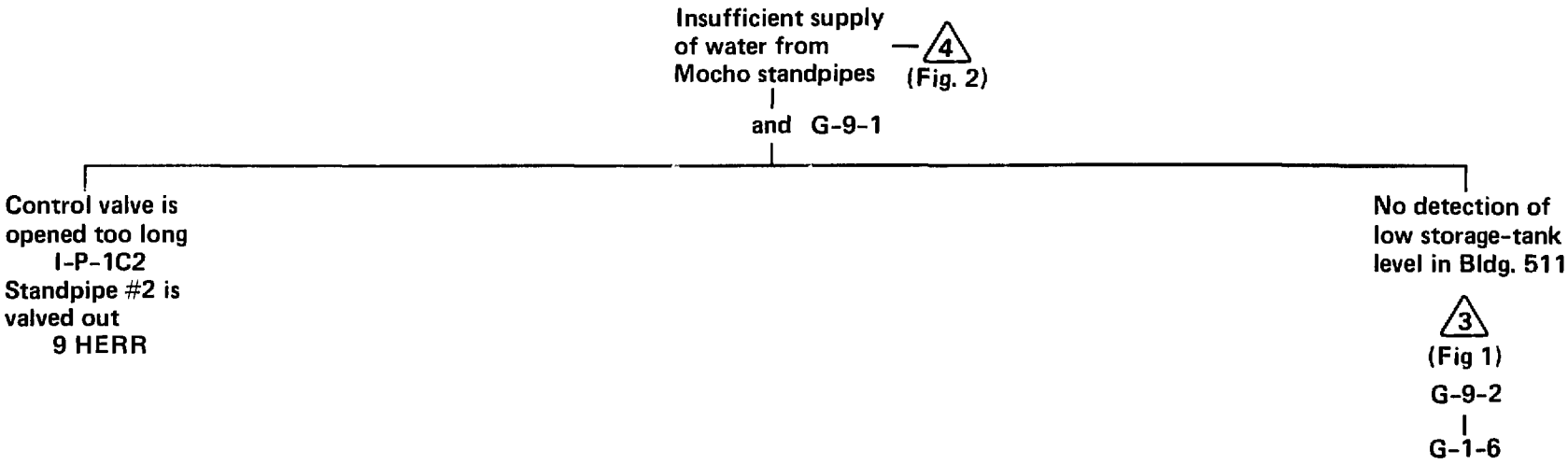

U. S. Government Printing Office: 1985/2-587-002/24054